

NEXT GENERATION OF CURRENT SENSOR FOR AERONAUTICS:  
PRELIMINARY DESIGNS

A Thesis  
Presented to  
The Academic Faculty

By

Cyril Babinet

In Partial Fulfillment  
Of the Requirements for the Degree  
Master of Science in  
Mechanical Engineering

Georgia Institute of Technology

August 2008

NEXT GENERATION OF CURRENT SENSOR FOR AERONAUTICS:  
PRELIMINARY DESIGNS

Approved by:

Dr. Jianmin Qu, Co-Advisor  
George W. Woodruff School of  
Mechanical Engineering  
*Georgia Institute of Technology*

Dr. Mohammed Cherkaoui, Co-Advisor  
George W. Woodruff School of  
Mechanical Engineering  
*Georgia Institute of Technology*

Dr. Christophe Giraud-Audine  
*Ecole Nationale Supérieure d'Arts et  
Métiers*

Dr. Nico F. Declercq  
George W. Woodruff School of  
Mechanical Engineering  
*Georgia Institute of Technology*

Date Approved: Tuesday, 16 May 2008

## ACKNOWLEDGMENTS

My motivation to pursue the thesis option of the Master's program was to get more from my Georgia Tech experience. I must acknowledge the help of my co-advisor Dr. Mohammed Cherkaoui, who provided me with this exciting and challenging project. The interaction with M. Idriss Ilali and M. Marc Bournat from Leach International gave me an insight on industrially motivated research. They have been very friendly.

I must acknowledge also the great help I received from Dr. Christophe Giraud-Audine, who was my advisor at *Ecole Nationale Supérieure d'Arts et Métiers* for the first part of the project when I was in Metz. He has been helping me conduct my research, organise my ideas, and spent a lot of time working with me. I also need to thank my co-advisor Dr. Jianmin Qu for his help. He gave me some of his precious time.

Dr. Declercq also helped me organising my ideas by letting me explain him the difficulties I was encountering. Of course, I also need to acknowledge the help of David Swafford whom I have worked with from the beginning. We would most often tell each others our latest developments and difficulties, exchanging ideas to solve problems and sharing excitement for their prospective solutions.

## TABLE OF CONTENTS

LIST OF TABLES .....	vii
LIST OF FIGURES .....	viii
SUMMARY .....	xiii
CHAPTER 1: INTRODUCTION .....	1
1.1- Presentation of the partner company .....	1
1.2- Describing Leach's need .....	2
1.2.1- Strategic need .....	2
1.2.2- Technological need.....	3
1.3- Specifications.....	3
1.4- State of the Art.....	4
1.4.1- Primary techniques <sup>1</sup> .....	5
1.4.2- Hall Effect sensor .....	6
1.4.3- About the Piezoelectric Transformers (PT).....	7
1.4.4- Rogowski transformers <sup>4</sup> .....	8
1.4.5- Magnetostrictive-piezoelectric magnetic sensor <sup>5</sup> .....	11
CHAPTER 2: THE OSCILLATING COIL (OC) .....	12
2.1- Faraday's law and principle.....	12
2.2- Sensitivity calculation, theoretical study .....	15
2.3- Simulation of the magnetic field B.....	20
2.4- Resuming the calculation with B simulated .....	27
2.5- Output signal.....	30

CHAPTER 3: THE VARIABLE SECTION COIL (VSC).....	33
3.1- Principle.....	33
3.2- Sensitivity calculation, theoretical study .....	37
3.3- Resuming the calculation with simulated B .....	42
CHAPTER 4: THE ROTATING COIL PLUS STATIC COIL (RC+SC) .....	46
4.1- Principle.....	46
4.1.1- The Rotating Coil as a first approach .....	46
4.1.2- Adding a Static Coil .....	47
4.2- Sensitivity calculation, theoretical study .....	49
4.2.1- Magnetic flux in the rotor and subsequent voltage and current.....	49
4.2.2- Magnetic flux in the stator and sensitivity.....	50
4.3- New simulation for a three dimensional magnetic problem.....	53
4.3.1- Limits of the software and decomposing the analysis .....	53
4.3.2- Magnetic flux in the rotor and subsequent voltage and current.....	54
4.3.3- Magnetic field of the rotor.....	56
4.3.4- Magnetic flux in the stator and sensitivity.....	57
4.4- Output signal.....	59
4.5- Mechanical considerations .....	61
4.6- Further developments .....	61
CHAPTER 5: CONCLUSION .....	64
APPENDIX A.....	66
APPENDIX B .....	69
APPENDIX C .....	75
APPENDIX D.....	80

APPENDIX E .....	82
APPENDIX F.....	85
APPENDIX G.....	87
APPENDIX H.....	89
APPENDIX I .....	91
APPENDIX J .....	99
APPENDIX K.....	101

## LIST OF TABLES

Table 1: Design parameters and dimensioning of the OC .....	18
Table 2: Dimensioning of the OC for two different ratios of length to width .....	19
Table 3: Design parameters of the OC considering the simulated magnetic field.....	29
Table 4: Dimensioning of the OC considering the simulated magnetic field.....	29
Table 5: Adjusted design parameters of the OC .....	29
Table 6: Adjusted dimensioning of the OC .....	29
Table 7: Set of parameters for the VSC .....	38
Table 8: Another set of parameters for VSC .....	39
Table 9: Set of paramaters for VSC.....	43
Table 10: Set of parameters for RF+SC based on a full range for I .....	52
Table 11: Average flux density on the rotor in function of the angle.....	54
Table 12: Electromagnetic characteristics of the RC+SC after the simulation for $\varphi_r$ .....	55
Table 13: Data collection for the flux in the stator .....	89

## LIST OF FIGURES

Figure 1: The Hall Effect on a conducting plate <sup>1</sup> .....	6
Figure 2: The Hall Effect based current sensor <sup>1</sup> .....	7
Figure 3: Orders of magnitude associated with piezoelectric transformers.....	8
Figure 4: Principle and basic configuration of a Rogowski Transformer <sup>4</sup> .....	9
Figure 5: Specific configuration for Rogowski transformers <sup>4</sup> .....	10
Figure 6: Configuration of the magnetostrictive-piezoelectric magnetic sensor .....	11
Figure 7: Oscillating coil on a cantilever beam .....	13
Figure 8: Oscillating coil on a pivot-pivot beam .....	14
Figure 9: Oscillating coil on a free-free beam .....	15
Figure 10: Infinite wire hypothesis (left) and flux in a rectangular coil (right).....	16
Figure 11: Dimensions of the OC device.....	19
Figure 12: The sensor in its environment. The coils (in red) receive a magnetic flux that varies in time as they move in a non-constant field.....	20
Figure 13: Field lines surrounding the bus bar .....	21
Figure 14: Density of flux surrounding the bus bar .....	21
Figure 15: The magnetic flux near the conductor .....	22
Figure 16 : Magnetic field B simulated, linearization and gradient.....	24
Figure 17: B from simulation in comparison to expected values from analytical model ..	24
Figure 18: Gradient B from simulation in comparison to expected values from analytical model.....	25
Figure 19 : Profile of B and its gradient .....	25
Figure 20: Profile of B and its gradient .....	26



Figure 21: Flux of B and its time-derivative obtained for the simulated and linearised field	
B .....	28
Figure 22: Frequency content of the output signal .....	30
Figure 23: Frequency content of the output signal .....	31
Figure 24: Diamond-shaped VSC.....	34
Figure 25: Hexagonal shape VSC.....	35
Figure 26: The sensor in its environment. The coil receives a magnetic flux that varies in time as it deforms.....	36
Figure 27: Example of dimensions for hexagonal shape VSC based on B for an infinite wire .....	37
Figure 28: Two types of articulations for VSC.....	37
Figure 29: Derivative of the flux separately in the rectangle and the diamond, then on the whole coil.....	38
Figure 30: Maximum in time of the derivative, in function of the angle at rest.....	39
Figure 31: Derivative of the flux separately in the rectangle and the diamond, then on the whole coil.....	40
Figure 32: Maximum in time of the derivative, in function of the angle at rest.....	40
Figure 33: A hexagonal coil actuated by a stack .....	41
Figure 34: Reproducing the coil by translation.....	42
Figure 35: Magnetic flux in the coil and its time derivative.....	43
Figure 36: Dynamics and kinematics in the coil.....	44
Figure 37: Above the bus bar: rotor carrying a coil and facing a field line.....	47
Figure 38: Above the bus bar: rotor and stator with a quarter of a turn.....	48
Figure 39: Data and modelling for the average flux density on the rotor.....	55

Figure 40: Normal component of the magnetic field in the rotor's coil and in the immediate surroundings, for $\beta = 90^\circ$ .....	56
Figure 41: Simulated flux in the stator in function of the angular position of the stator .....	57
Figure 42: Overall output sensitivity of the RC+SC sensor .....	59
Figure 43: Output signal and filtered output signal .....	60
Figure 44: Output signal, rectified and integrated over $4\pi$ .....	60
Figure 45: The rotor based on last optimisation becomes just one massive coil .....	63
Figure 46: Effect of the simplification of the denominator on the actual output signal ....	78
Figure 47: Frequency content of the output signal .....	79
Figure 48: Signal and reconstruction through inverse Fourier for checking, in V/A .....	95
Figure 49: Amplitude in V/A and phase of the Fourier transform .....	95
Figure 50: Real part and imaginary part of the signal in V/A. The real part (cosines) is negligible.....	96
Figure 51: Power spectrum of the signal. The harmonics are not negligible.....	96
Figure 52: The reconstruction using only the imaginary part (sines) is fairly accurate.....	97
Figure 53: Top view of the rotor and polar coordinates .....	99
Figure 54: Centripetal acceleration (top) and subsequent distributed force on the rotor (bottom).....	100
Figure 55: Zoom on the set of coils of the rotor near the upper edge.....	102

LIST OF SYMBOLS

Context		Variable	Associated physical magnitude
Electromagnetic		$I$	Current to be measured
		$B$	Magnetic field generated by $I$
		$\mu_0$	Permeability of vacuum
Bus bar (section)	Dimensions	$l_b$	Width
		$e_b$	Thickness
	Axis	$x$	Direction of width
		$y$	Direction of thickness
All designs	Coil	$u_0$	Initial position of the coil
		$d$	Half-height of the coil
		$e(t)$	Electromotive force on the coil
		$u(t)$	Position of the coil
		$\varphi(t)$	Magnetic flux in the coil
		$N$	Number of coils
Oscillating Coil design	Beam	$E$	Young's modulus of the beam
		$\rho$	Density
		$d$	Half-height of the beam
		$I_{yy}$	Second momentum of area
		$\sigma$	Stress in the beam
		$L$	Length of the reasoning part of the beam
		$l$	Width of the beam
		$\alpha$	Length over half thickness ratio
		$\omega$	Natural frequency of the beam (rad.s <sup>-1</sup> )
		$k$	Vibration mode
		$a$	Amplitude of vibration of the beam
Variable Section Coil design	Diamond-shaped coil	$h$	Side of the diamond
		$a$	Amplitude of vertical displacement
		$b$	Amplitude of horizontal displacement
		$d_0$	Half vertical diagonal, original value
		$e_0$	Half horizontal diagonal, original value
		$\theta_0$	Angle between horizontal diagonal and a side, original value
	Hexagonal shaped coil	$l_0$	Length of the upper bar
	Actuator	$\omega$	Deformation cycle frequency
		$td\%$	Deformation rate of the actuator

Context		Variable	Associated physical magnitude
Rotating Coil plus Fixed Coil design	Rotor	$e_r$	Electromotive force on the rotor
		$i_r$	Current on the rotor
		$\varphi_r$	Magnetic flux on the rotor
		$B_r$	Magnetic field due to current on rotor
		$n_r$	Number of coils on the rotor
		$R_r$	Resistance of the rotor's coils
		$A_r$	Cross-sectional area of the conductor
		$\omega$	Frequency of rotation ( $\text{rad.s}^{-1}$ )
	$\beta$	Angular position	
	Rotor, Stator	$J$	Density of current
		$S$	Surface of a coils (loop)
	Stator	$e_s$	Electromotive force on the stator
		$i_s$	Current on the stator
		$\varphi_s$	Magnetic flux on the stator
		$n_r$	Number of coils on the rotor
$R_s$		Resistance of the stator's coils	
Sensor		$s$	Sensitivity
		$s_0$	Desired sensitivity
		$t$	Time variable

## SUMMARY

As a specialist in power distribution for the aerospace industry, Leach International-Europe intends to master both design and production of the current sensor – a strategic component – while offering a novel technology, free from important disadvantages of the previous generation. This report puts forward some research directions to replace the present generation, based on the Hall Effect and equipping most of commercial and military aircrafts. Relying on a feasibility study, and after reviewing the state of the art, this work heads quickly on exploiting Faraday's Law. The latter allows getting a voltage as an output directly from the magnetic field generated by the current flowing inside the conductor. The different solutions introduced here are based on analytical calculations (when it is possible), simulations and numerical calculations and are grounded on designing a sensor with an acceptable sensitivity.

## CHAPTER 1: INTRODUCTION

### **1.1- Presentation of the partner company**

From a modest beginning as a one-product company in 1919, Leach International Corporation has claimed a position of world leadership in the design and manufacture of power distribution systems for the aerospace and rail industries.

Designed for applications as diverse as civil and military aviation, satellites and railway systems, Leach International's line of products includes hermetically sealed relays and complementary devices to provide time delay and power measurement functions. Comprehensive lines of push-button indicators, solid state power controllers and limit switches also play important roles in the company's product mix.

From the first relay, the product family grew to include other types of relays including time delay relays, aircraft switches, power monitor, power distribution, and aircraft relays for the communications and electrical industries. It was not long before Leach relays became known to aircraft manufacturers and products were developed specifically for aircraft power switching as well as for aircraft communications.

By 1992, Leach consolidated all of its U.S. manufacturing operations at the present site in Buena Park, California. European operations were consolidated in Sarralbe, France, Leach International's European headquarters. In 1997, Leach once again extended its global reach with the addition of Leach International Asia-Pacific, Ltd. In July 2004, Esterline Corporation, a specialized manufacturing company serving the needs of the aerospace and defence industry, acquired Leach International. Leach has 1000 employees and representatives in more than 20 countries.

## 1.2- Describing Leach's need

Leach now intends to develop the next generation of current sensors. This is the Next Generation of Current sensor (NGCS) project. To that purpose, the company asked David Swafford, from the Georgia Institute of Technology, to perform a feasibility study<sup>1</sup> during the summer 2006. This study constitutes a very broad state of the art, and presents a rich variety of directions to be explored. While Mr. Swafford continues the NGCS project in the frame of his PhD thesis, this Master's Thesis intends to initiate other solutions in a cooperative parallel work so as to provide Leach with a broader spectrum of solutions. This section summarizes the motivations of Leach.

### 1.2.1- Strategic need

Today Leach relies on suppliers for certain important components of the current sensors it integrates in its measurement circuits. The company wishes to have a better control of this situation by developing a product that would be its own. The main strategic motivation is that the current situation of being dependent *vis-à-vis* the supplier compels Leach to constitute considerable stocks of the subcontracted components to ensure everlastingness of the fleet it equips. Indeed, it does not master the strategic decisions of the subcontractor, who can decide to stop producing the component.

Furthermore, if a new generation of sensors happens to appear on the market and supersede the current one, being technologically a step ahead the competitors may become a major asset. If Leach's developed solution overcomes, it can be included into

numerous products as integrated solutions. The entire range of these products thus takes advantage of the exclusive technology.

### 1.2.2- Technological need

Having established the motivation to develop peculiar technology, it is now necessary to come up with a genuine innovation. Nowadays sensors are based on the Hall Effect; this technology is explained in detail at section 1.4.2. Despite its being perfectly well-proven today, this technology presents notable disadvantages, mostly due to the presence of a magnetic circuit in the system. The latter is first of all heavy and voluminous, both elements being highly significant in the aeronautical context. But this very context also implies a severe thermal and electromagnetic environment. The magnetic circuits present notable sensitivity to the temperature, as well as problems of remnant polarisation, magnetic saturation, and offset adjustment.

Moreover, the primordial necessity to offer Leach clients a wide range of working temperatures involves that current products suffer important tradeoffs on other parameters.

### **1.3- Specifications**

The definition of the sensor is deliberately as light as possible, so as to avoid limiting the imagination of the designers and the variety of the leads examined in the early phase of the project and thus favour a really novel design. The specifications defining the future sensor are reduced to the characteristics of the current to be measured and those of the



conductor. The conductor, called a bus bar, is a bar of copper or aluminium. It is a part of the Power Distribution Unit (PDU) in a commercial or military aircraft.

- Section of the conductor: 3 x 20 mm, typically
- Range of current: +/- 1000 Amperes
- DC current, 28 V
- The voltage drop due to measure will be naught or very little
- Range of temperature: -55°C ~ +75°C
- Galvanic insulation
- If possible, the sensor will be able to measure AC current as well. The latter having a range of 300 Hz to 1000 Hz

The technical objectives are to:

- Decrease weight and size
- Decrease manufacturing costs
- Reduce sensitivity to temperature, vibrations and electromagnetic interference
- Design for mass production
- Adapt to the scale of Micro Electro Mechanical Systems (MEMS). This adaptation would constitute the object of a future study.

#### **1.4- State of the Art**

This section offers a quick overview of the different current sensing principles in use, from the most basic ones to the Hall Effect. This part relies on the preceding feasibility

study<sup>1</sup> and goes over its main points. The goal here is not to repeat the feasibility study, but to recall basic facts to the reader. The section also contains a description of the first techniques that have been considered in this study.

#### 1.4.1- Primary techniques1-

The most basic way to measure current is to insert a resistor, called a shunt, in series in the circuit. This resistor will have a voltage across its terminals and is related to the current, according to Ohm's Law. This technique has the advantage of being extremely simple and suitable for both alternating and direct current. It has the weaknesses of being invasive, offering no galvanic insulation, and obviously causes a voltage loss. The two last limitations are very important in the context of high current and low voltage.

Another common way of measuring currents is to use transformers. It is quite simple, offers a galvanic insulation and is extensively used in many applications. However, this principle allows only alternating current to be measured, and requires a magnetic circuit. Some developments like null-flux transformers allow for reducing the size of the magnetic circuit, but for measuring high currents they would consume too much power.

The last category gathers the other techniques under the label "transducers". The transducers convert one form of energy into another. For example, according Faraday's Law, a coil placed into a magnetic field transforms a magnetic flux into an electromotive force. Transducers are a very broad category and they have various interests and limitations. However, most of them are both AC and DC compatible and offer a galvanic insulation.

#### 1.4.2- Hall Effect sensor

The Hall Effect was discovered in 1879 by Dr. Edwin Hall. When a current-carrying thin plate is exposed to a magnetic field it produces a voltage, known as the Hall voltage. As a matter of fact, the charge carriers in the plate experience the Lorentz force that alters their course. The figure presented below shows how the deviation of the electrons from their original path ends up creating a voltage across the plate, in the direction orthogonal to the current.

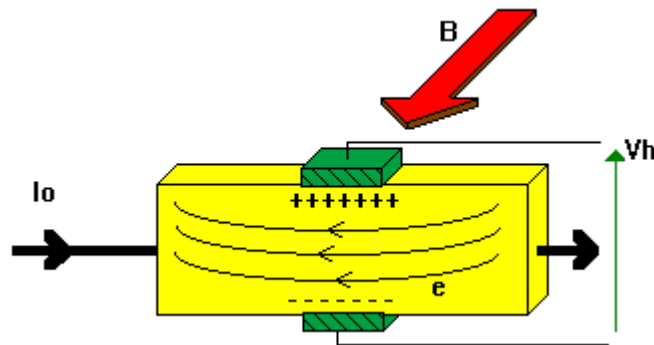


**Figure 1: The Hall Effect on a conducting plate1-**

An open magnetic circuit is used to concentrate the magnetic flux so as to get sufficient field intensity in order to create a readable voltage. Furthermore this makes the sensor almost insensitive to the position of the conductor inside the magnetic circuit. In the air gap is placed the Hall Effect sensor, thus experiencing a dense magnetic field. In the particular context of the application developed here, high currents will make it necessary to have a magnetic circuit able to concentrate high magnetic flux without reaching saturation. This means that the circuit must be relatively voluminous, and thus heavy,

even with high magnetic permeability materials, since the performance of the magnetic material will suffer a tradeoff with its resistance to temperature, a very demanding constraint. As a matter of fact, knowing the high magnetic flux carried and the frequent dramatic drop of convection of the air in the aircraft, the management of the temperature is a critical issue.

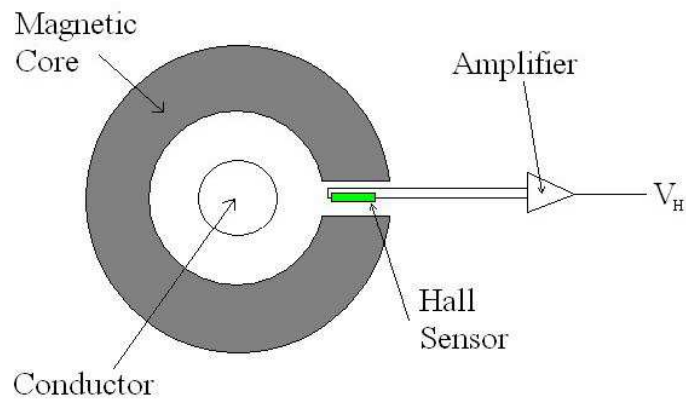


**Figure 2: The Hall Effect based current sensor1-**

#### 1.4.3- About the Piezoelectric Transformers (PT)

Because they are adaptable to very small scale and they offer galvanic insulation, piezoelectric transformers have been considered attractive from the first stage of this study, and were the first path explored. The main source of information was an article of *Techniques de l'Ingénieur*<sup>3</sup>. It appeared that this solution was not adapted to direct currents, first because the gain of such transformers is mainly interesting at the resonance of the device. The following graph explains the difficulty of using such a device for DC. The capacitance symbol stands for the electrical image of the piezoelectric material.

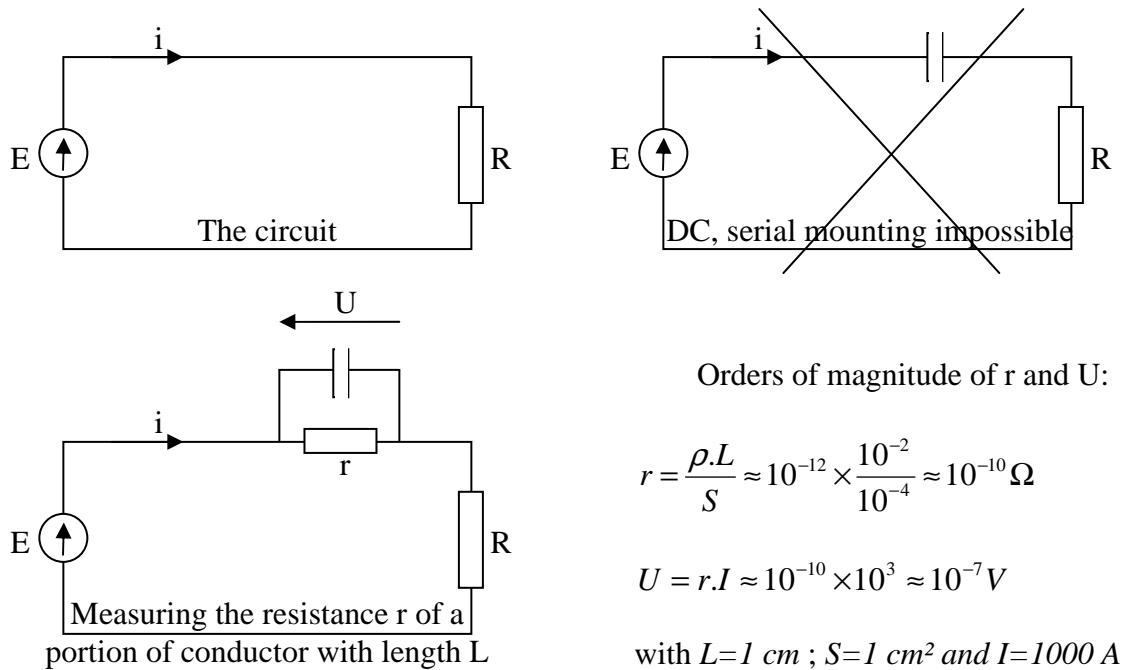


**Figure 3: Orders of magnitude associated with piezoelectric transformers**

In this configuration the transformer will not offer a sufficient gain to provide a reasonable output. Therefore the piezoelectric transformer does not meet the requirements.

#### 1.4.4- Rogowski transformers<sup>4</sup>

This type of transformer offers by its nature galvanic insulation and sustains a wide range of currents, due to the absence of a magnetic circuit, and thus saturation phenomenon. This absence also allows for good linearity. Rogowski transformers are known to offer correct precision and a large bandwidth. The latter will be reduced if an extensive winding is used so as to improve the sensitivity.

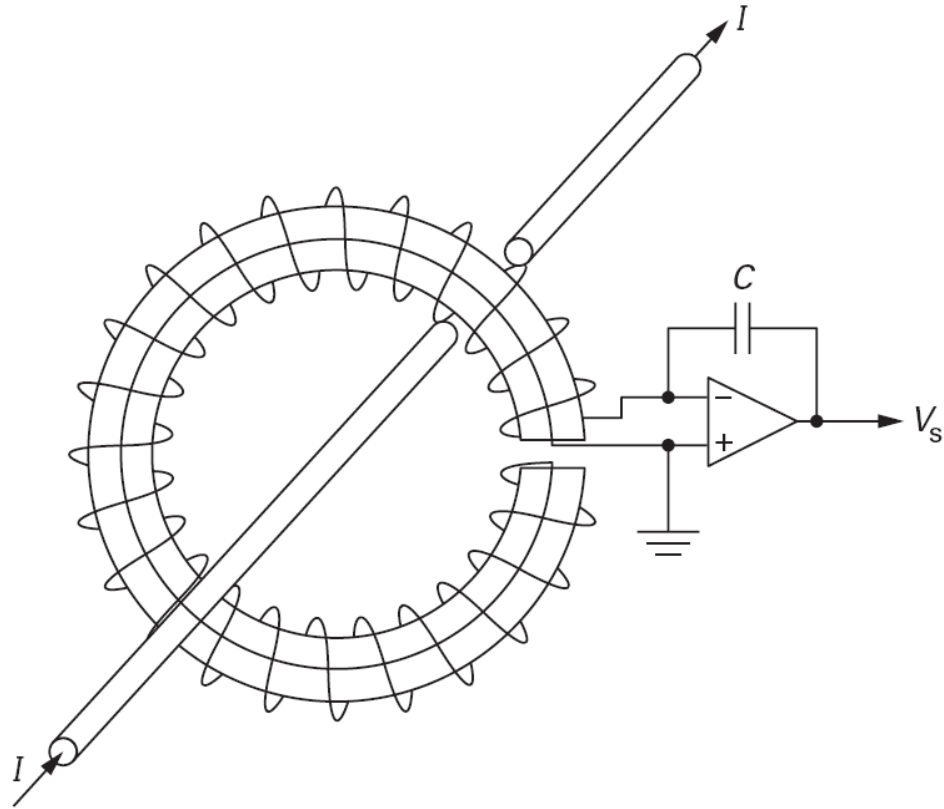


**Figure 4: Principle and basic configuration of a Rogowski Transformer4-**

Another main interest of this type of transformer, presented in **Figure 4**, is that while the winding captures the orthoradial field, the coaxial return cancels the flow in the overall loop to be immunized to this type of parasite flux.

Moreover, **Figure 5** introduces a configuration where two series of printed circuit boards carrying the winding are placed concentrically. The output integrator is working on the difference of the voltages. An external field would generate very similar voltages on both half-windings, thus cancelling each other with the subtraction whereas those voltages due to the current to measure would not.

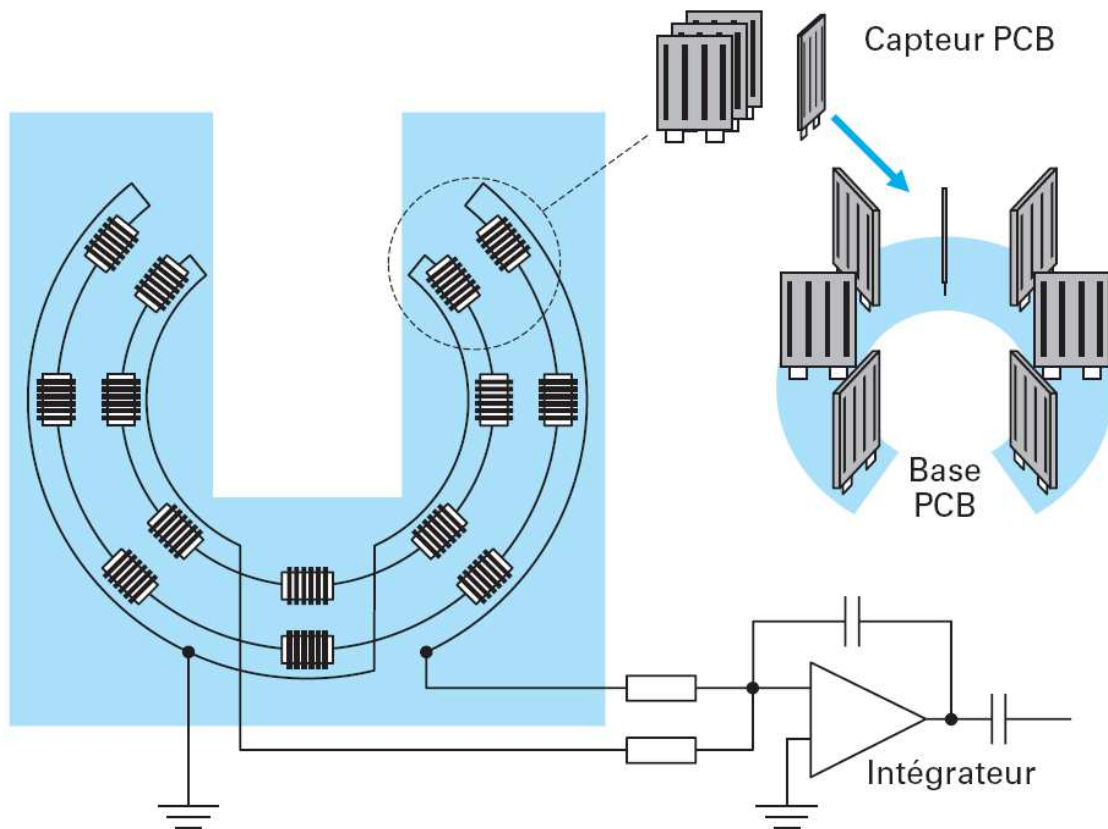


**Figure 5: Specific configuration for Rogowski transformers4-**

One disadvantage of this device is that it needs to encircle the conductor, which will always be a limit to miniaturisation. In addition it is based on Faraday's Law, which means that the output is proportional to the time-variation of flux. It is then unable to measure DC. The solutions developed in this thesis and presented in following chapters will nonetheless introduce different ways to use Faraday's Law for measuring DC. In the present case, this would require integrating the variation of flux over the whole time, which would not make sense.

#### 1.4.5- Magnetostrictive-piezoelectric magnetic sensor<sup>5-</sup>

Other principles have been considered that have turned out to be difficult to adapt to DC.

The magnetostrictive-piezoelectric magnetic sensor<sup>5-</sup> should be cited.

The device consists of a layer of magnetostrictive material, a layer of piezoelectric material and an interface in between. The first deforms under the action of the magnetic field surrounding the current to measure. The interface transmits the deformation, while the second layer changes this deformation directly into an output voltage. However, because of different hysteretic behaviour, it turns out to be impossible, at this stage, to set up a solid interface. Thus the interface is a viscous fluid, which can transmit vibrations very well, but not permanent deformations. In addition resonance is used to obtain good sensitivity. Consequently, this device can only be used for AC in its present state.

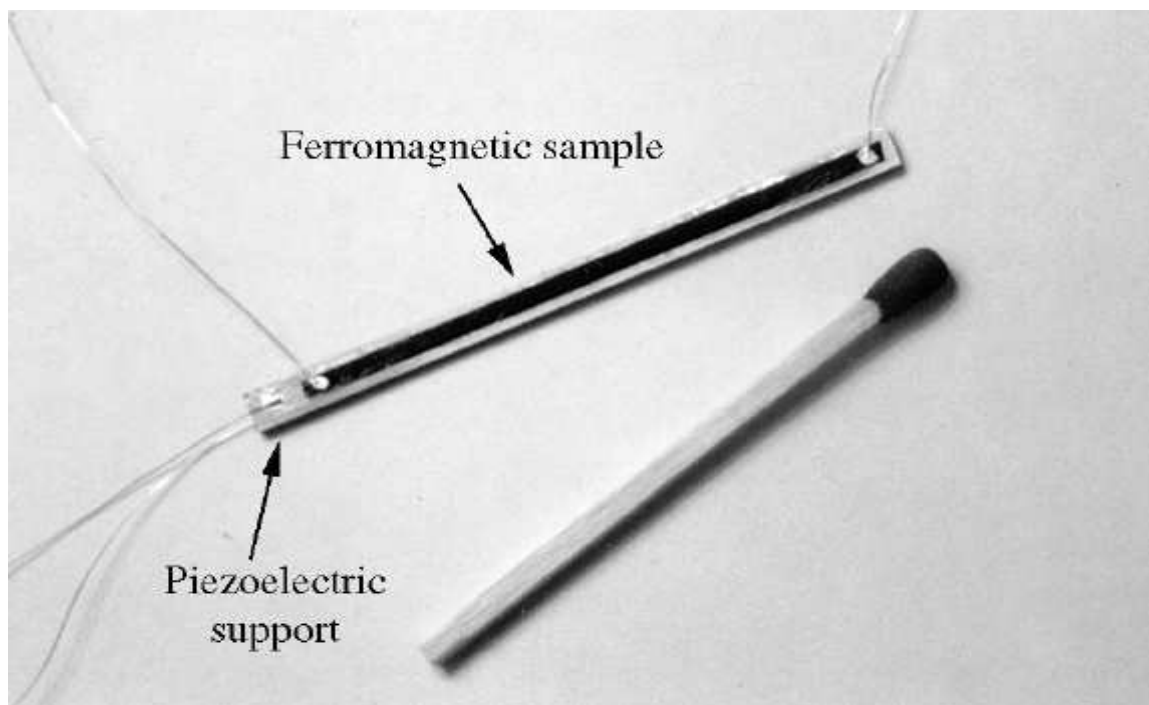


**Figure 6: Configuration of the magnetostrictive-piezoelectric magnetic sensor**



## CHAPTER 2: THE OSCILLATING COIL (OC)

### 2.1- Faraday's law and principle

The heart of this study is about utilising Faraday's Law for a coil. Its expression is reminded here:

$$e = -\frac{d\phi}{dt} \quad \text{Equation 1}$$

where  $e$  is the electromotive force due to the variation of magnetic flux  $\phi$  at the terminals of the coil. This appears to be extremely attractive for several reasons. First of all, it has a voltage as a direct output of the sensor. Secondly, as with the Hall Effect, this principle is based on the magnetic field surrounding the conductor, which allows measurement without contact or voltage loss. The architectures developed here around this law do not have a magnetic circuit, thus eliminating the disadvantages specific to this component. Furthermore, unlike the Hall Effect sensor, the concepts presented here should not be significantly sensitive to the temperature.

For DC currents in the bus bar, the magnetic field is static, and Faraday's Law is based on time-variation of the flux. Despite this fact, all the concepts developed in the following chapters make it possible to have a time variation of the flux in the coil, each of them by different means. In short, the magnetic field is static, but the coil itself does not have to be so.

The simplest idea consists of moving the coil in the magnetic field (which is not constant in the space). Thus, in the course of its displacement, the coil “feels” a time-variation of the magnetic flux. Rewriting equation 1, one gets:

$$\frac{\partial \varphi}{\partial t} = \frac{\partial \varphi}{\partial u} \times \frac{\partial u}{\partial t} \quad \text{Equation 2}$$

where  $u$  is the position of the coil. The first term shows that it is necessary to have a magnetic field gradient, so that the flux in the coil would depend on its position. The second term corresponds to the velocity of displacement of the coil.

The displacement will be obtained using one or several piezoelectric crystals. A beam will act as a mechanical amplifier. This allows for a very simple architecture. The beam will be in resonance, thus the consumption of energy is reduced to compensating for the different types of losses.

Three configurations were studied.

The first one is a cantilever-type beam:

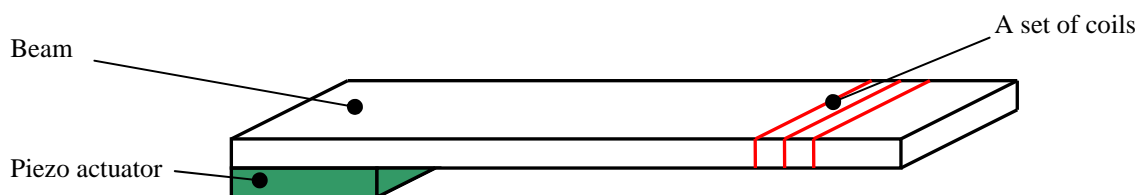


**Figure 7: Oscillating coil on a cantilever beam**

This is the simplest design, and the easiest to produce. It allows large deflections of the beam. But it will generate high stress at the link between the actuator and the beam. In addition the coils, if there are several, cannot be all placed at the antinode. This should be taken into account when computing the displacement, as much as a slight rotation of section, which will affect the flux by the cosine of the angle of rotation.

Then one has a pivot – pivot configuration:

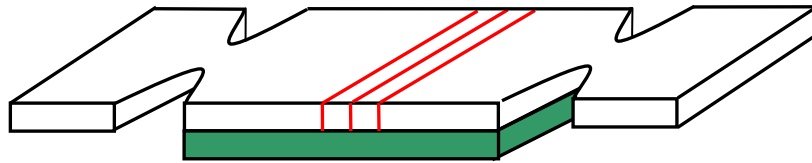


**Figure 8: Oscillating coil on a pivot-pivot beam**

The cuts in the beam are made to create pivot-like links with the fixed extremities. Here the winding may be centred on the antinode, the latter having no rotation of section. In addition, the piezoelectric crystal is used in its 31-mode, which is the most efficient. However, this configuration may be more difficult to mount, because of the critical gluing. Moreover attaching the piezoelectric ceramic may interfere with the winding. The latter should be set up initially, unless it is coiled around both beam and ceramic. One could also imagine a “bender”-type ceramic, being the beam itself. This would be a simplified version of this configuration, but not necessarily easy to set up. A bending piezo-actuator is a bi-layer or multi-layer actuator. Basically, bending is due to a difference of elongation of the layers. Several configurations may achieve this result. They are explained in **Appendix A**.

The third configuration can be considered a free-free or a pivot- pivot configuration:

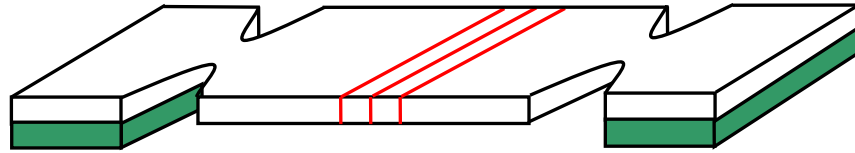


**Figure 9: Oscillating coil on a free-free beam**

Here the actuators vibrate in their 33-mode, but one can control the vibration easily. Adding an accelerometer to the device could allow compensation for external vibrations or perturbations due to strong acceleration by sending to the actuator the image of the perturbation with a phase shift of  $180^\circ$ .

A chosen mode, probably the first one, will carry the important information in the output signal, the rest being filtered off. Nonetheless, controlling parasitic vibration remains interesting to preserve the device and protect the working mode from external excitations.

## **2.2- Sensitivity calculation, theoretical study**

The first crucial aspect of the design of a sensor based on a novel concept is to check its ability to sense anything, and to give a usable output. First of all, an analytical study is performed. Fundamentally, the analytical study requires hypothesising the shape of the magnetic field  $\mathbf{B}$ . The hypothesis is that the field decreases as  $1/r$ , like the field generated by an infinite wire carrying a current. In reality the bus bar has a rectangular section, so a simulation, presented in section 2.3, is necessary to have a better idea of the shape and the values of the field.

The reasoning presented below is detailed in **Appendix B**:

- Calculation of magnetic field **B** due to the current  $I$  in the bus bar

$$B(r) = \frac{\mu_0 \cdot I}{2\pi \cdot r} \quad \text{Equation 3}$$

- Calculation of the flux of **B** in the coil

$$\varphi = \frac{\mu_0 \cdot l}{2\pi} \cdot I \cdot \left( \ln \frac{u(t) + d}{u(t) - d} \right) \quad \text{Equation 4}$$

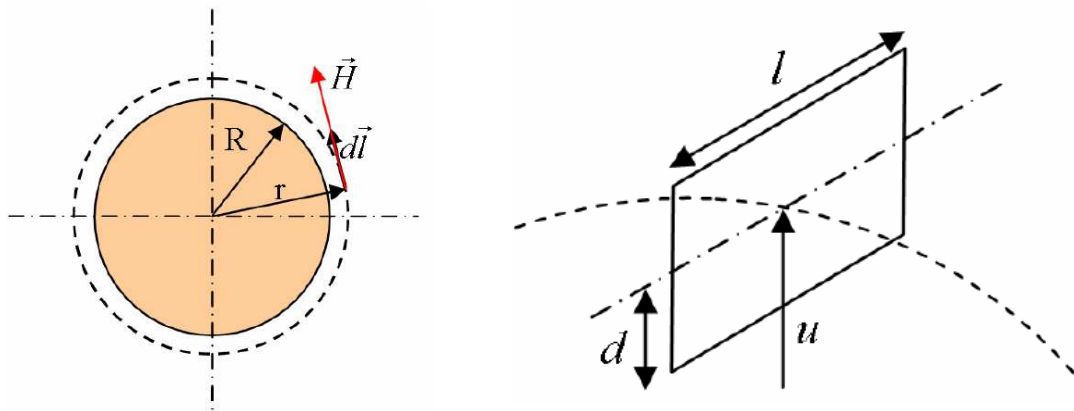


Figure 10: Infinite wire hypothesis (left) and flux in a rectangular coil (right)

- Calculation of the sensitivity

$$s = -\frac{\mu_0 \cdot l}{2\pi} \cdot \frac{2a \cdot d \cdot \omega \cdot \cos \omega t}{u_0^2} \quad \text{Equation 5}$$

Where  $a$  is the amplitude of the oscillation,  $d$  is the half-thickness,  $l$  the width, and  $u_0$  the position at rest. For further calculations, the cosine is omitted, only the amplitude is kept.

This gives:

$$s = -\frac{\mu_0 \cdot l}{2\pi} \cdot \frac{2a \cdot d \cdot \omega}{u_0^2} \quad \text{Equation 6}$$

- Calculation of the frequency of resonance of the carrying beam for the  $k^{\text{th}}$  mode

$$\omega_k = \sqrt{\frac{E \cdot I_{yy}}{\rho \cdot S}} \left( \frac{k \cdot \pi}{L} \right)^2 \quad \text{Equation 7}$$

With  $L$  the length of the beam,  $E$  is Young's modulus,  $\rho$  the density, and  $I_{yy}$  the second moment of area. Replacing  $\omega_k$  into the expression of  $s$  gives a more specific expression:

$$s = -2\mu_0 \cdot \pi \sqrt{\frac{E}{12\rho}} k^2 \frac{d^2 \cdot l}{u_0^2 \cdot L^2} a \quad \text{Equation 8}$$

- Calculation of the maximum amplitude of displacement  $a_{max}$  based on a maximum acceptable stress  $\sigma_{crit}$  :

$$a_{max} = \frac{\sigma_{crit} \cdot L^2}{E \cdot d \cdot k^2 \pi^2} \quad \text{Equation 9}$$

Replacing  $a$  into  $s$ , stating  $l = \alpha \cdot d$ , and taking into account the number of coils  $N$ , the maximal value of sensitivity based on the maximal stress in the beam becomes:

$$\max_{\sigma}(s) = -\alpha \cdot \frac{\mu_0}{\pi} \sqrt{\frac{1}{3\rho \cdot E}} \frac{d^2}{u_0^2} \sigma_{crit} \cdot N \quad \text{Equation 10}$$

Now the intent was to dimension the device, so as to have a reasonable sensitivity. Then

**Equation 10** is flipped into:

$$d = u_0 \sqrt{\frac{s_0 \cdot \pi \sqrt{3 \rho \cdot E}}{\alpha \cdot \mu_0 \cdot \sigma_{crit} \cdot N}}$$

**Equation 11**

where the desired sensitivity  $s_o$  is introduced.

For practical reasons, the output of the sensor after amplification should be aligned on this of a usual Operational Amplifier (OA), that-is-to-say +/- 5V as a full range. Here the full range should correspond to +/-1000A, so we expect the sensitivity after amplification ( $s_A$ ) to be  $5 \cdot 10^{-3}$  V/A.

Basic OA may have a gain of 100, thus  $s_o$  needs to be  $5 \cdot 10^{-5}$  V/A.

**Table 1: Design parameters and dimensioning of the OC**

Parameters (SI)	$E$ (Mpa)	$\rho$ (kg.m <sup>-3</sup> )	$s_o$ (V.A <sup>-1</sup> )	$\alpha$	$\sigma_{crit}$ (MPa)	$u_0$ (m)	$N$
	2.00E+11	2.40E+03	5.00E-05	4	4.00E+08	3.00E-03	100
<b>d(m)</b>	<b>5.17E-04</b>						

In red are the design parameters, in black the calculated values. The last parameter to fix is the ratio between length and width. To respect fully the “beam hypothesis”, this ratio should be at least ten. Nonetheless, two configurations are presented in the next table, with a ratio 5 and 10 respectively.

**Table 2: Dimensioning of the OC for two different ratios of length to width**

$2d$	$l$	$L/l$	$L$	$a$	$u_0$ (m)	$\omega$
1.03E-03	2.06E-03	5	1.03E-02	4.19E-05	3.00E-03	2.52E+05
1.03E-03	2.06E-03	10	2.07E-02	1.67E-04	3.00E-03	6.29E+04

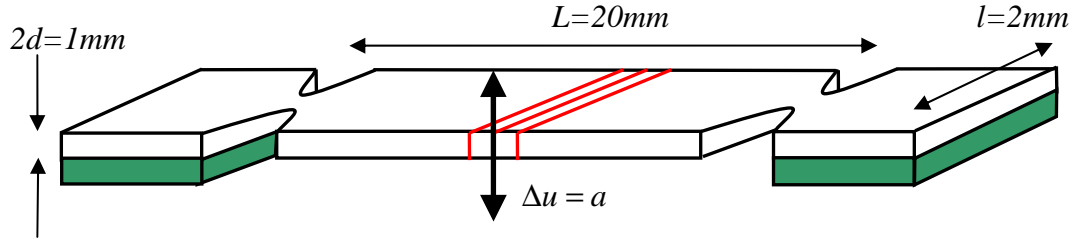


**Figure 11: Dimensions of the OC device**

Under the threshold of 10, a Finite Element Analysis should be performed to check the natural frequencies of the beam. Moreover, some transverse modes may appear, even though their influence should be minimal.

The calculations presented here are directly valid for the model corresponding to **Figure 9** or **Figure 11**. For this of **Figure 8**, the same calculation could be performed with a homogenised section.

According to this analytical study, such a device appears to be feasible. Even if not adaptable to the scale of MEMS, a  $2 \times 2 \times 25\text{mm}$  device is still very light (less than 1g) and occupies a small volume ( $100\text{mm}^3$ ).

Still relying on the theoretical **B**, a Matlab calculation is done to check the influence of the hypothesis made in the analytical study. The code and the detailed results are shown in **Appendix C**.



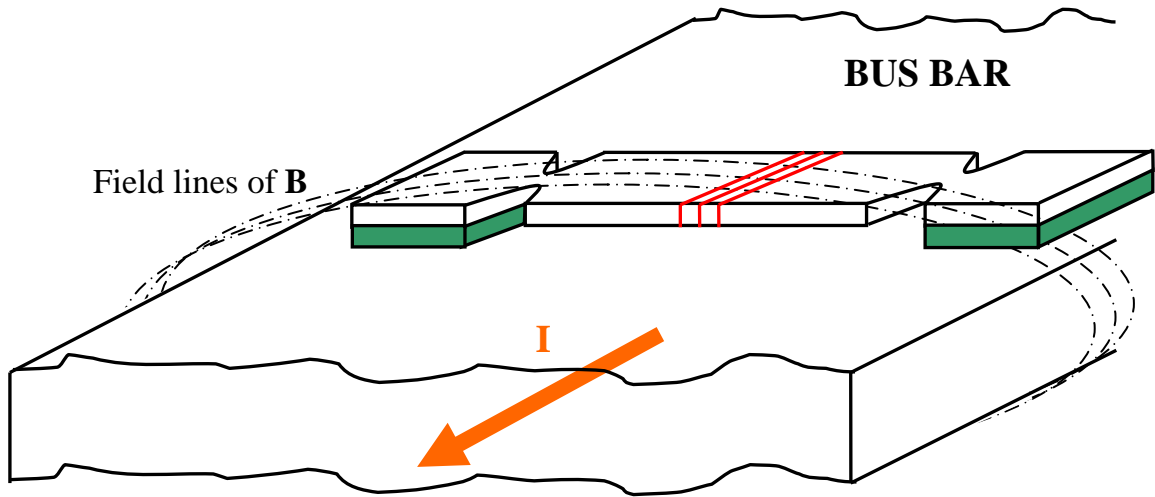


**Figure 12: The sensor in its environment. The coils (in red) receive a magnetic flux that varies in time as they move in a non-constant field**

### **2.3- Simulation of the magnetic field $B$**

Since the bus bar has a rectangular section, and inasmuch as the device will be operating near the conductor, it is predictable that the field  $B$  will be quite different from that of our starting hypothesis. Nevertheless, the latter was very useful as a tool for a rough validation of the concept and for dimensioning.

This section presents the result of the simulation conducted with a piece of software named FEMM (Finite Elements Method for Magnetism).

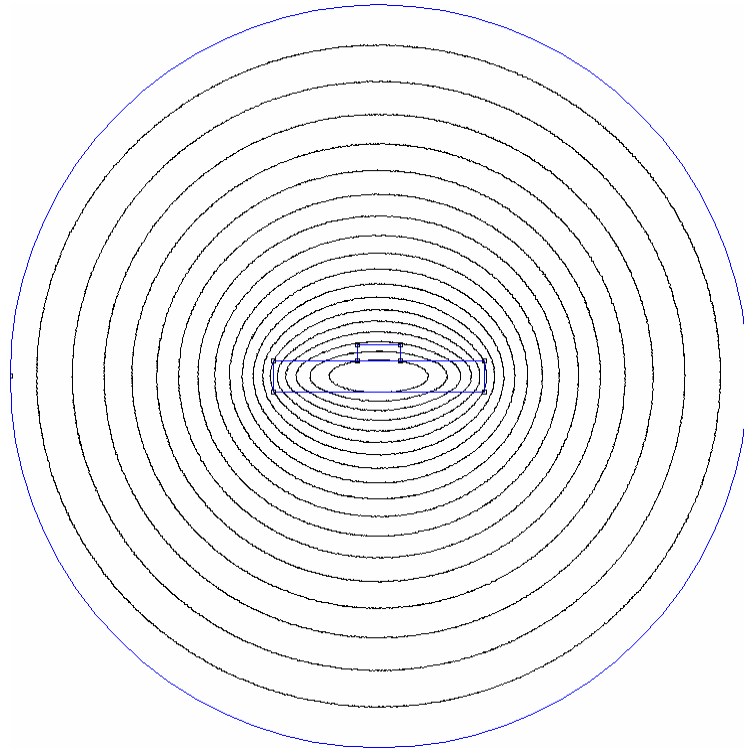


**Figure 13: Field lines surrounding the bus bar**

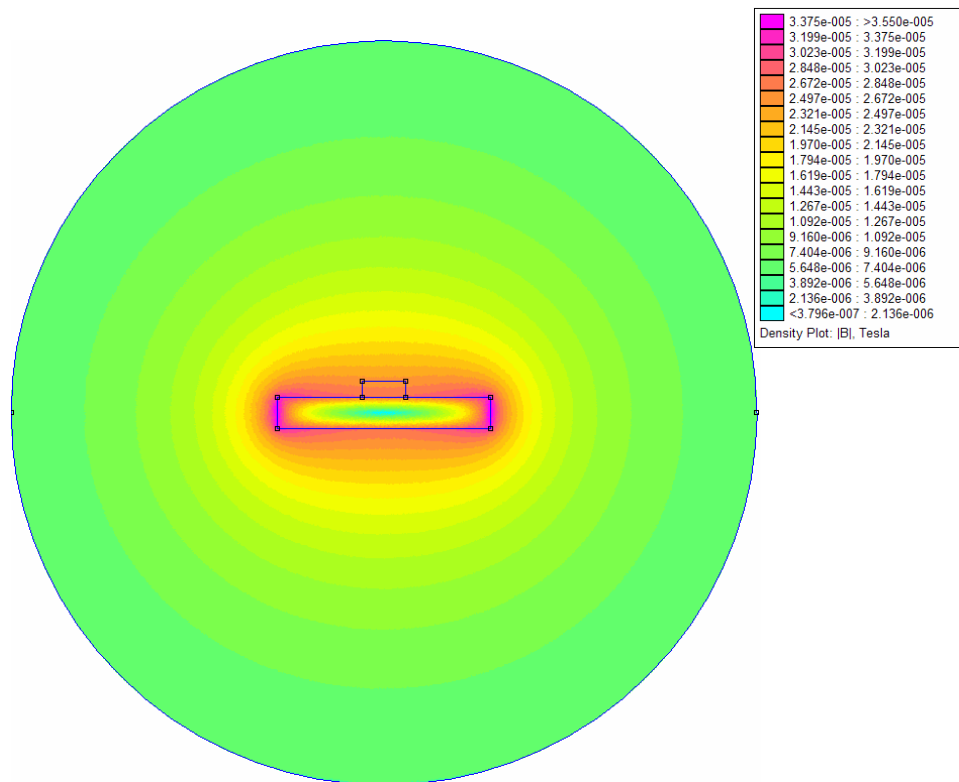


**Figure 14: Density of flux surrounding the bus bar**

The area of simulation has a radius 40 mm, and an asymmetric boundary condition. The rectangle in the middle represents the bus bar, taken as an amagnetic copper conductor of cross section 3 mm by 20 mm. All the rest of the simulation area is considered as air and the small rectangle above the bus bar is a place of very thin mesh.

The configuration is a planar problem, assuming that this plane is far enough from the ends of the bus bar. As a matter of fact, at this stage of the study, a precise modelling of the electromagnetic environment is outside of the scope.

In addition, despite the two axes of symmetry, FEMM did not easily allow reduction of the simulation area by four.

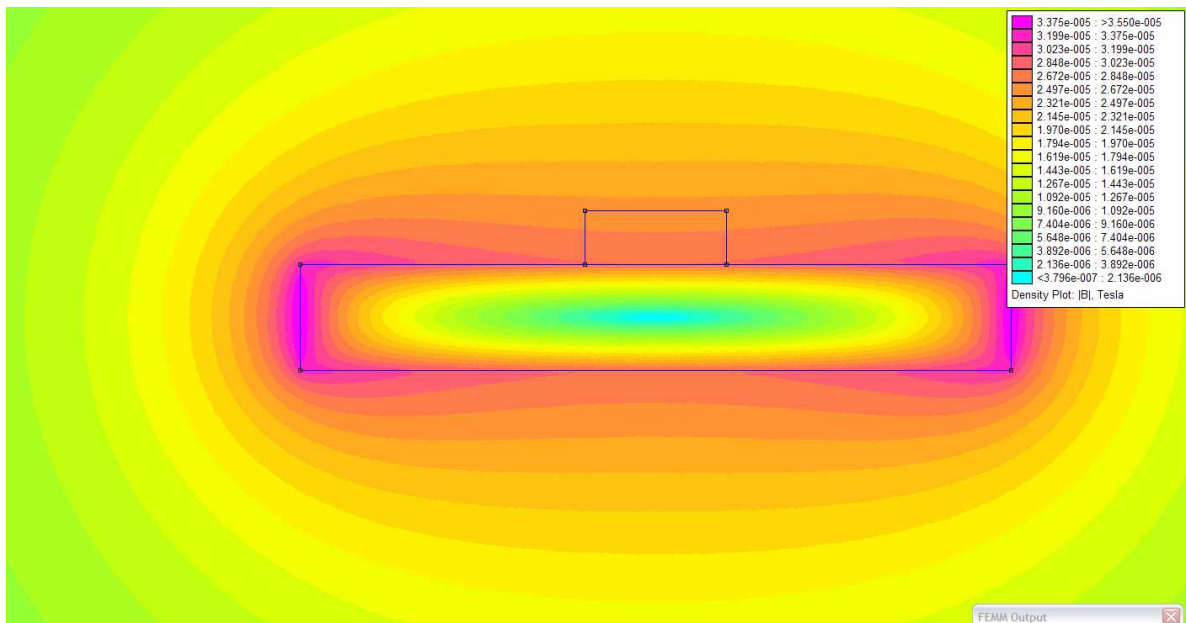


**Figure 15: The magnetic flux near the conductor**

The data was extracted to create graphs for interpretation of the simulation results. **Figure 16**, **Figure 17** and **Figure 18** give these details on the magnetic field in the area contained in the small rectangle above the bus bar.

At first sight, this location does not seem to be the most favourable for the sensor because it is not the place with the highest gradient of  $\mathbf{B}$ . Both highest flux and gradient of  $\mathbf{B}$  are located on the sides of the bus bar. However, it is not a question of orders of magnitude as one can see on the colour scale for the flux.

This is illustrated in **Figure 19** and **Figure 20**. These figures show the analysis of the data of a previous simulation, which has been conducted with a bus bar of dimensions 6 mm x 40 mm, a thicker mesh and a full range current (1000A). Data is collected in both the horizontal direction  $x$  and the vertical direction  $y$ . The ratio between the maximum gradient in the  $x$ -direction and the maximum gradient in the  $y$ -direction was around 3.5. This is probably not advantageous enough to compensate the problems of sensitivity to the location, which is much higher if the device is placed on the side. As a matter of fact, the value of the gradient is more or less constant in the first case whereas it is not at all in the second. And considering the size of the OC device, the large side of the conductor appears to be more convenient.

Thus it appears more beneficial to install the sensor on the vertical axis of symmetry, i.e. in the middle of the area contained in the small rectangle. This is why this focused study is conducted only in this area.

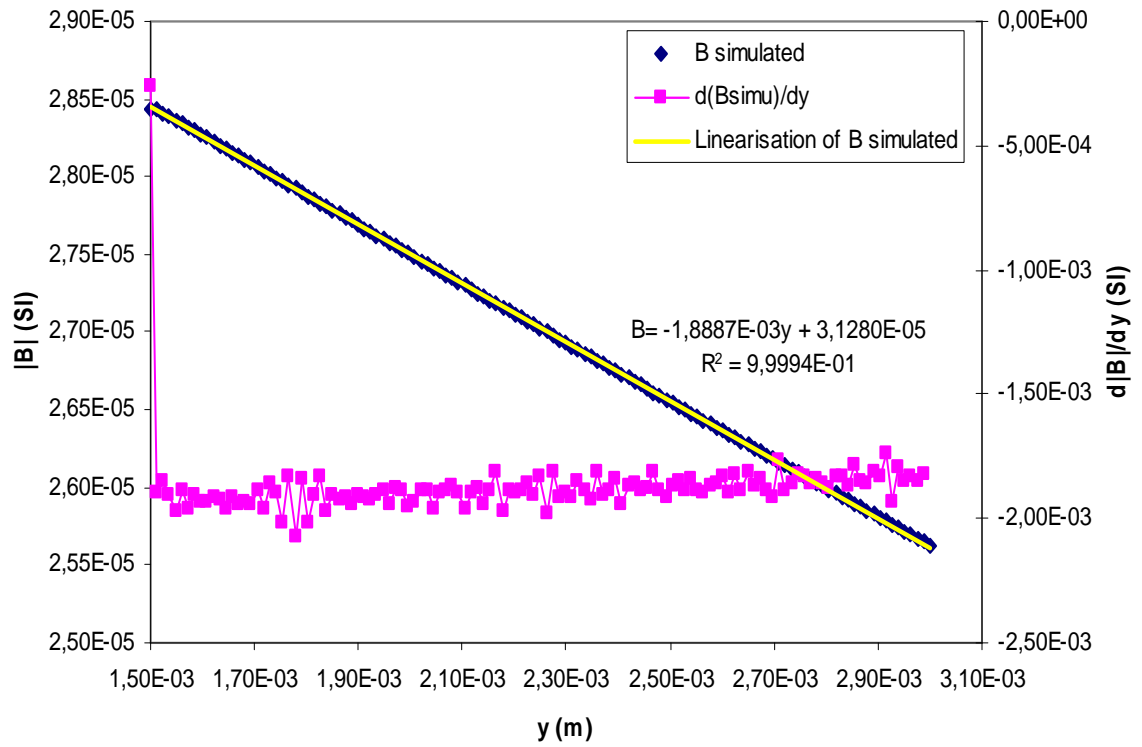


Figure 16 : Magnetic field B simulated, linearization and gradient

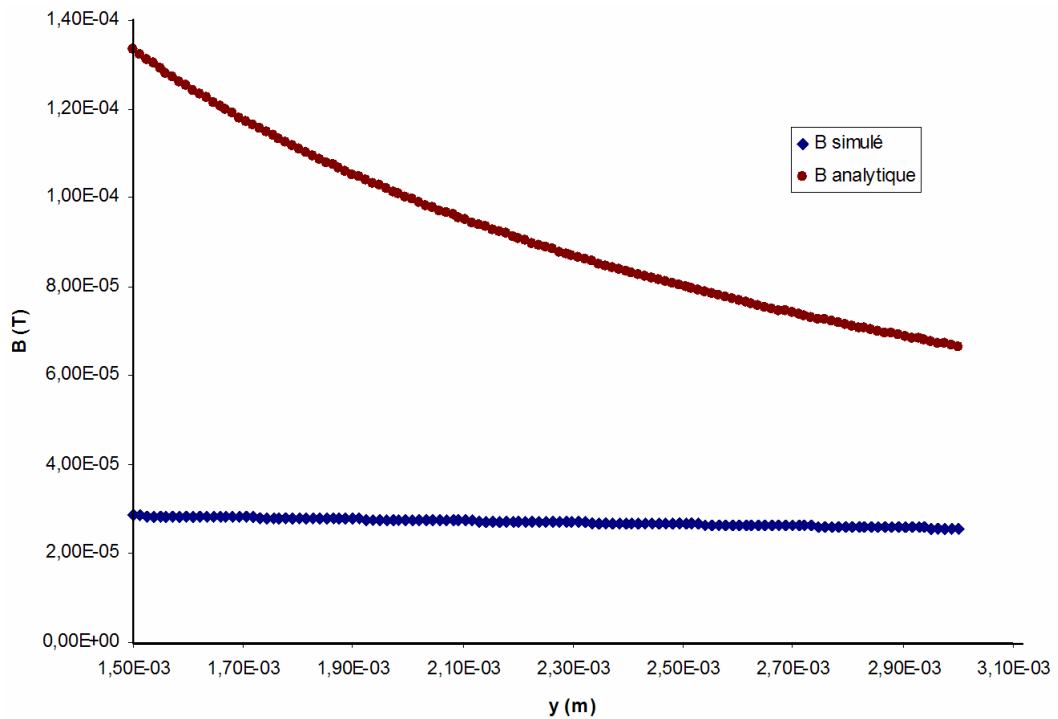


Figure 17: B from simulation in comparison to expected values from analytical model

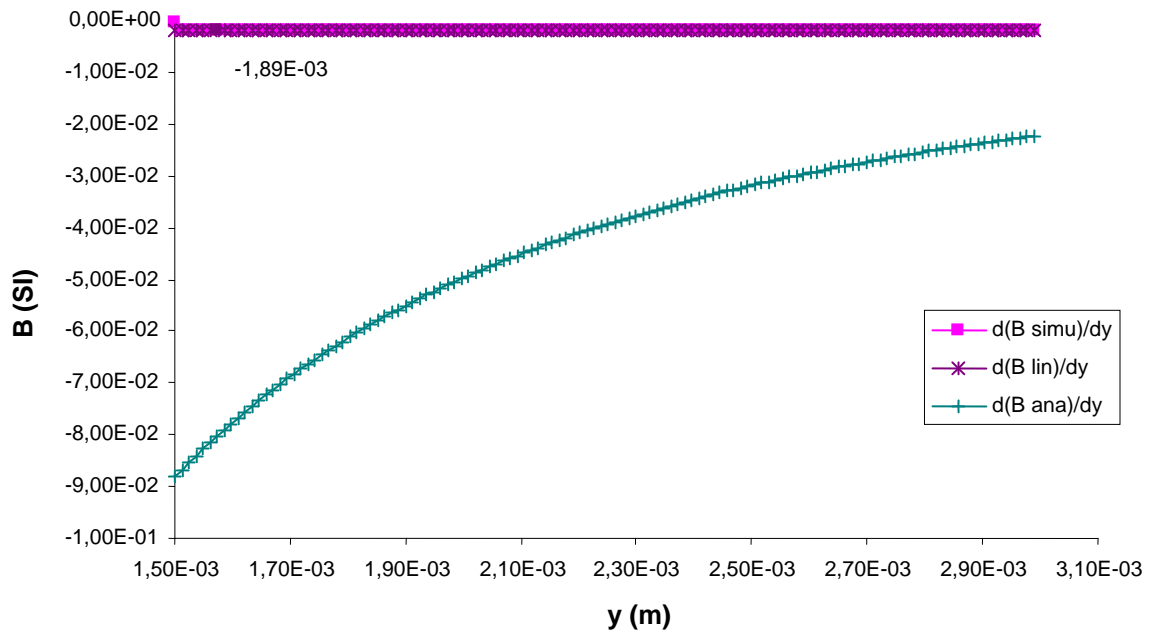


Figure 18 : Gradient B from simulation in comparison to expected values from analytical model

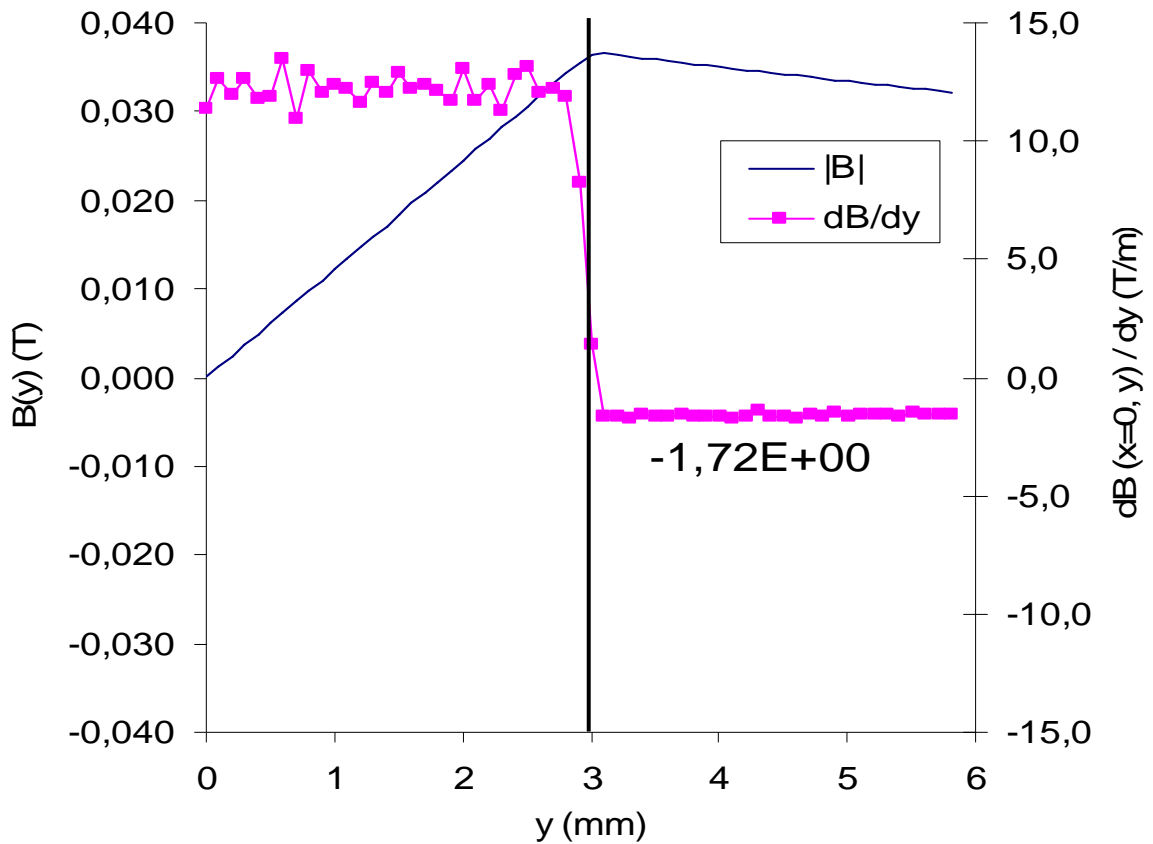


Figure 19 : profile of B and its gradient

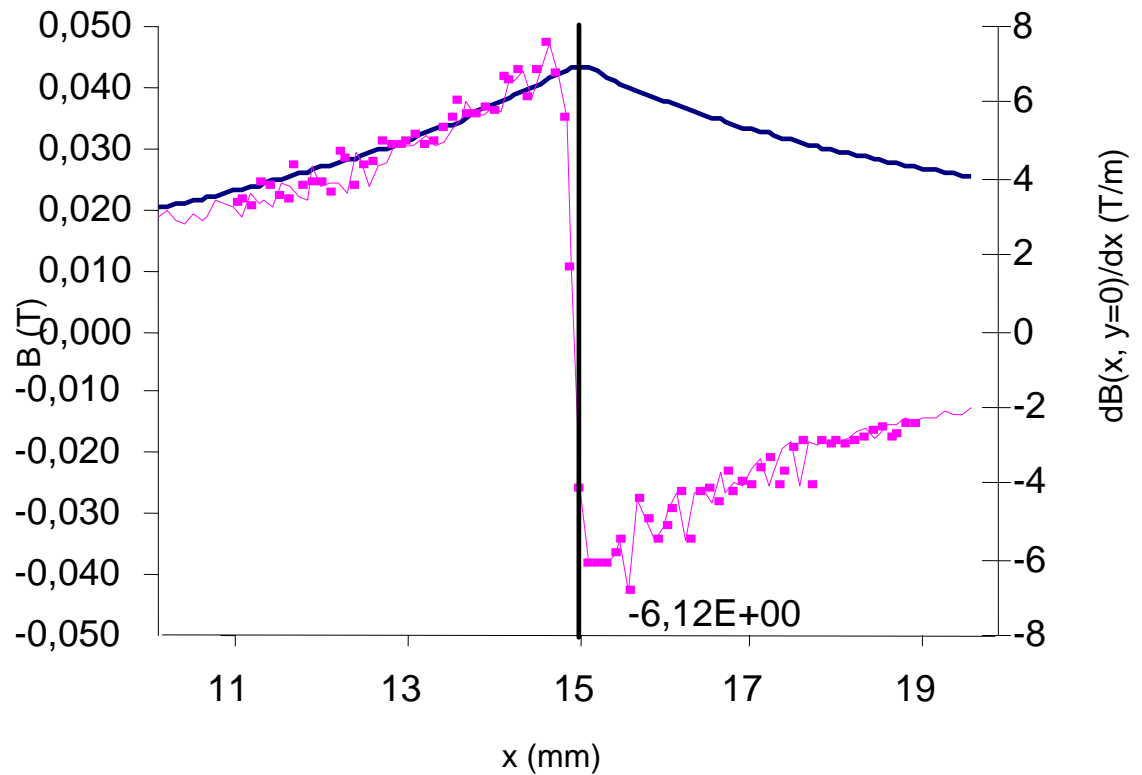


Figure 20: profile of  $B$  and its gradient

Again, the last two figures display data for another simulation with 1000 A of current and quite different dimensions for the cross section.

To clarify the notation,  $\mathbf{B}$  stands for  $|\mathbf{B}|$ , which is in all the situations of this study equal to  $\vec{B} \cdot \vec{h}$ , by symmetry. Indeed, the magnetic flux should always be normal to the axis of symmetry of the problem. In terms of flux one is interested in  $\vec{B} \cdot \vec{h}$ . Then “gradient of  $\mathbf{B}$ ” then stands for the derivative of  $(\vec{B} \cdot \vec{h})$  in the direction of interest (x or y).

It appears in the analysis of the data extracted from the simulations that **B** right above the bus bar is approximately 2.5 times smaller than the values given by the analytical model (**Figure 17**) and the gradient of **B** nearly twelve times smaller. This leads to resuming the calculations of sensitivity of the sensor with the results of the simulation as a starting point instead of the analytical model.

#### **2.4- Resuming the calculation with B simulated**

The first idea was to directly use the data extracted from the simulation in a Matlab program to perform the numerical calculation of the sensitivity. To achieve this, a text file is generated by FEMM and then converted by Excel into a table that Matlab can use directly.

This approach requires a large number of points in the simulation, and matching the integration points in Matlab with those extracted from the simulation. The consequence is that the syntax of the program becomes burdensome and inefficient. Furthermore the resolution obtained is not very good.

Since the linear regression of **B** is very well fitted in this area ( $r^2=0.99994$ , cf. **Figure 16**), it is more convenient and much more efficient to use this linear model of **B**.

A Matlab program given in **Appendix D** shows how the new values of the sensitivity for the oscillating coil are computed, using the dimensions previously given by the analytical approach in section **2.2**.



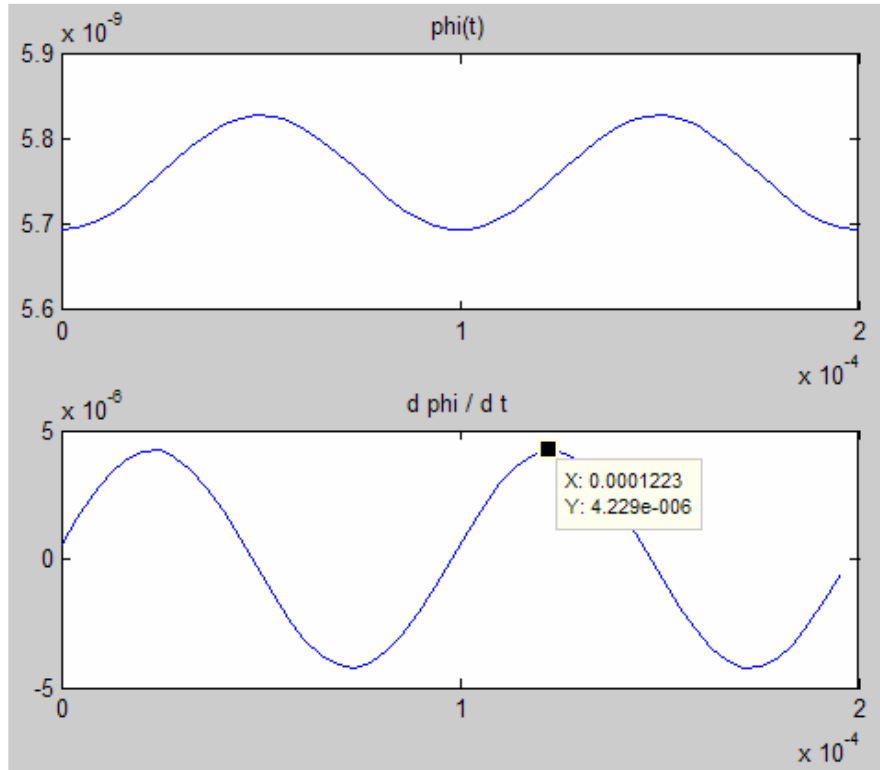


**Figure 21: Flux of B and its time-derivative obtained for the simulated and linearized field B**

One sees on the second graph displayed in **Figure 21** that the sensitivity has decreased by a factor 10 in comparison with that calculated with the infinite wire hypothesis. Considering the size of the device, it does not seem reasonable to multiply by 10 the number of coils. Increasing by this factor the gain of the OA is another possibility as well as increasing both parameters simultaneously.

Now as one has an analytical expression of **B** that comes from the linear regression, it is possible to reproduce the reasoning applied previously in order to derive a new value of  $d$ .

This reasoning is shown in **Annex 6**, and gives:

$$d = \sqrt{\frac{s\sqrt{3\rho E}}{2b_1\alpha\sigma_{crit}N}}$$

**Equation 12**

**Table 3: Design parameters of the OC considering the simulated magnetic field**

Parameters (SI)	$E$ (Mpa)	$\rho$ (kg.m <sup>-3</sup> )	$s_0$ (V.A <sup>-1</sup> )	$\alpha$	$\sigma_{crit}$ (MPa)	$N$	$b_l$
	2.00E+11	2.40E+03	5.00E-05	4	4.00E+08	100	1.89E-03
<b>d(m)</b>	<b>1.77E-03</b>						

As a result, one obtains the following dimensions:

**Table 4: Dimensioning of the OC considering the simulated magnetic field**

$2d$	$l$	$L/l$	$L$	$a$	$\omega$
3.54E-03	7.09E-03	10	7.09E-02	5.74E-04	1.83E+04

These dimensions are not satisfactory. The length is 7 centimetres, *i.e.* 3.5 times the width of the bus bar. To make this solution feasible, some design parameters have to be modified. If the OA gain is doubled to 200, then  $s_0$  becomes  $2.5 \times 10^{-5}$ . If  $N$  is set to 150 and  $L/l$  is set to 5, one gets:

**Table 5: Adjusted design parameters of the OC**

Parameters (SI)	$E$ (Mpa)	$\rho$ (kg.m <sup>-3</sup> )	$s_0$ (V.A <sup>-1</sup> )	$\alpha$	$\sigma_{crit}$ (MPa)	$N$	$b_l$
	2.00E+11	2.40E+03	2.50E-05	4	4.00E+08	150	1.89E-03
<b>d(m)</b>	<b>1.02E-03</b>						

**Table 6: Adjusted dimensioning of the OC**

$2d$	$l$	$L/l$	$L$	$a$	$\omega$
2.05E-03	4.09E-03	5	2.05E-02	8.29E-05	1.27E+05

This eventually leads to an acceptable result in terms of dimensions. Considering the violation of the beam hypothesis, it will be necessary to check the natural frequency of the beam by a finite element analysis.

## 2.5- Output signal

A frequency analysis of output signals is conducted. The output signal is  $e = -\frac{\partial \varphi}{\partial t}$ .

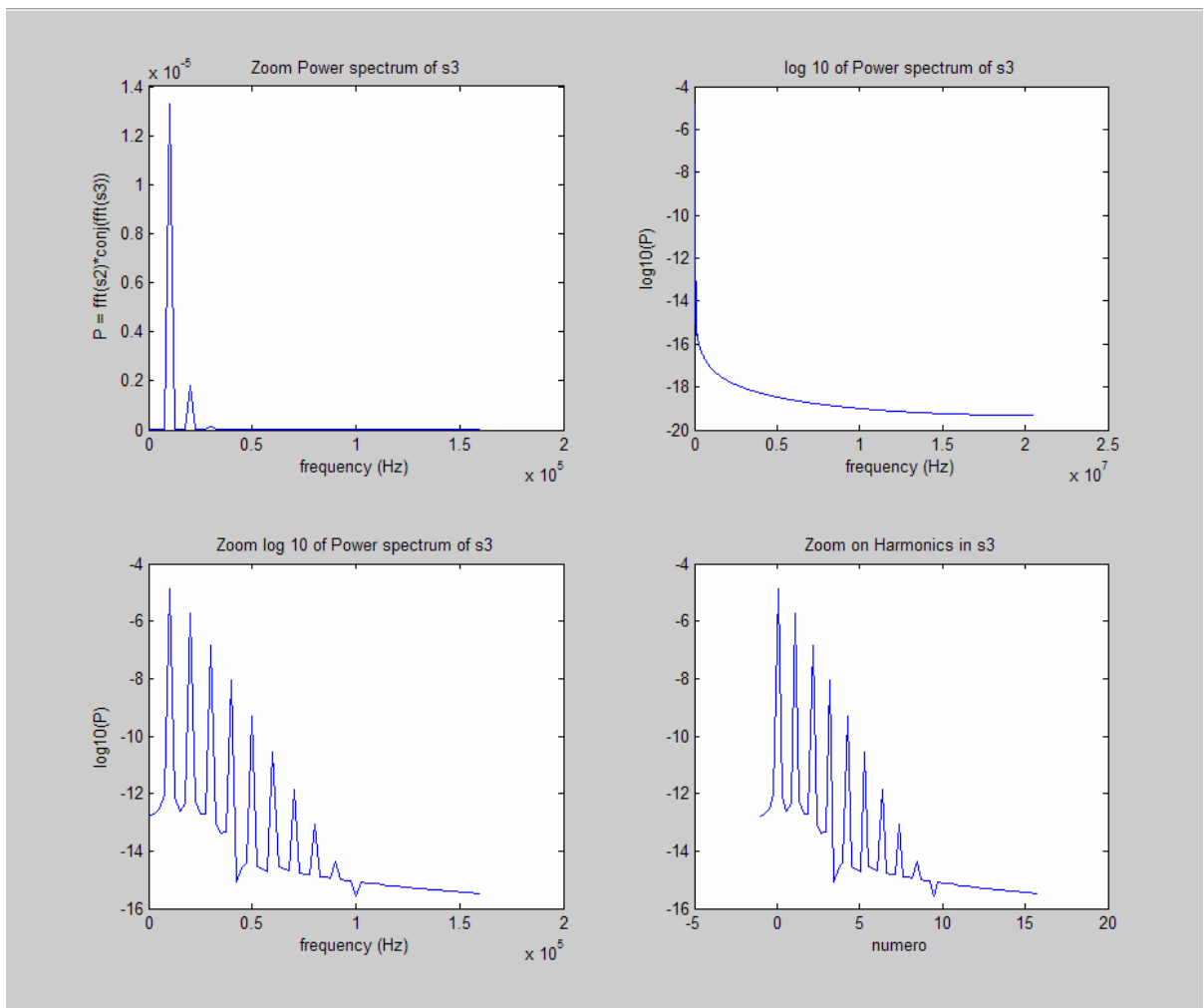


**Figure 22: Frequency content of the output signal**

The first analysis of frequency content has been conducted on the theoretical signal given by the Oscillating Coil and the infinite wire hypothesis. **Figure 22** comes from **Appendix C** where the program is given, along with more plots detailing the shape of the signal and the influence of simplifications made in the analytical calculations. Here it is already noticeable that the signal is almost a sinusoid. Each peak of the power spectrum is an order of magnitude lower than the preceding peak.

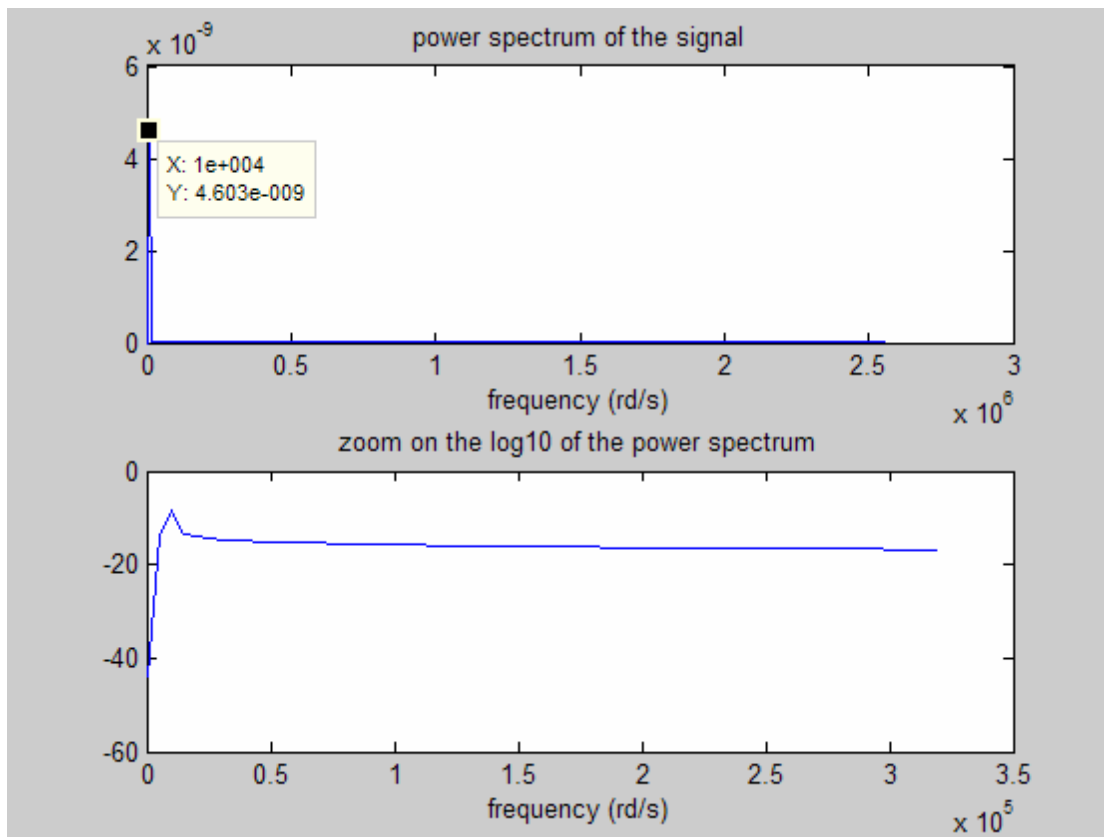


**Figure 23: Frequency content of the output signal**

**Figure 23** shows that for a linear **B** as provided by the simulation, the output signal of an Oscillating Coil is a sinusoid. The code is shown in **Appendix D**. To verify this fact, the second plot in this figure displays a zoom on the logarithm of the power spectrum.

Logarithm is used to check out hypothetic smaller peaks, and the horizontal zoom helps detaching the peak from the left side of the window so that it is easier to see. It is clear here that there is only one frequency, so the output ends up being a perfect sinusoid.

The signal will be processed at least for amplifying and if necessary for filtering. This filtering will get rid of noises with electromagnetic or mechanical origin. In the case of mechanical-based noise, one could consider a mechanical treatment. As stated when presenting the configuration of beams for the oscillating coil device, it could be beneficial to place an accelerometer detecting the parasite vibrations, treat its signal and send it back into the command of the actuator.

## CHAPTER 3: THE VARIABLE SECTION COIL (VSC)

### 3.1- Principle

While developing the Oscillating Coil presented in chapter two, another way of using Faraday's Law was investigated. It appears by expanding **Equation 1** as follows:

$$\frac{\partial \phi}{\partial t} = \frac{\partial \phi}{\partial S} \times \frac{\partial S}{\partial t} \quad \text{Equation 13}$$

Where  $S$  is the cross-sectional area of the coil.

That is to say one can obtain a time-variation of the flux by changing the cross-sectional area of the coil. Here the study is more at the geometric level, and the type of actuator is not defined. The rate of deformation of a piezoelectric crystal should be too small here, unless integrated into a mechanical oscillator that could bring large displacements. Other possibilities can be considered, such as using electrostatic forces or other techniques that become feasible at small scales. Two basic types of geometries were studied.

The first possibility explored is the diamond-shaped coil:

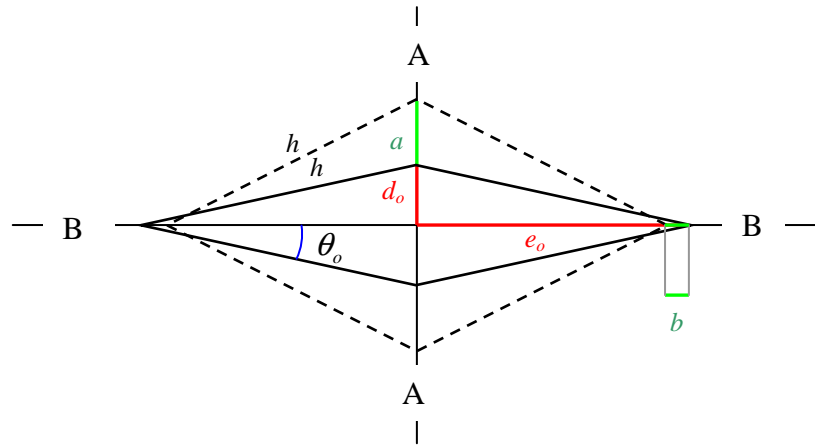


**Figure 24: Diamond-shaped VSC**

Where  $h$  is the hypotenuse of the triangle that constitutes each quarter of the diamond,  $d_o$  and  $e_o$  its initial sides,  $a$  and  $b$  the respective elongations of these sides.

This idea happened to be already implemented as a mechanical motion amplifier for piezoelectric actuators<sup>2</sup>. One sees easily that it offers a good amplification of the motion ( $a > b$ ). The smaller  $\theta_o$ , the bigger amplification, but the bigger internal constraints as well, since the configuration gets closer and closer to a singular point. Note that at point A, high values of acceleration will be reached, especially in the case of a large amplification. But what is interesting to the study is the cross-sectional area change that will bring the flux variation. **Figure 24** shows that this geometry provides a significant area change.

The second possibility is the following:

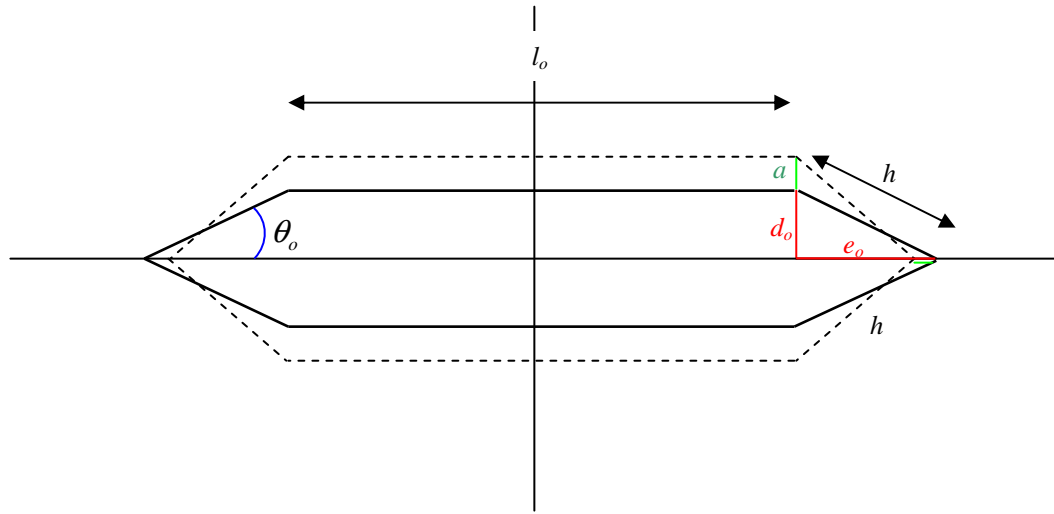


**Figure 25: Hexagonal shape VSC**

This hexagon is designed to convert the gain in displacement into a maximised gain of area. It behaves actually as the addition of a rectangle and a diamond that would have been split in two parts and apposed on at the ends of the rectangle. In this configuration, the angle  $\theta_o$  can be increased to  $45^\circ$  in order to allow large deformations around the configuration at rest. This will also result in a smoothing of both time-variations of  $a$  and of the area. Consequently there will be a dramatic decrease of acceleration in the upper bar, thus reducing the mechanical constraints on the system as well as the peak kinetic. As a consequence it also decreases the maximum elastic potential energy of this resonator. The last statement can be derived by approximating the resonator to a mechanical system subject only to conservative forces for which the total mechanical energy, being the sum of the kinetic energy and the potential energy, remains constant.



Now consider a magnetic field  $\mathbf{B}$  that decreases along the vertical axis. Fastening the coil on its upper bar allows concentrating the area change near the bottom bar, the one that experiences the highest  $\mathbf{B}$ , thus increasing the flux variation. Two other possibilities can be considered. The easiest way of mounting the device is to fasten the lower bar on the bus bar. A way that would reduce the accelerations in the system is to fasten the middle.

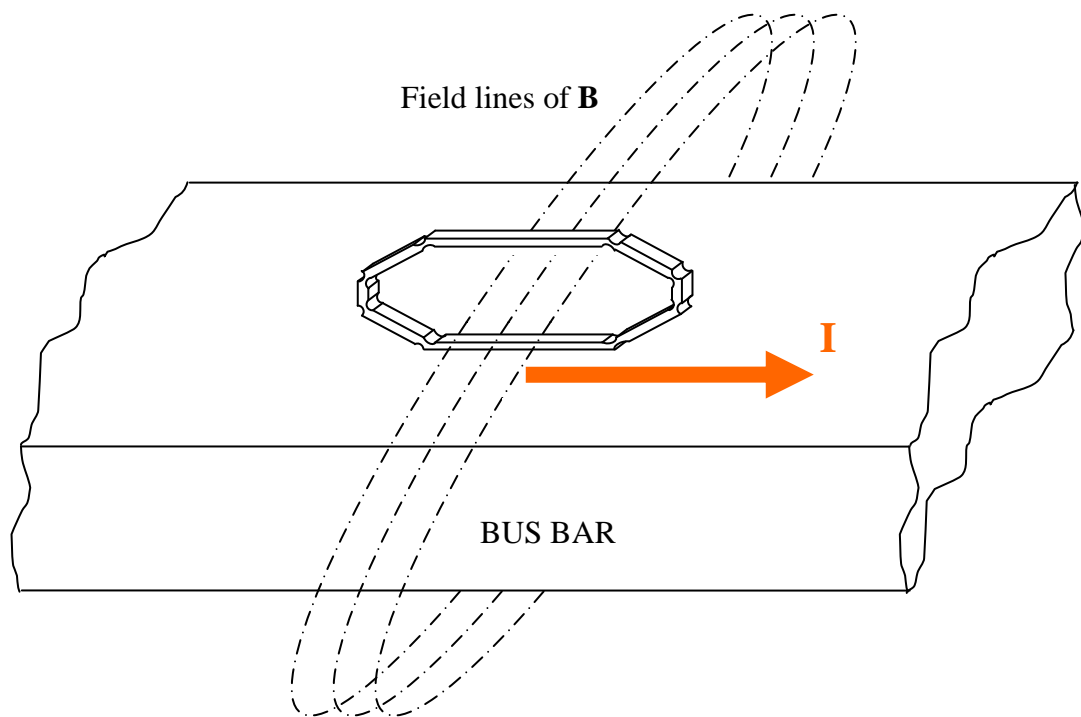


**Figure 26: The sensor in its environment. The coil receives a magnetic flux that varies in time as it deforms**

### 3.2- Sensitivity calculation, theoretical study

Integrating a field in  $1/r$  over a hexagon whose shape changes with time is nontrivial. Thus the calculations are directly performed numerically. The program is shown in **Appendix E**.

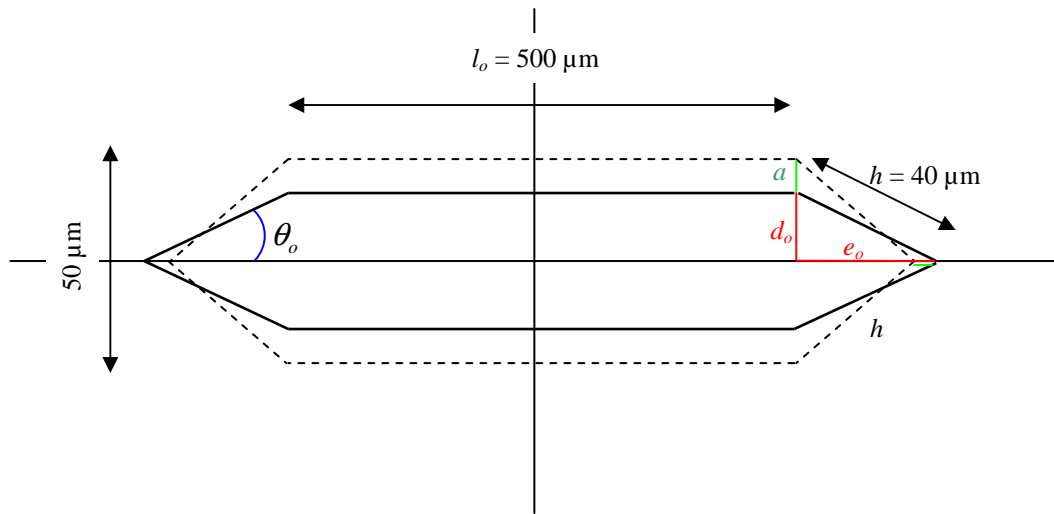


**Figure 27: Example of dimensions for hexagonal shape VSC based on B for an infinite wire**

To get sufficient deformation, the structure must vibrate, which requires stiffness. This stiffness can be integrated in the pivots if one chooses an appropriate technology, or come from a spring.

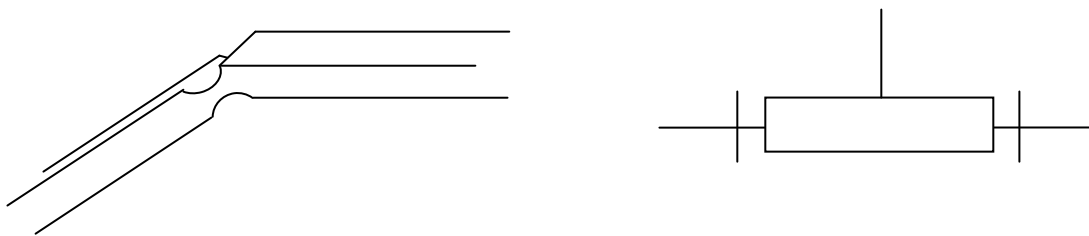


**Figure 28: Two types of articulations for VSC**

The technology used for the six pivots is not fixed. Two suggestions are made in **Figure 28**. The first one is a classical solution for small scale devices, while the second, figuring a cylinder into another cylinder, is more difficult to manufacture and requires adding a spring to the structure. In both cases, the natural frequency of the device will be considered as a parameter, considering that it can be widely adjusted, by using elastic to super-elastic materials, or by using springs.

Again, the main objective is a sensitivity of  $5 \cdot 10^{-5} \text{V/A}$ . Two cases are presented for very different scales. Here are the design parameters and the results in the form of curves.

**Table 7: Set of parameters for the VSC**

$\omega$ (rd/s)	$h$ (mm)	$l_o$ (mm)	td (%)	$N$
1,00E+04	1	5	4	6

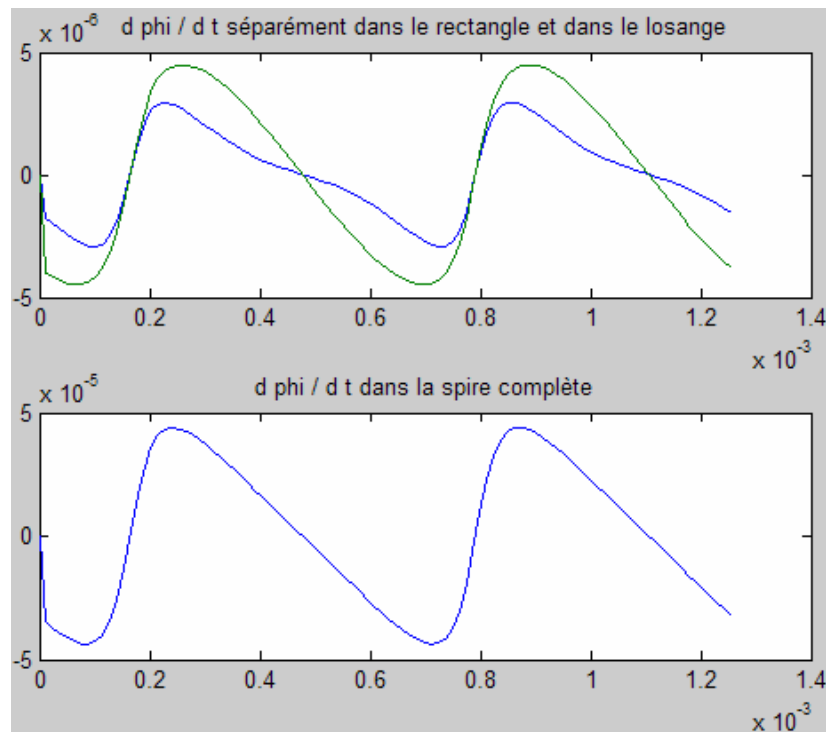


**Figure 29: Derivative of the flux separately in the rectangle and the diamond, then on the whole coil**

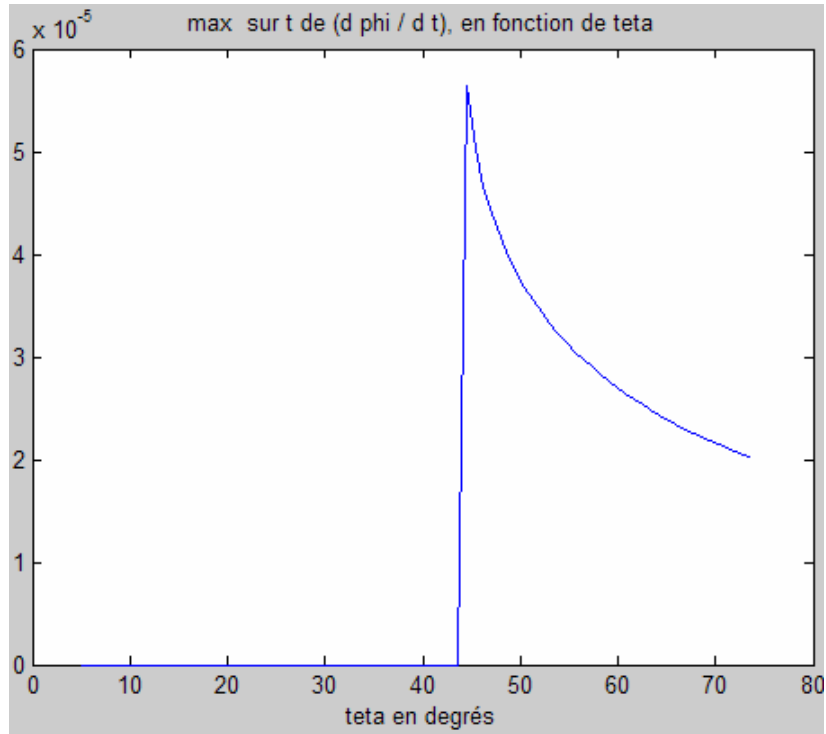


**Figure 30: Maximum in time of the derivative, in function of the angle at rest**

Following the reasoning explained before, this first configuration has been optimised to have its best performances around  $45^\circ$ , as shown in **Figure 30**. Now a second configuration is presented

**Table 8: Second set of parameters for VSC**

$\omega$ (rd/s)	$h$ (mm)	$l_o$ (mm)	td (%)	$N$
1,50E+06	0,05	0,5	0,2	12

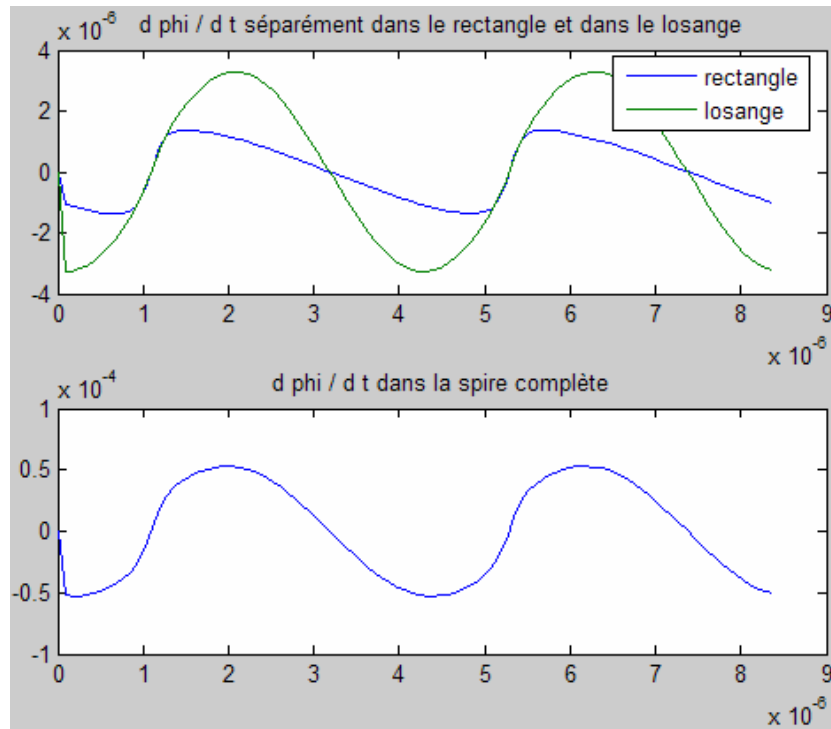


Figure 31: Derivative of the flux separately in the rectangle and the diamond, then on the whole coil

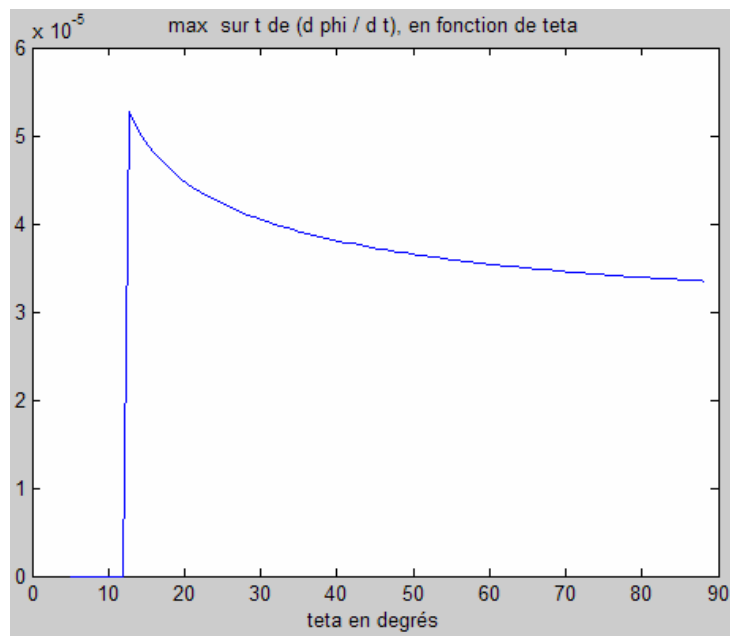
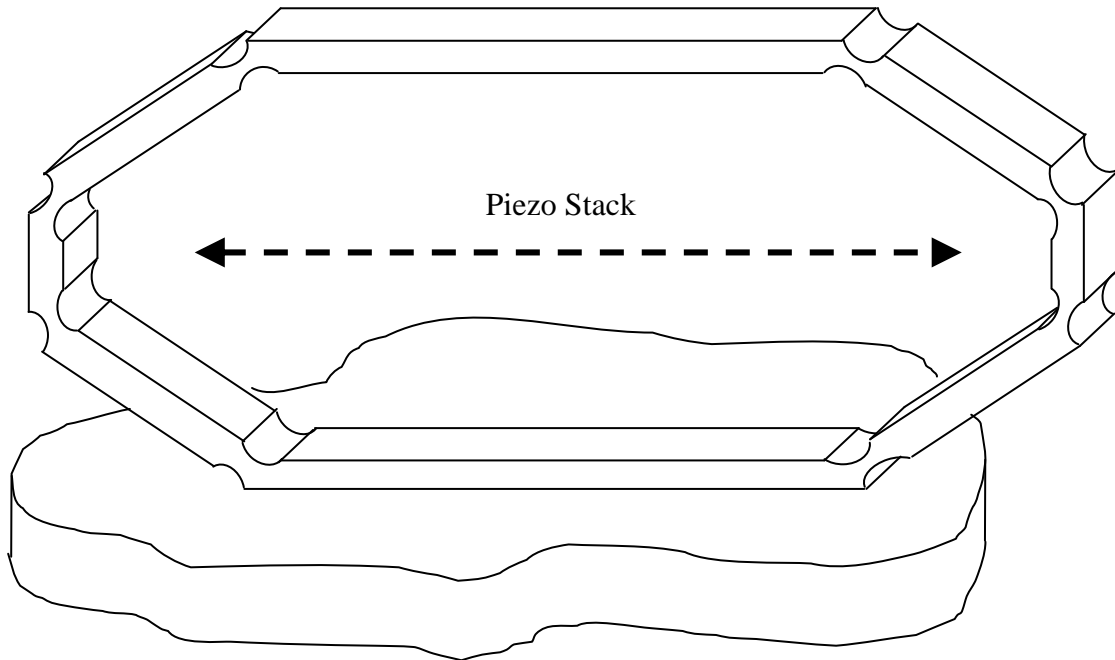


Figure 32: Maximum in time of the derivative, in function of the angle at rest

Here the rate of deformation  $td\%$  is chosen to be small (0.2%) because this deformation can be achieved by a stack type piezoelectric actuator.



**Figure 33: A hexagonal coil actuated by a stack**

For a larger rate of deformation as in the first set of parameters it would be necessary to use a different actuating principle, such as a resonator placed on the top of the structure.

Surprisingly enough, in both cases presented above the flux time-variation is larger in the diamond part than in the rectangle. This may be because the “dead surface”, i.e. the part of the surface that remains always open, is proportionally larger in the rectangle than in the diamond. This points out the effect of the “dead surface”. One sees again that the aim is not to have the largest magnetic flux, but to have the largest variation of this flux. Thus

it appears that the device, having a large “dead surface”, could be highly improved by neutralising it.

All these results are based on the infinite wire hypothesis, considering that the magnetic field  $\mathbf{B}$  decreases as  $1/r$ . It is then necessary to check how closely this hypothesis corresponds to reality.

### 3.3- Resuming the calculation with simulated $\mathbf{B}$

For the Variable Section Coil the dimensions obtained previously in section 3.2 are used. To obtain the chosen sensitivity  $s_0$  with the same dimensions, the number of coils is set to 100. For such a number of coils it becomes complicated to simply reproduce the device by translation as shown in **Figure 34**. It would be necessary to use one or two of these devices as a support for a winding.

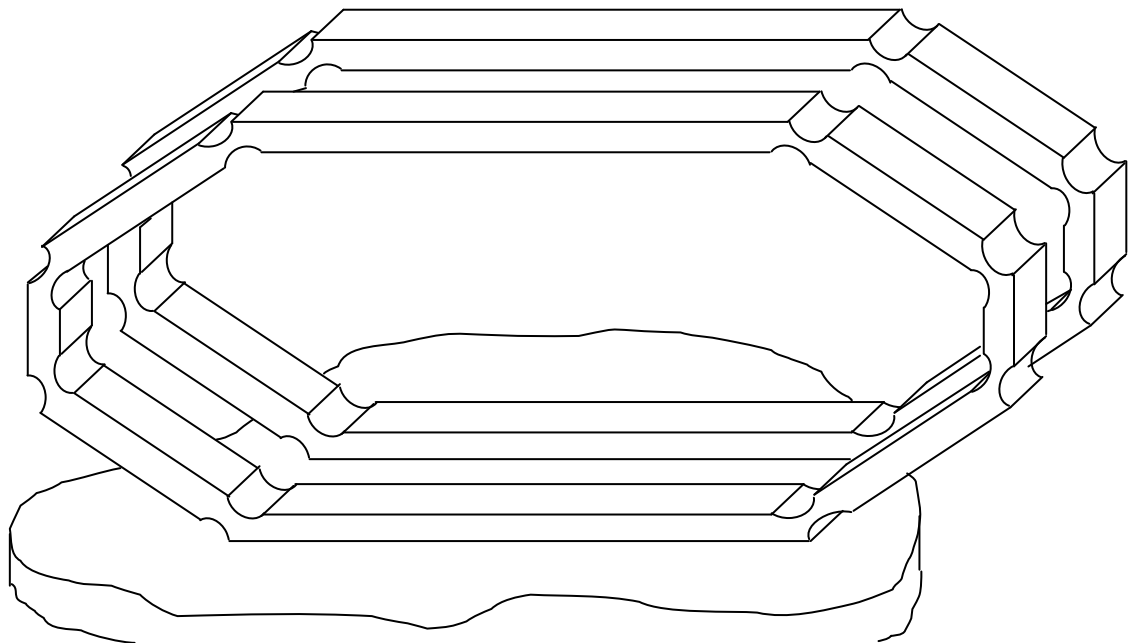


**Figure 34: Reproducing the coil by translation**

**Table 9: Set of paramaters for VSC**

$\omega$ (rd/s)	$h$ (mm)	$l_o$ (mm)	td (%)	$N$
1.00E+04	1	5	2	140

It appears that  $\omega$  should not be too high, since it would generate very high accelerations. Large deformations are preferable from the dynamics point of view. The Matlab code used for deriving these parameters from the calculation of sensitivity is shown in **Appendix F**, and displays the following results.

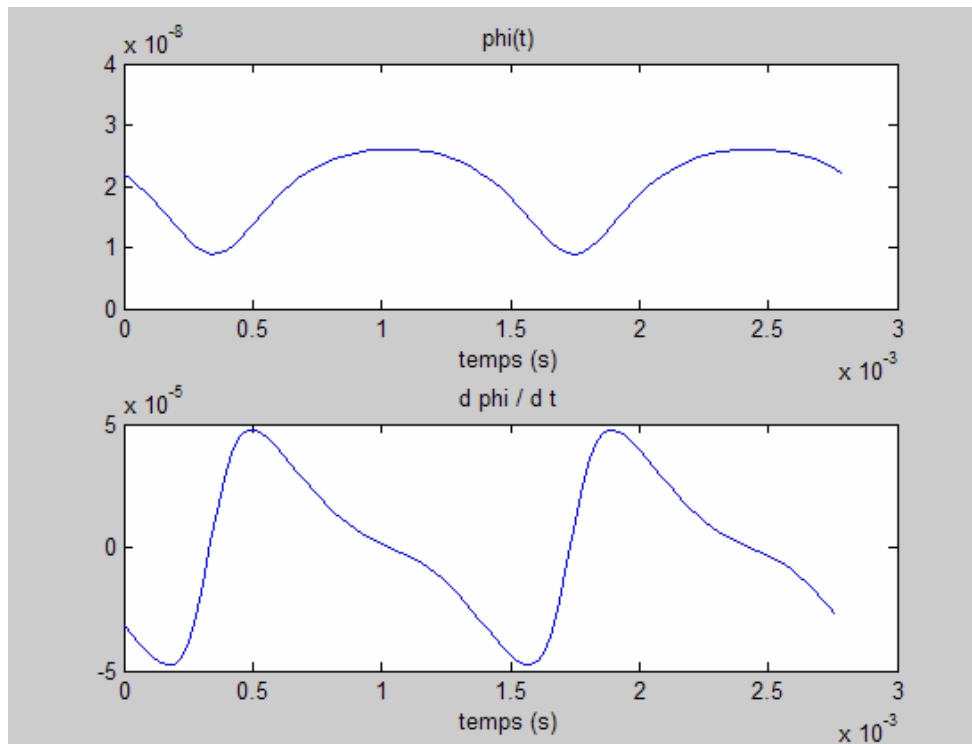


**Figure 35: Magnetic flux in the coil and its time derivative**



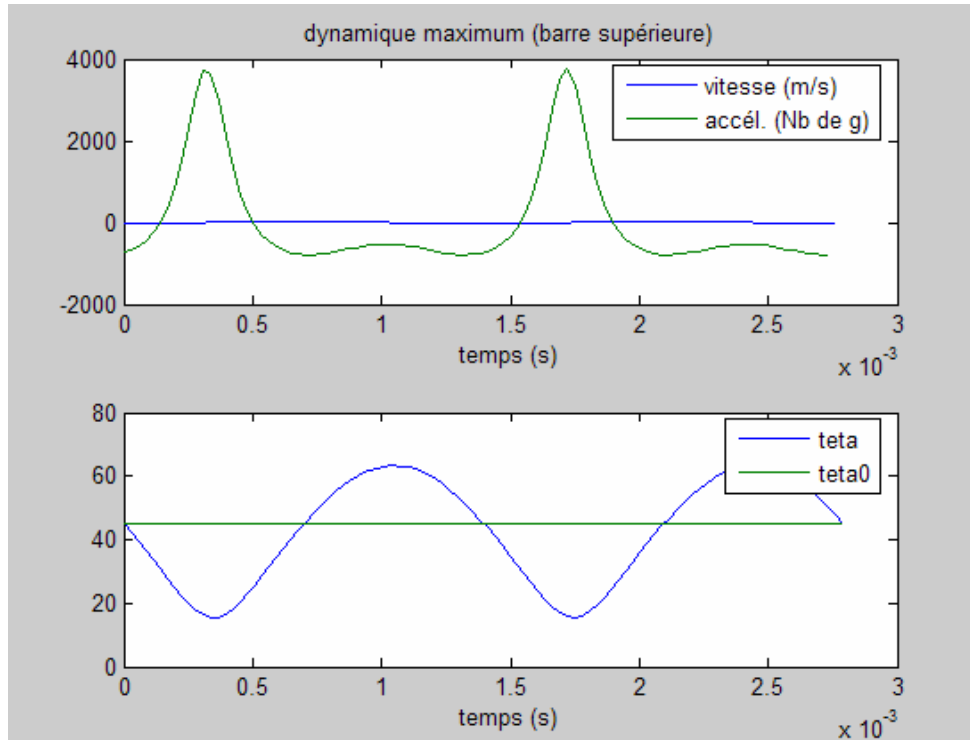


**Figure 36: Dynamics and kinematics in the coil**

The top graph in **Figure 36** introduces dynamics considerations. One can see that the device experiences very high acceleration. More details about the geometry and materials should be fixed in order to get further information about forces and stresses involved. This would allow establishing whether the actuator can supply enough power to impose the deformation. Most likely, it will be necessary to take into account the inertia of the structure beforehand in order to know the actual deformation, instead of considering that the actuator can impose its sinusoidal variation of length. This would push towards smoothing the acceleration.

As previously stated, the maximum acceleration can also be reduced by fixing the centre of the coil instead of the bottom.

Such a rate of deformation as that considered in the last calculations (2%) requires a different type of actuation than a transversal piezoelectric stack. This would most likely be a structure using a resonator, which could generate very large rates of deformations. Then the implicit hypothesis of the program imposing a deformation at the lateral extremities is not realistic anymore.

Both shape and frequency of the output signal will strongly depend on the solution chosen and on the design parameters. In any case, it will be an alternating current. As one can see in **Figure 47**, it will not be a sinusoid for the VSC solution. At least not in the case of a deformation imposed to be sinusoidal at the lateral extremities of the coil.

## CHAPTER 4: THE ROTATING COIL PLUS STATIC COIL (RC+SC)

The search for an actuation principle of the Variable Section Coil that would both induce a smooth variation of flux and exploit the whole surface of the coil without “dead area” led to another idea. Instead of changing the cross-sectional area of a coil that would stay oriented so as to face the field line, the coil could be driven in rotation, in order to be successively “open” to the magnetic flux or “closed”. That way, the variation of the flux would operate on the entire surface of the coil and be smooth. The faster the spinning, the higher output. Internal efforts would be reduced to possible contact-generated efforts at the links and those due to centripetal acceleration.

### 4.1- Principle

#### 4.1.1- The Rotating Coil as a first approach

At first, the concept is as simple as stated above. A set of coils is deposited on a rotor placed in the field  $\mathbf{B}$  so as to be at each turn successively facing the magnetic field lines or parallel to them. The value of  $\varphi_r$  (the flux in the rotor) will then vary at each complete turn from full range to naught, then full range on the other face and naught again. Thus the flux  $\varphi_r$  is time-varying, even if the magnetic field  $\mathbf{B}$  and the current  $I$  are constant in time. In the following,  $\mathbf{B}$  and  $I$  will always be considered to be constant. As a matter of fact, this device can as well be used for AC current, and the following analysis will remain valid, provided that the frequency of rotation of the rotor is sufficiently higher than the frequency of the AC current to be measured. With this simple modelling, the

bandwidth grows with the parameter  $\omega$ , the frequency of rotation. This consideration is actually valid for all the devices presented in this thesis.

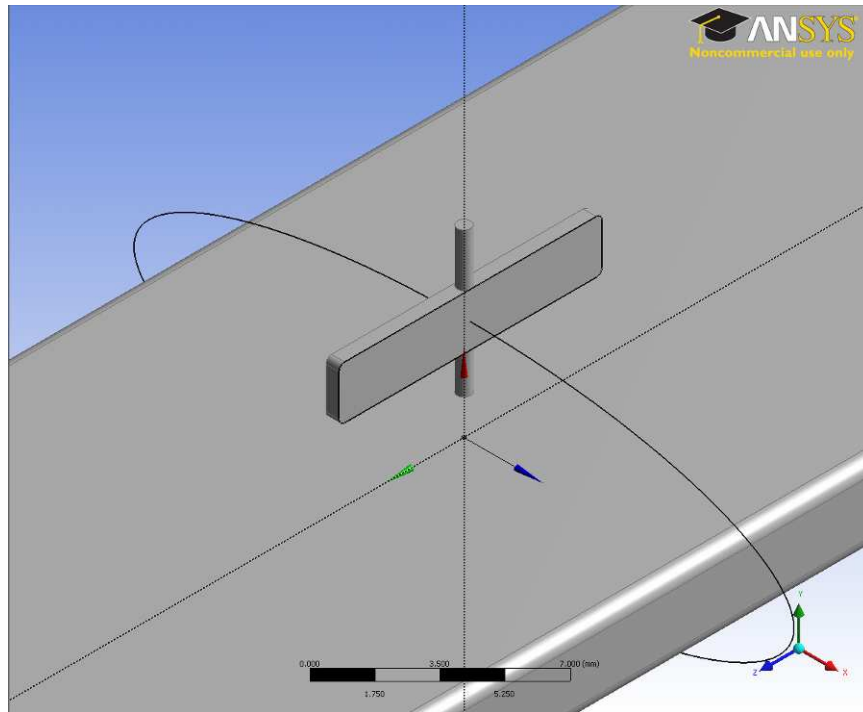


**Figure 37: Above the bus bar: rotor carrying a coil and facing a field line**

#### 4.1.2- Adding a Static Coil

Faraday's Law ensures that there will be on the rotor's set of coils an electromotive force  $e_r$ , image of  $B$ , and eventually of the current  $I$  in the bus bar. But collecting the signal on a spinning part may be challenging, and implies electrical tracks for contacts involving both mechanical and electrical losses, as well as aging and complicated assemblies. The RC+SC solution proposed here intends to avoid collecting the current on the rotor, by adding another layer of electromagnetic interaction, introducing a static coil on a stator.

For its carrying and e.m.f., the RC is also carrying a current  $i_r$ . This current circulating on the coil will be generating a magnetic field  $\mathbf{B}_r$  normal to the coil's plane and following its spinning motion. Another set of coils on the stator is intended to capture this spinning field  $\mathbf{B}_r$ , using Faraday's Law again. As a matter of fact, the phenomenon of the coil spinning in a fixed field is similar to this of a fixed coil in a spinning field. It is clear though that  $\mathbf{B}_r$  is several orders of magnitude under  $\mathbf{B}$ , since the rotor will carry a very small current  $i_r$ . The fact of having multiple coils carrying this current will compensate minimally this difference.

It is important to notice that the stator is sensitive to time-varying magnetic fields only, namely  $\mathbf{B}_r$ . But to avoid direct interaction with  $\mathbf{B}$  in case of an AC current to measure, the stator will be oriented so as to be parallel to the field lines of  $\mathbf{B}$ .

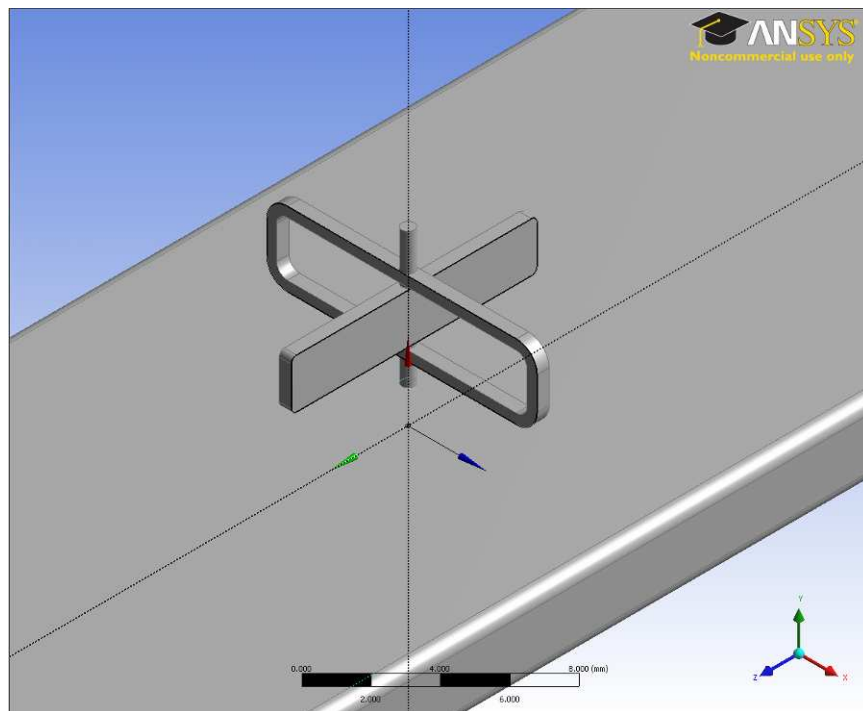


**Figure 38: above the bus bar: rotor and stator with a quarter of a turn**

## 4.2- Sensitivity calculation, theoretical study

### 4.2.1- Magnetic flux in the rotor and subsequent voltage and current

Considering that the flux of the magnetic field  $\mathbf{B}$  depends on the angle  $\beta(t)$  between this vector and the vector element of surface, Faraday's Law can be expanded so as to let this angle appear:

$$\frac{\partial \varphi}{\partial t} = \frac{\partial \varphi}{\partial \beta} \times \frac{\partial \beta}{\partial t} \quad \text{Equation 14}$$

With: 
$$\beta(t) = (\vec{B}, \vec{S})(t) = \omega.t + \alpha \quad \text{Equation 15}$$

And: 
$$\varphi_r = \iint_S \vec{B} \cdot d\vec{S} \quad \text{Equation 16}$$

$$e_r = -\frac{d\varphi_r}{dt} = -\frac{d}{dt} \iint_S B(x, y, z) \cdot \cos(\beta(t)) \cdot dx \cdot dy \quad \text{Equation 17}$$

It is reasonable to consider a space average of  $B(x, y, z)$  since the coil does not deform nor move in the vertical direction and since the value of the field just above the bus bar does not vary significantly along the conductor's width.

Moreover, as  $B$  can be considered constant in time, the e.m.f. becomes:

$$e_r = -B.S \frac{d}{dt} \cos(\beta(t)) \quad \text{Equation 18}$$

The hypotheses made on  $\mathbf{B}$  will make it necessary to check this sinusoidal shape in the simulation conducted in **section** 4.3.2. By including the number of coils  $n_r$  on the rotor, the e.m.f. can be written as follow:

$$e_r = \omega.B.S.n_r.\sin(\beta(t)) \quad \text{Equation 19}$$

If  $R_r$  is the natural resistance of the coil, due to its resistivity, then the current  $i_r$  can finally be written:

$$i_r = \frac{\omega.B.S.n_r}{R_r} \sin(\beta(t)) \quad \text{Equation 20}$$

#### 4.2.2- Magnetic flux in the stator and sensitivity

The magnetic flux generated by the rotor is a complex function of the space. As a matter of fact, the winding is deposited on a printed circuit board constituting the rotor. Then it must be in-plane, what makes it a rectangular spiral. In order to increase the number of coils, rotor will be printed on both sides, with the consequence of improving the symmetry of the device. If necessary, the PCB can also be multi-layered, so as to increase the number of coils even more. In this context, even using Biot and Savart's equation to

estimate the field at one point would require quite heavy calculations. An analytical calculation of the field as a function of space is out of the question.

Since a strong simplification is required, let us assume that the magnetic field due to the current in the rotor's coil set,  $B_r$ , can be averaged inside the coil and approximated to:

$$B_r = \gamma \cdot i_r \cdot n_r \quad \text{Equation 21}$$

Where  $\gamma$  is a constant coefficient ( $\text{T} \cdot \text{A}^{-1} \cdot \text{turn}^{-1}$ ). This  $B_r$  is carried by a vector normal to the rotor and spinning with it. Then the e.m.f. on the stator,  $e_s$ , can be calculated.

$$e_s = -\frac{d\varphi_s}{dt} = -\frac{d}{dt} \iint_s \vec{B}_r \bullet \vec{dS}_s \quad \text{Equation 22}$$

**Equation 22**, where  $\vec{dS}_s$  is the vector element of surface of the stator, becomes, after calculations shown in details in **Appendix G**, becomes:

$$e_s = \frac{\omega^2 \cdot B \cdot n_r^2 \cdot n_s \cdot S^2 \cdot \gamma}{R_r} \cdot \sin(2\beta(t)) \quad \text{Equation 23}$$

It is important to keep in mind the different hypothesis, especially this concerning  $B_r$ . The section areas are also approximated to be the same for the rotating coil as for the fixed coil. Thus the formula is not directly usable for a full analytical optimization of the



design, but it can help getting an order of magnitude of the sensitivity. This formula is also meant to show the interesting parameters, and give an idea of the shape of the signal.

This analysis is based on a value of the magnetic field  $\mathbf{B}$  that has been extracted from previous simulations, and on an averaged value of  $B_r$  estimated through Biot and Savart equation. The objective to give orders of magnitude for the parameters so as to reach a sensitivity of  $5.10^{-5}$  V/A, which means 5V at full range including an amplifier of coefficient 100, leads to establish the set of parameters presented in the table below:

**Table 10: Set of parameters for RF+SC based on a full range for I**

(SI)	$n_r$	$B(1000A)$	$L$	$l$	$S$	$\omega$
<b>Rotor</b>	10	2,40E-02	1,00E-02	2,00E-03	2,00E-05	4,00E+03
<b>Stator</b>	$n_s$ 10000	Br 6,81E-05			2,00E-05	4,00E+03
<b>Rotor</b>	$d_r$ 9,00E-05	$e_r$ 1,92E-02	$R_r$ 5,88E-01	$i_r$ 3,27E-02	$j$ (A/m <sup>2</sup> ) 5,13E+06	$j$ (A/mm <sup>2</sup> ) 5,13E+00
<b>Stator</b>	$d_s$ 1,00E-07	$e_s$ 5,47E-02	$R_s$ 2,90E+08	$i_s$ 1,89E-10	2,40E+04	2,40E-02

s (V/A)	5,47E-05
---------	----------

In red are the design parameters,  $d_r$  and  $d_s$  are respectively the diameter of the conductor of the rotor and this of the stator. It is necessary to realize that an analytical model is very complicated to establish for this problem, and requires many hypotheses and approximations. The value of  $B$  is estimated from the simulation conducted with FEMM.

### 4.3- New simulation for a three dimensional magnetic problem

#### 4.3.1- Limits of the software and decomposing the analysis

This next step is then to conduct a magnetic simulation. The electromagnetic problem as presented in **Figure 37** and **Figure 38** is not plane since the rotor introduced evolves out of a cross-section plane of the bus bar. A three-dimensional software is then required. In absence of accessible software to conduct time-dependant electromagnetic simulation, the magnetostatic solver of ANSYS will be used. This implies a non-trivial process of simulations.

First of all, the problem will be decomposed according to a quasi-static approach, which means that the simulation of the flux  $\varphi_r$  of  $\mathbf{B}$  in the rotor and the following e.m.f. and current on one hand and the subsequent flux  $\varphi_s$  of  $\mathbf{B}_r$  in the stator along with the following output voltage on the other hand, will be simulated separately. So the first set of simulations will establish the current  $i_r$  in the rotor to validate the analytical expression of it, and the second set of simulations will establish the output voltage  $e_s$  in the stator. Moreover, these two sets will actually decompose into a number of static simulations with different angular positions of the rotor so as to reconstitute the signals from these points.

As a consequence of this quasi-static approach, phase shift is neglected. This can be justified by the fact that the time-constants of electromagnetics can be neglected in front of these of the dynamics.

#### 4.3.2- Magnetic flux in the rotor and subsequent voltage and current

The simulations are conducted using the parameters proposed in **Table 10**. As the outcome of the modelling for  $e_r$  and  $i_r$  presented in **Equations 19** and **20** is extremely simple and as the one hypothesis that an average  $B$  can be used is very reasonable, the set of simulations only contains 7 points to explore a quarter of a turn of the rotor. Once it is checked that a sinusoidal model fits perfectly, the rest of the turn is obtained by symmetry.

**Table 11: Average flux density on the rotor in function of the angle**

Angle (deg)	Angle (rad)	avg flux density	cosine model
0	0	2,42E-02	2,39E-02
15	0,261799	2,33E-02	2,31E-02
30	0,523599	2,07E-02	2,07E-02
45	0,785398	1,67E-02	1,69E-02
60	1,047198	1,16E-02	1,20E-02
75	1,308997	6,06E-03	6,19E-03
90	1,570796	6,60E-05	1,46E-18

Flux density is the way ANSYS names the magnitude of  $\mathbf{B}$  or the component asked for. Here it corresponds to the component along the vector normal to the rotor. This way, and since the meshing of the conductor has a perfectly regular size, it is sufficient to extract this flux density from all the points of the meshing of the surface of the rotor, average it, and multiply by the surface, so as to get a numerical equivalent to the integral over  $S$  of the scalar product between  $\mathbf{B}$  and the vector element of surface, that-is-to-say the flux  $\varphi_r$  in the coil.

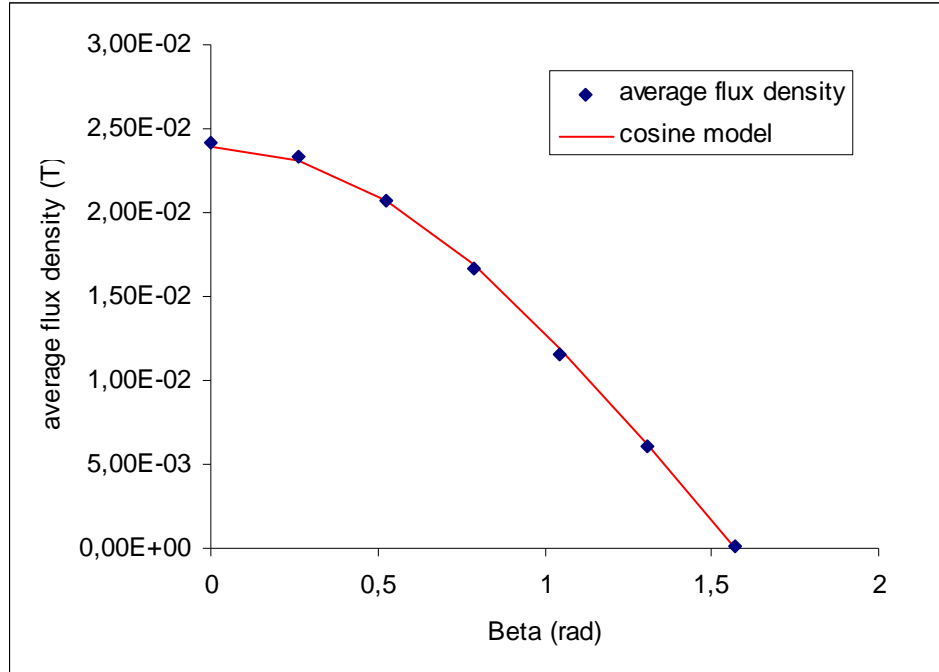


**Figure 39: Data and modelling for the average flux density on the rotor**

The cosine model fits the data points closely and has an amplitude of  $2.39 \times 10^{-2}$  T, which validates both the value of  $B$  used in the analytical sensitivity calculation (**Table 10**,  $2.40 \times 10^{-2}$  T) and the expected cosine shape of  $\varphi_r$ . As a consequence,  $e_r$  and  $i_r$  are validated as well, since they are derived straightforwardly from  $\varphi_r$ . The updated values are very similar to the previous ones, and summarised in the following table:

**Table 12: Electromagnetic characteristics of the RC+SC after the simulation for  $\varphi_r$**

(SI)	$n_r$	$B(1000A)$	$e_r$	$i_r$
<b>Rotor</b>	10	2,40E-02	1,92E-02	3,27E-02
	$n_s$	Br	$e_s$	$i_s$
<b>Stator</b>	10000	6,81E-05	5,47E-02	1,89E-10
s (V/A)		5,47E-05		

### 4.3.3- Magnetic field of the rotor

Knowing the current  $i_r$  on the rotor in function of the angular position allows conducting the second part of the simulation task. It consists in using this current to reconstruct the field  $\mathbf{B}_r$  for the different positions of the rotor. In as much as the analytical model built to predict the flux  $\phi_s$  uses very simplistic hypotheses, in particular concerning the magnetic field of the rotor, more output points are needed, and the simulations will be spread over a whole revolution of the rotor.

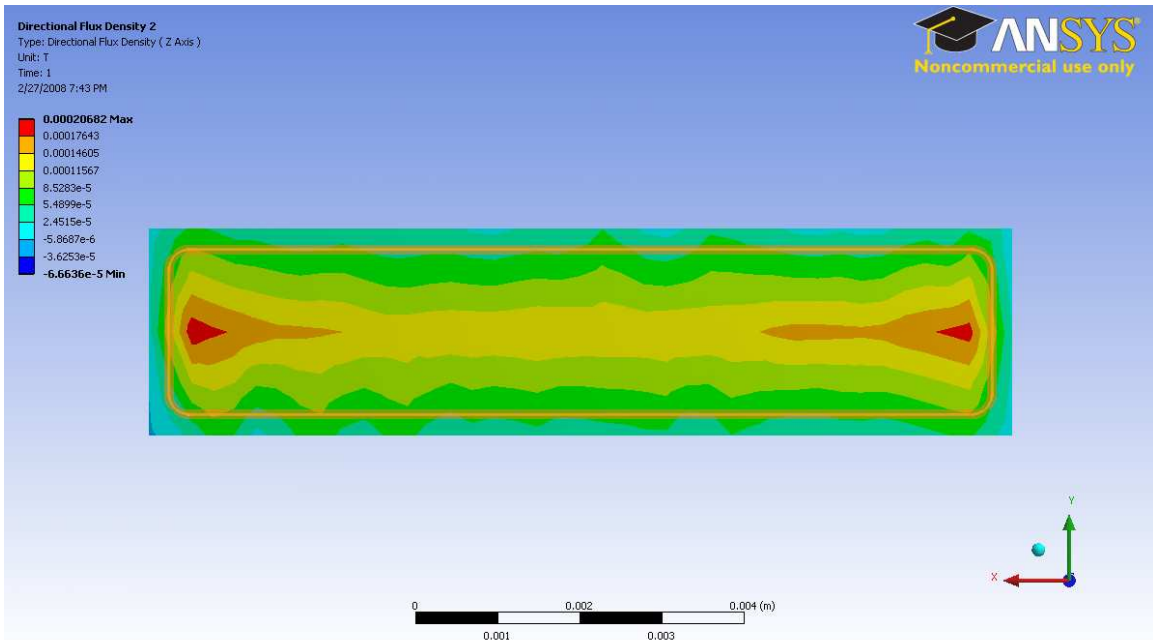


**Figure 40: Normal component of the magnetic field in the rotor's coil and in the immediate surroundings, for  $\beta = 90^\circ$**

#### 4.3.4- Magnetic flux in the stator and sensitivity

Thus, the interval  $[0, 2\pi]$  is discretized into 48 points. For the angles  $0$ ,  $\pi$ , and  $2\pi$ , the current  $i_r$  is naught since it is a sine function, so there is no simulation. For each the other 45 points, a simulation is conducted, where a geometry is generated with the actual position of the rotor, it is transferred in the magnetic simulation environment and loaded with the value of the current corresponding to the actual value of the angle  $\beta$ . Then the meshing is generated and the simulation is run. Similarly to the flux in the rotor in the previous section, the value of the component of the magnetic field  $\mathbf{B}_r$  normal to the stator is extracted at each point of the meshing of the stator. This meshing is made regular in size so the flux  $\varphi_s$  can be computed as the product between the average of the extracted values and the area of the coils of the stator, multiplied by  $n_r$  and  $n_s$ .

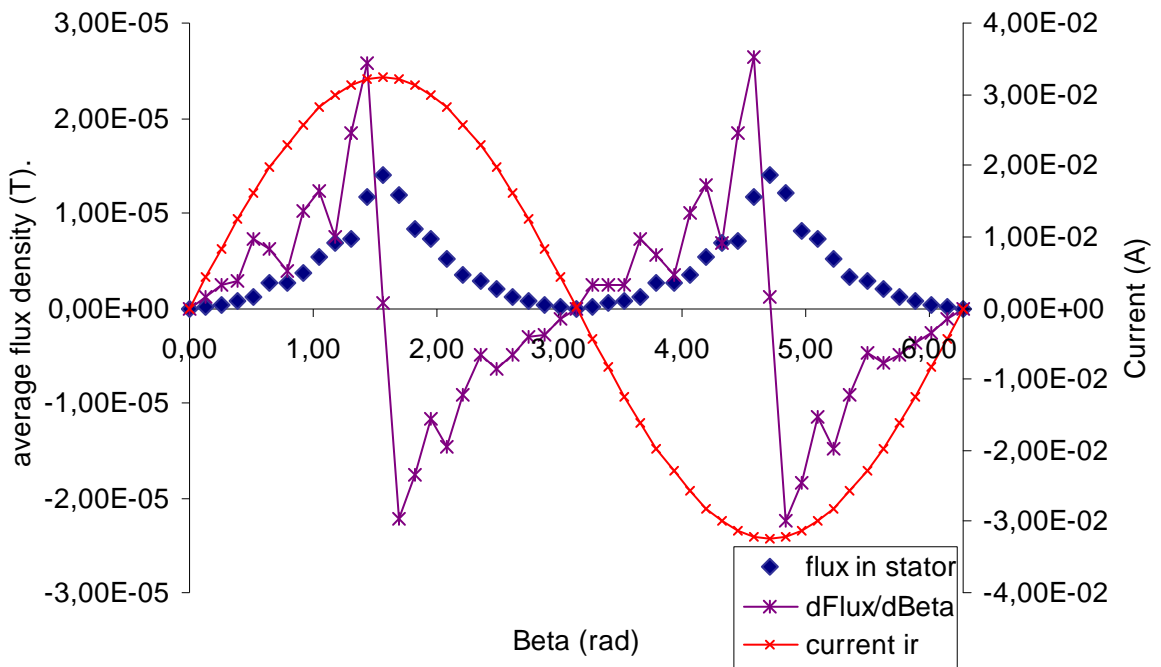


Figure 41: Simulated flux in the stator in function of the angular position of the stator

**Figure 41** presents the collection of points outputted from the set of simulations in the series “flux in stator”, as well as its derivative with respect to the angle  $\beta$ . This derivation is calculated at each point from the previous and the next point of the flux, so as to avoid introducing an artificial phase shift and an artificial agitation of the function. Data is provided in **Appendix H**.

$$\frac{d\varphi_s}{d\beta} \approx \frac{\Delta\varphi_s}{\Delta\beta} = \frac{\varphi_s(\beta + \Delta\beta) - \varphi_s(\beta - \Delta\beta)}{2.\Delta\beta} \quad \text{Equation 24}$$

Then the e.m.f. is calculated as follows:

$$e_s = -\frac{d\varphi_s}{dt} = -\frac{d\varphi_s}{d\beta} \frac{d\beta}{dt} \quad \text{Equation 25}$$

And 
$$e_s = -\omega \frac{d\varphi_s}{d\beta} \quad \text{Equation 26}$$

Since 
$$\beta = \omega t \quad \text{Equation 27}$$

And the overall sensitivity of the RC+SC is:

$$s = \frac{e_s}{I} = -\frac{\omega}{I} \frac{d\varphi_s}{d\beta} \quad \text{Equation 28}$$

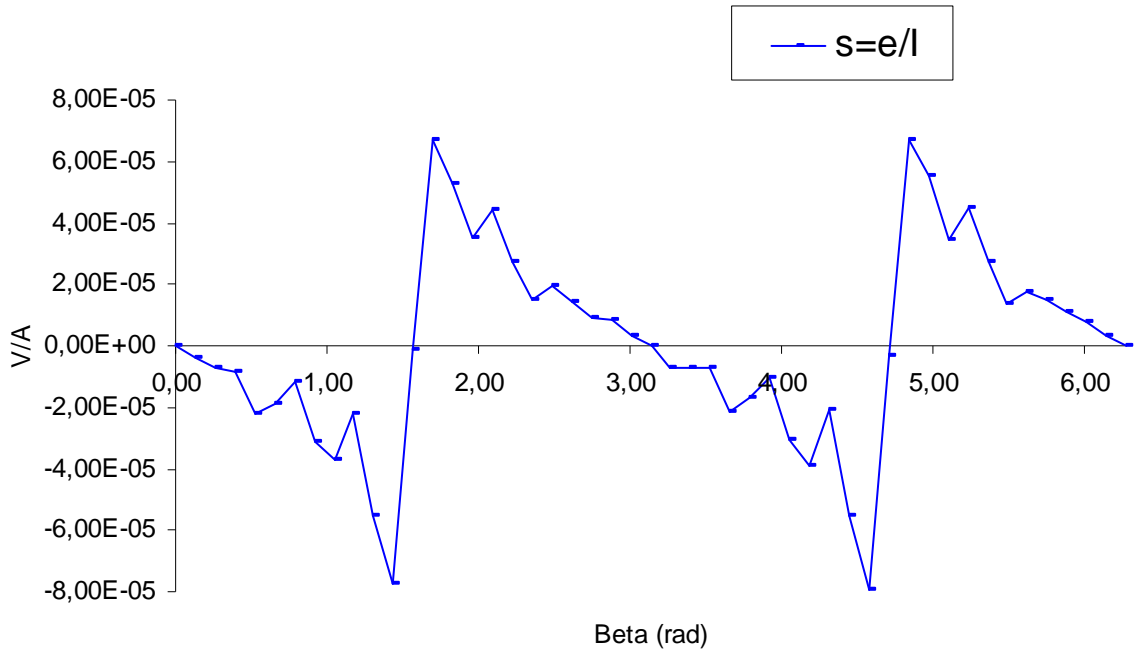


**Figure 42: Overall output sensitivity of the RC+SC sensor**

#### 4.4- Output signal

It appears clearly that the output is not the smooth function predicted by our simplistic analytical model, but it is noticeable that the magnitude is similar to this expected, and that the signal is  $2\omega$ -periodic.

Now the sensor is meant to give an image of the current in the bus bar, which is, according to our approach, a scalar. Thus output signal should eventually be reduced to a scalar as well. Two approaches are possible in order to get there:

- either keeping the  $2\omega$  fundamental frequency and filtering out the others.
- or rectifying and integrating the signal over one or a few periods.

The first one gives a sinusoid easy to deal with, whereas the second way avoids wasting power. The code and plots of the detailed signal analysis are provided in **Appendix I**.



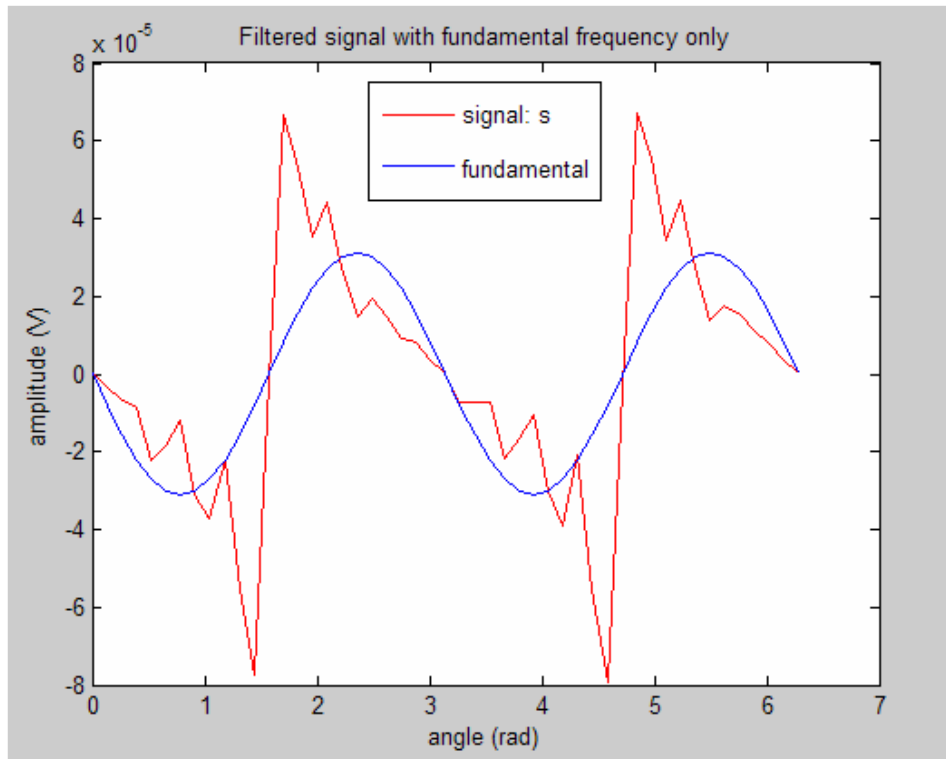


Figure 43: Output signal and filtered output signal

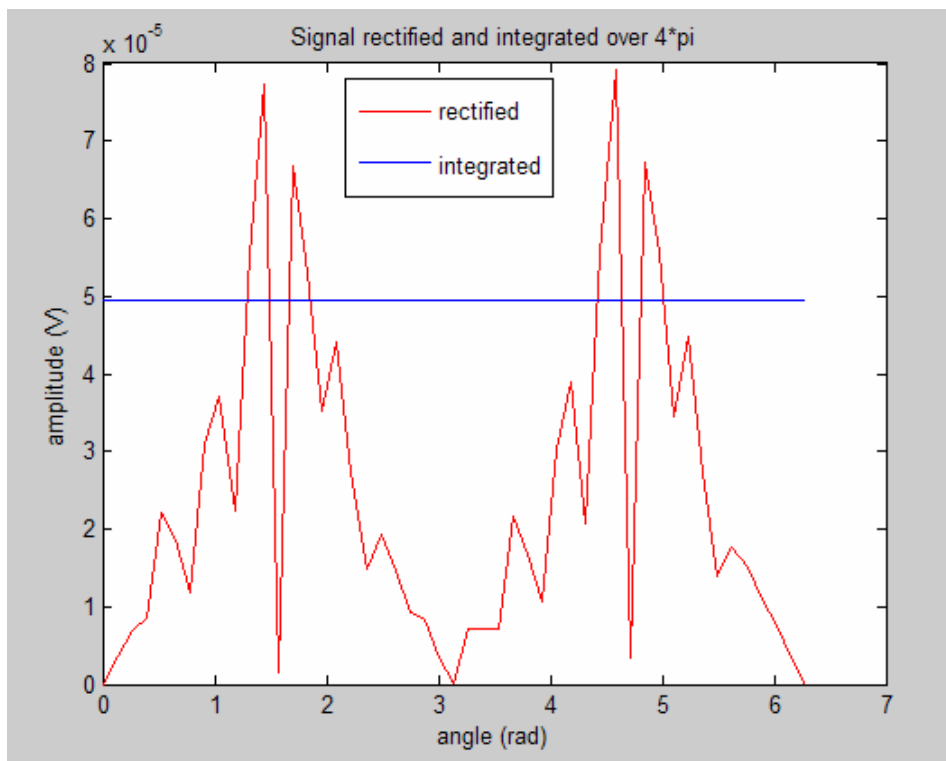


Figure 44: Output signal, rectified and integrated over  $4\pi$

#### 4.5- Mechanical considerations

The particularity of this design compared to those presented before is that it does not oscillate, it rotates at a constant speed. As it does not work based on elastic vibrations, it is much less subject to high accelerations and high stresses. The aim is to develop air bearings to avoid contacts, thus the only two types of mechanical issues left are the effect on the rotor of an abrupt variation of the velocity or orientation of the aircraft on one hand, and stresses due to centripetal acceleration on the rotor, since it spins at high speed. While the first of these issues will be strongly dependant on the design of the bearing, the second one can be estimated based solely on the geometry of the rotor. Calculations presented in **Appendix J** lead to a maximal stress of  $4.66 \times 10^5 \text{ Pa}$  or  $0.466 \text{ MPa}$  for the dimensions and angular speed presented in **Table 10**, and a silicon-based rotor. This is a fairly small value and should not create any problem.

#### 4.6- Further developments

Optimisation, linearity, resolution, one “massive” coil.

It is highly interesting to notice that Biot and Savart’s equation applied at the centre of a circular coil with diameter the average between the length and the width of the rectangular coil gives a very good approximation of the average value of the field in this rectangular coil ( $6.81 \times 10^{-5} \text{ T}$  instead of  $7.03 \times 10^{-5} \text{ T}$ , i.e. 3% error in this case). This could be included in the analytical model. But this value of  $B_r$  is not valid outside of the plane of the rotor, where it decays rapidly. An expression of this decay in space is necessary to set up a much better modelling of the overall sensitivity, since the current

equation implicitly supposes a constant value of  $B_r$  valid as far as the plane of the stator. Nonetheless, the current expression of the sensitivity (**Equation 23**) suggests an path of optimisation presented in **Appendix K** leads to the equation below:

$$e_s \propto A_r^{1/2} \quad \text{Equation 50}$$

**Equation 50** suggests that the area of the section of the conductor should be as high as possible. This can be understood as bringing down the resistance of the winding and thus raising the current, and the magnetic field  $B_r$ , then the overall sensitivity. Based on this optimisation, the rotor should be carrying or should just be one “massive” coil rather than a large number of smaller coils.

It is clear that any optimisation based on such a simplified modelling should be taken with care. The simulations conducted until this point do not represent well such a geometry, since it uses a thin conductor on the rotor. A thick conductor obstructing most of the surface intended to receive the magnetic field is not a classical situation for computation of the flux. The conductor is usually reduced to a line, so the surface delimited by the inner dimensions and this corresponding to the outer dimensions are identical. Here it becomes important to determine whether the flux should be calculated over its outer or inner-dimensions, or any intermediate dimension. In addition, in the modelling set up here, the area of the rotor’s coil is approximated to be this of the rotor itself as well as this the stator’s coil, to avoid taking magnetic leakage into account. If the rotor’s coil is thick, then  $S$  will be corresponding to its outer dimensions, so it fits inside the stator. And, since the field lines generated by the coil buckle around it, a non-

negligible difference between the effective “magnetic” surface of the rotor’s coil and the surface of the stator’s coil may imply important magnetic leakage counteracting this optimisation.

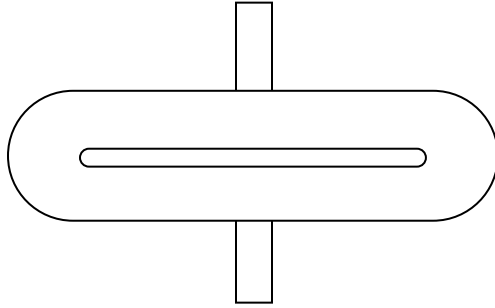


**Figure 45: The rotor based on last optimisation becomes just one massive coil**

## CHAPTER 5: CONCLUSION

When implementing analytical or simulation-based designs into an experimental process, one expects at least an offset, and quite likely some unpredicted phenomena that can be marginal or major. In this context, the lack of margins on the design parameters (especially the size) concerning the Oscillating Coil is a handicap compared to the Variable Section Coil or the Rotating Coil plus Static Coil designs. In the other hand, the OC is the simplest design, and the only one with a reliable analytical modelling than can significantly help the development of a prototype.

VSC and RC+SC have a greater potential for miniaturisation, featuring respectively 1 to 10mm and 10 to 15mm as a rough value of their main dimension, whereas the OC would rather feature 30mm under tight constraints. If the VSC is probably worth exploring despite potential issues with internal efforts due to fast deformation and large local accelerations, the most promising is probably the RC+SC design. As a matter of fact, it should bring much less mechanical issues than the two other ones, since it is not based on any deformations and actually is driven from its origin by the objective of minimizing mechanical efforts.

Despite the difficulty for modelling the behaviour of this sensor towards its design parameters like the dimensions of the rotor and the section of the conductors, this design has a high potential. As a matter of fact, it allows to consider various improvement possibilities if they proof to be necessary. Among them, a multi-layer architecture for the rotor would allow fitting more coils if the “massive” coil is not conclusive. This would also apply to the stator, where the main issue is the e.m.f. produced, which leads to

having a large number of turns, but where a multilayer architecture would allow embedding thicker coils if the output current needs to be increased.

For RC+SC, the next step may be to conduct simulation with the massive rotor. But since further modelling is heavy and uncertain, it may be preferable to start directly an experimental process to get a physical proof of concept before working on optimisation.

One thing that would still be interesting to estimate before is the power required for actuating the rotor, so as to dimension the motor. The value of the of the resisting torque would include a contribution from mechanical losses, namely friction with air if an air bearing can be used to support the rotor, and a possibly non-negligible contribution from Laplace force.

## APPENDIX A

### BENDING PIEZOACTUATORS, EXTRACT FROM A PIEZOMECHANIK™ CATALOGUE

#### 1. Introduction

##### 1.1 Applications:

When a standard piezoceramic plate is electrically activated, it shows 2 modes of motion

1. a variation in thickness: when an electrical field of proper polarity is applied, the thickness increases. This effect is used with common piezo stack actuators.
2. a planar motion: This mode always accompanies effect 1, and leads to a planar contraction of the plate under above conditions.

This effect is used in **piezoceramic bending actuators (often designated as unimorphs, bimorphs)**

When the PZT-layer is joined to a proper substrate sheet (e. g. a thin metal plate), any electrical activation of the PZT plate leads to a planar movement of the plate relatively to the

substrate and induces thereby an internal mechanical stress resulting in a bending movement of the composite structure similar to a thermo-bimetal (Fig. 1).

This works with a single PZT layer e.g. on a thin metal plate ("unimorph"), but such a system shows strong variation with temperature. A symmetric arrangement, using 2 PZT layers ("bimorph"), which are counteracting with their planar contraction/expansion, is thermally stable and shows improved displacement/force generation.

Such bending structures are used as actuators, force sensors, acoustical generators (buzzers) etc.

**PIEZOMECHANIK offers a wide range of bilayer or multi-layer PZT-benders in strip or disc geometry**

PZT benders show

- **bigger travel (up to mm) than PZT stacks for comparable operating voltages.**
  - **simple structure**
  - **flat design**
  - **wide range of operation parameters (travel, force, stiffness, resonance frequency)**
- together with the PZT specific properties
- **short reaction time**
  - **vibrationfree electro-mechanical energy conversion**
  - **no magnetic field**

and open thereby a lot of interesting design solutions e.g. in

- **positioning equipments (video/audio heads)**
- **optical tuning/chopping**
- **electrical relais**
- **valve actuation**
- **fans**
- **micropumps**

When used for high resolution positioning tasks, the philosophy of the application of PZT-benders is similar to PZT stacks:

**By combining the PZT actuator with a positioning sensor via a feedback control loop, a compensation for hysteresis, drift and varying load is obtained resulting in an ultimate positioning accuracy and stability.**

Because the PZT effect is a dual effect, **bending elements** are successfully used as vibration and force **sensors** as well as small electrical **generators**.

## 1.2. Basics: Polarization of PZT components

To understand the different philosophies of bender designs and operating modes, it is necessary to look for some details of PZT material, especially polarization.

When you are buying a simple PZT plate or disc, you will find the electrical polarity indicated on the element, and it is stated, that voltage has to be applied with correct polarity. Nevertheless, it is possible to drive such elements to some extent with counterpolarity inverting thereby the direction of motion e.g. the thickness of the plate shrinks and vice versa the plate shows a planar expansion.

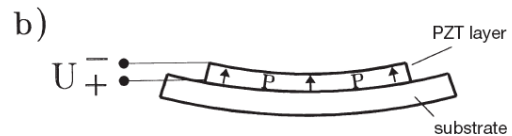
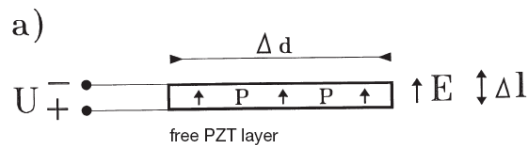
The very important point in this context is, that the acceptable **voltage range for this counteraction is much lower** than the voltage range in forward direction and this limits the travel range. The theoretical countervoltage limit is defined by the “coercitive field strength” and depends on the type of PZT ceramic. The application of too high countervoltages leads to depolarization or polarization reversal and thereby deactivate the component or change it property. Because depolarization is further supported by mechanical forces/stress and/or elevated temperatures, the acceptable countervoltages have to be held sufficiently low to avoid any risk of depoling under all conditions and **the stated limits of countervoltages have to be observed strictly**.

The coercitive field depends on the type of PZT material: “Piezoelectrically hard” PZT ceramic is more stable against depoling, but shows rather low actuating efficiency.

“Piezoelectrically soft” PZT ceramic shows good actuating efficiency in forward direction, but easily changes polarization. For several technological reasons, “soft” PZT has to be used in multilayer low voltage actuators, manufactured by co-firing technology.

This detailed explanation is necessary to show the limitations of the simplest operating mode of conventional bending elements. It makes use of this voltage reversal to produce the counteraction between the two PZT layers. Such benders are therefore made from “semi-hard” or “hard” PZT ceramics. But there are a lot of advantages, when operating modes are used, which avoid countervoltages:

- no risk of desactivation of bender even under critical driving conditions (mechanical stress, temperature)
- higher mean electrical fields and thereby higher displacement rates
- full working range for “high efficiency” benders, made of “soft” PZT or electrostrictive ceramics.





## 2. Bender types (bimorphs)

### 2.1. Serial benders

Common serial benders consist of 2 thin PZT plates, discs or strips with opposing polarizations. They are glued together by a proper adhesive, showing only 2 accessible (surface) electrodes for operation.

An application of a distinct voltage leads to a contraction of the PZT layer, where E and P are parallel and expansion of the PZT layer where E and P are antiparallel.

Serial bending elements show a bilateral movement starting from zero (middle position), when a bipolar voltage is applied. Because of the risk of depoling, the specified limits of driving voltages have to be observed strictly.

With this type of bender, the electrical capacitances of the involved PZT layers are operated serially.

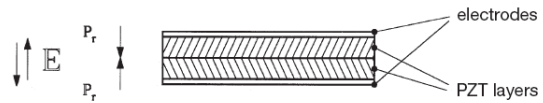


Fig. 2  
Serial bender arrangement with antiparallel polarization in PZT layers, bilateral motion for bipolar driving voltage

### 2.2. Parallel benders

For the applicator, the easiest way to distinguish a standard parallel bimorph from a serial element is, that 3 electrodes have to be connected (2 surface electrodes and 1 middle electrode).

The middle electrode can be a metal sheet as neutral fiber improving the mechanical properties of the bender or a thin metalization layer on the PZT. The electrical capacitances of the PZT layers are then connected parallel.

The standard 3-electrode design of parallel-bimorphs offers more alternatives for driving modes than the serial types.

The PZT polarization P of conventional parallel bimorphs is mostly parallel in the PZT layers as shown in fig. 3, but there exist some applications with antiparallel polarization. (e.g. see 3.3.)

The individual contacting of each PZT layer offers the choice, not only to produce a bending movement, but also a transla-

tional component: the tip of a strip bender moves axially, when the 2 PZT layers are activated for parallel motion. By superimposing axial and bending motion, you get a bi-dimensional actuator, which may be useful for some scanning microscope technologies.

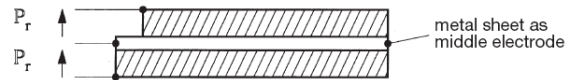


Fig. 3  
Schematic of a parallel bender structure, 2 PZT layers (e.g. parallel polarization) 3 contact electrodes

### 2.3. Multilayer benders

They behave like parallel benders (3 electrical contacts), but are built up from more than 2 PZT layers (polymorphs, multimorphs). The layers are joined together by high temperature sintering (not by an adhesive) and have therefore better

mechanical properties. From technological and performance reasons, such multilayers are made from "soft" PZT. The polarization of the PZT-layers can be easily switched and be adapted to the different driving modes.

## APPENDIX B

### ANALYTICAL CALCULATION OF SENSITIVITY WITH INFINITE WIRE HYPOTHESSIS

#### Calculation of the magnetic field $B$

The magnetising field  $H$  and then the magnetic field  $B$  can be derived as follows:

$$\oint \vec{H} \cdot d\vec{l} = \oint H \cdot dl = H \oint dl = I$$

$$2\pi \cdot r \cdot H = I$$

$$H(r) = \frac{I}{2\pi \cdot r}$$

$$B(r) = \mu_0 \cdot H(r) = \frac{\mu_0 \cdot I}{2\pi \cdot r}$$

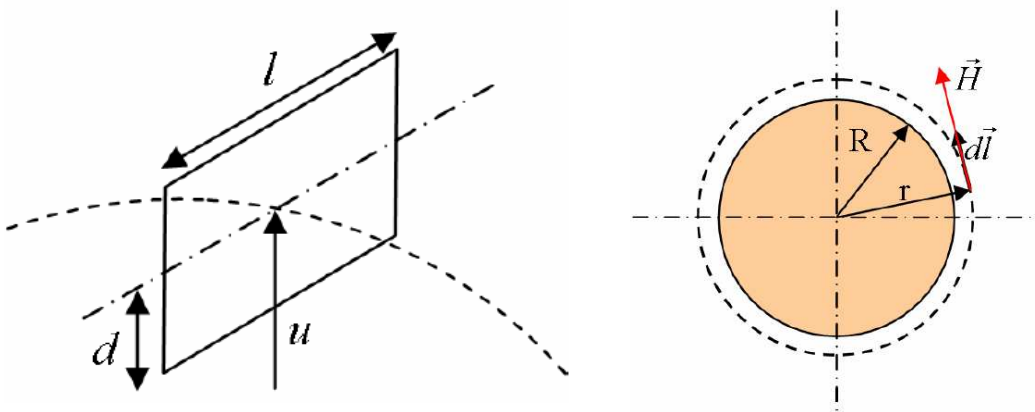


Figure 10: Infinite wire hypothesis (left) and flux in a rectangular coil (right)

## Calculation of the flux of B in the coil

**Figure 10** defines the geometry of the coil. Then the position of the coil is:

$$u(t) = u_0 + a \cdot \sin \omega t$$

$$\begin{aligned} \varphi &= \int \vec{B} \cdot d\vec{S} = \int_{u(t)-d}^{u(t)+d} B \cdot l \cdot dr = \frac{\mu_0 \cdot l}{2\pi} \cdot I \cdot \int_{u(t)-d}^{u(t)+d} \frac{dr}{r} \\ \varphi &= \frac{\mu_0 \cdot l}{2\pi} \cdot I \cdot \left( \ln \frac{u(t)+d}{u(t)-d} \right) \end{aligned}$$

And then comes

$$e = -\frac{d\varphi}{dt}$$

where  $e$  is the e.m.f. appearing on the coil. If one denotes  $s$  the sensitivity of the sensor:

$$\begin{aligned} s &= \frac{e}{I} = -\frac{1}{I} \frac{d\varphi}{dt} \\ s &= -\frac{\mu_0 \cdot l}{2\pi} \cdot \frac{4d^2 \cdot \omega \cdot \cos \omega t}{(-d + u_0 + 2d \cdot \sin \omega t)(d + u_0 + 2d \cdot \sin \omega t)} \end{aligned}$$

The denominator is developed into:

$$u_0^2 - d^2 + 4d \cdot u_0 \sin \omega t + 4d^2 \sin^2 \omega t \approx u_0^2$$

The effect on the output signal of this simplification is shown on Figure 46 in Appendix C

Then one has:

$$s = -\frac{\mu_0 \cdot l}{2\pi} \cdot \frac{2a \cdot d \cdot \omega \cdot \cos \omega t}{u_0^2}$$

If one removes the harmonic function:

$$s = -\frac{\mu_0 \cdot l}{2\pi} \cdot \frac{2a \cdot d \cdot \omega}{u_0^2}$$

### Calculation of the natural frequency $\omega$

$$\omega_k = \sqrt{\frac{E \cdot I_{yy}}{\rho \cdot S}} \left( \frac{k \cdot \pi}{L} \right)^2$$

with  $I_{yy}$  the quadratic moment of the beam in flexion

$$I_{yy} = \frac{S \cdot (2d)^2}{12}$$

For a rectangular section,

$$\omega_k = \sqrt{\frac{E \cdot (2d)^2}{12\rho}} \left( \frac{k \cdot \pi}{L} \right)^2 = 2d \sqrt{\frac{E}{12\rho}} \left( \frac{k \cdot \pi}{L} \right)^2$$

Then

$$s = -\frac{\mu_0 \cdot l}{\pi} \cdot \frac{2a \cdot d}{u_0^2} \cdot d \sqrt{\frac{E}{12\rho}} \left( \frac{k \cdot \pi}{L} \right)^2$$

Finally,

$$s = -2\mu_0 \cdot \pi \sqrt{\frac{E}{12\rho}} k^2 \frac{d^2 \cdot l}{u_0^2 \cdot L^2} a$$

## Calculation of the amplitude of oscillation $a$

The amplitude of oscillation is calculated based on the maximum acceptable value regarding stress in the support beam.

Displacement  $u_x = -z \frac{\partial w}{\partial x}$

Deformation  $\varepsilon_{xx} = -z \frac{\partial^2 w}{\partial x^2}$

Hooke's Law  $\sigma_{xx} = E \cdot \varepsilon_{xx}$

Stress on the external fibre  $\hat{\sigma}_{xx} = E \cdot d \frac{\partial^2 w}{\partial x^2}$

Deflection  $w = a \cdot \sin \frac{k \cdot \pi \cdot x}{L}$

$$|\hat{\sigma}_{xx}| = E \cdot d \cdot a \left( \frac{k \cdot \pi}{L} \right)^2 \sin \frac{k \cdot \pi \cdot x}{L}$$

$$|\hat{\sigma}_{xx \max}| = E \cdot d \cdot a \left( \frac{k \cdot \pi}{L} \right)^2$$

$$|\hat{\sigma}_{xx \max}| \leq \sigma_{crit}$$

$$\Rightarrow a_{\max} = \frac{\sigma_{crit} \cdot L^2}{E \cdot d \cdot k^2 \cdot \pi^2}$$

### Calculation of the sensitivity s

The maximum sensitivity, based on the maximum acceptable stress in the beam, becomes:

$$\max_{\sigma}(s) = -2\mu_0 \cdot \pi \sqrt{\frac{E}{12\rho}} k^2 \frac{d^2 \cdot l}{u_0^2 \cdot L^2} \frac{\sigma_{crit} \cdot L^2}{E \cdot d \cdot k^2 \cdot \pi^2}$$

$$\max_{\sigma}(s) = -\frac{\mu_0}{\pi} \sqrt{\frac{1}{3\rho \cdot E}} \frac{d \cdot l}{u_0^2} \sigma_{crit}$$

If  $l = \alpha \cdot d$ , and taking into account the number of coils  $N$

$$\max_{\sigma}(s) = -\alpha \cdot \frac{\mu_0}{\pi} \sqrt{\frac{1}{3\rho \cdot E}} \frac{d^2}{u_0^2} \sigma_{crit} \cdot N$$

To derive the main design parameter, the equation is flipped and  $s_0$ , the desired sensitivity, is introduced:

$$d^2 = \frac{s_0 \cdot u_0^2 \cdot \pi \sqrt{3\rho \cdot E}}{\alpha \cdot \mu_0 \cdot \sigma_{crit} \cdot N}$$

$$d = u_0 \sqrt{\frac{s_0 \cdot \pi \sqrt{3\rho \cdot E}}{\alpha \cdot \mu_0 \cdot \sigma_{crit} \cdot N}}$$

Parameters (SI)	$E$ (Mpa)	$\rho$ (kg.m <sup>-3</sup> )	$s_0$ (V.A <sup>-1</sup> )	$\alpha$	$\sigma_{crit}$ (MPa)	$u_0$ (m)	$N$
	2.00E+11	2.40E+03	5.00E-05	4	4.00E+08	3.00E-03	100
<b>d(m)</b>	<b>5.17E-04</b>						

In red are the design parameters, in black the calculated values. Two possibilities are presented below:

$2d$	$l$	$L/l$	$L$	$a$	$u_0$ (m)	$\omega$
1.03E-03	2.06E-03	5	1.03E-02	4.19E-05	3.00E-03	2.52E+05

$2d$	$l$	$L/l$	$L$	$a$	$u_0$ (m)	$\omega$
1.03E-03	2.06E-03	10	2.07E-02	1.67E-04	3.00E-03	6.29E+04

## APPENDIX C

### NUMERICAL CALCULATION OF SENSITIVITY FOR OC FOR VALIDATION OF SIMPLIFICATIONS

```
%%%%%%%%%%%%%%%%%%%%%%%%%%%%%%%%%%%%%%%%%%%%%%%%%%%%%%%%%%%%%%%%%%%%%%%%%%%%%%  
%%%%%%%%%%%%%%%%%%%%%%%%%%%%%%%%%%%%%%%%%%%%%%%%%%%%%%%%%%%%%%%%%%%%%%%%%%%%%% Sensitivity Calculation %%%%%%%%%%%%%%%%%%%%%%%%%%%%%%%%%%%%%%%%%%%%%%%%%%%%%%%%%%%%%%%%%%%%%%%%%%%%%%%  
%%%%%%%%%%%%%%%%%%%%%%%%%%%%%%%%%%%%%%%%%%%%%%%%%%%%%%%%%%%%%%%%%%%%%%%%%%%%%%
```

```
clear all  
close all
```

All the calculations presented here are based on the analytic expression of B derived from the infinite wire hypothesis. The mechanical support is a beam in resonance in flexion.

The aim of this code is to show the validity of the simplification made in the numerator of the analytical expression of the sensitivity.

---

```
% In the variable s0, the sensitivity is calculated with a denominator  
simplified into u02  
% In the variable s1, one multiplies s0 by a harmonic function "carrier"  
that describes the oscillation of the coil.  
% In the variable s2, it is calculated with the full expression of the  
denominator.  
% In the variable s3, one multiplies s2 by a harmonic function "carrier"  
that describes the oscillation of the coil.  
  
w = 60000; % frequency of oscillation of the beam rad/s  
k = 214 ; % =16384 number of time samples  
t = linspace(0,8*pi/w,k); % sample of time: 4 periods  
  
d = 0.00025; % half-thickness of the beam/coil  
l = 0.00125; % width of the beam/coil  
uo = 0.003; % distance at rest between centre conductor  
and centre coil  
  
muo = 4*pi*10-7; % magnetic permeability of vacuum  
E = 1.6e11; % Young modulus of the beam  
sigmacrit= 7e9; % yield point of the beam  
rho = 2.4e3; % density  
  
for i=1:k  
s0(i) = -(muo/pi) * ((3*rho*E)(-0.5)) * (d*l*sigmacrit)/(uo2);  
s1(i) = s0(i)*cos(w*(t(i)));  
s2(i) = -(muo/pi) * ((3*rho*E)(-0.5)) * (d*l*sigmacrit)  
/(((d+uo+2*d*sin(w*t(i)))*(d+uo+2*d*sin(w*t(i))));  
s3(i) = s2(i)*cos(w*(t(i)));  
end
```



```

%%%%%%%%%%%%%%%%%%%%%%%%%%%%%%%%%%%%%%%%%%%%%%%%%%%%%%%%%%%%%%%%%%%%%%%%
%%%%%%%%%%%%%%%%%%%%%%%%%%%%%%%%%%%%%%%%%%%%%%%%%%%%%%%%%%%%%%%%%%%%%%%% Fourier transform of s3 %%%%%%%%%%%%%%%%%%%%%%%%%%%%%%%%%%%%%%%%%%%%%%%%%%%%%%%%%%%%%%%%%%%%%%%%%
%%%%%%%%%%%%%%%%%%%%%%%%%%%%%%%%%%%%%%%%%%%%%%%%%%%%%%%%%%%%%%%%%%%%%%%%

K=k; % sampling for fft
S3= fft(s3,K);
P=S3.*conj(S3)/K; % The power spectrum

f =(1./(t(2)-t(1)))*(0:K/2)/K;

%%%%%%%%%%%%%%%%%%%%%%%%%%%%%%%%%%%%%%%%%%%%%%%%%%%%%%%%%%%%%%%%%%%%%%%%
%%%%%%%%%%%%%%%%%%%%%%%%%%%%%%%%%%%%%%%%%%%%%%%%%%%%%%%%%%%%%%%%%%%%%%%% Curves plotting %%%%%%%%%%%%%%%%%%%%%%%%%%%%%%%%%%%%%%%%%%%%%%%%%%%%%%%%%%%%%%%%%%%%%%%%%
%%%%%%%%%%%%%%%%%%%%%%%%%%%%%%%%%%%%%%%%%%%%%%%%%%%%%%%%%%%%%%%%%%%%%%%%

%_____Figure 1_____

% first figure has 4 curves, compared all together then 2 by 2, for
details

figure1 = figure('PaperPosition',[0.6345 6.345 20.3
15.23],'PaperSize',[20.98 29.68]);

%% Create axes
axes1 = axes('OuterPosition',[0 0.4985 0.4823 0.5015],'Parent',figure1);
title(axes1,'sensibilité du capteur'); %sensitivity of the sensor
xlabel(axes1,'time (s)');
hold(axes1,'all');

subplot(221)
plot1 = plot(t,s0,t,s1,t,s2,t,s3);
title('sensibilité du capteur') %sensitivity of the sensor
xlabel('time (s)')
legend1 = legend({'s0','s1','s2','s3'],'Position',[0.3661 0.745 0.1286
0.1551]);

subplot(222)
plot2= plot(t,s1,t,s3);
title('effet du dénominateur') %effect of denominator
legend2 = legend({'s1 : simplifie','s3 : complet'],'Position',[0.8087
0.77 0.13 0.1551]);

subplot(223)
plot2= plot(t,s0,t,s2);
title('effet du dénominateur') %effect of denominator
legend3 = legend({'s0 : simplifie','s2 : complet'],'Position',[0.3766
0.3055 0.13 0.1551]);

subplot(224)
plot2= plot(t,s2,t,s3);
title('multiplication par cos')
legend4 = legend({'s2 : avant','s3 : apres'],'Position',[0.8073 0.3055
0.1286 0.1551]);

```

% \_\_\_\_\_ Figure 2 \_\_\_\_\_

```
figure
% first graph, power spectrum of s3
subplot(221)
plot21=plot(f(1:64+1),(P(1:64+1)));
title('Zoom Power spectrum of s3')
xlabel('frequency (Hz)')
ylabel('P = fft(s2)*conj(fft(s3))')

% second graph, power spectrum of s3
subplot(222)
plot22=plot(f(1:K/2),log10(P(1:K/2)));
title('log 10 of Power spectrum of s3')
xlabel('frequency (Hz)')
ylabel('log10(P)')

% third graph, power spectrum of s3
subplot(223)
plot23=plot(f(1:64+1),log10(P(1:64+1)));
title('Zoom log 10 of Power spectrum of s3')
xlabel('frequency (Hz)')
ylabel('log10(P)')

% fourth graph, to let harmonics numbers appear
f1 =(1/9549)*(1./(t(2)-t(1)))*(0:K/256)/K-1;
subplot(224)
plot24=plot(f1(1:64+1),log10(P(1:64+1)));
title('Zoom on Harmonics in s3')
xlabel('numero')
```

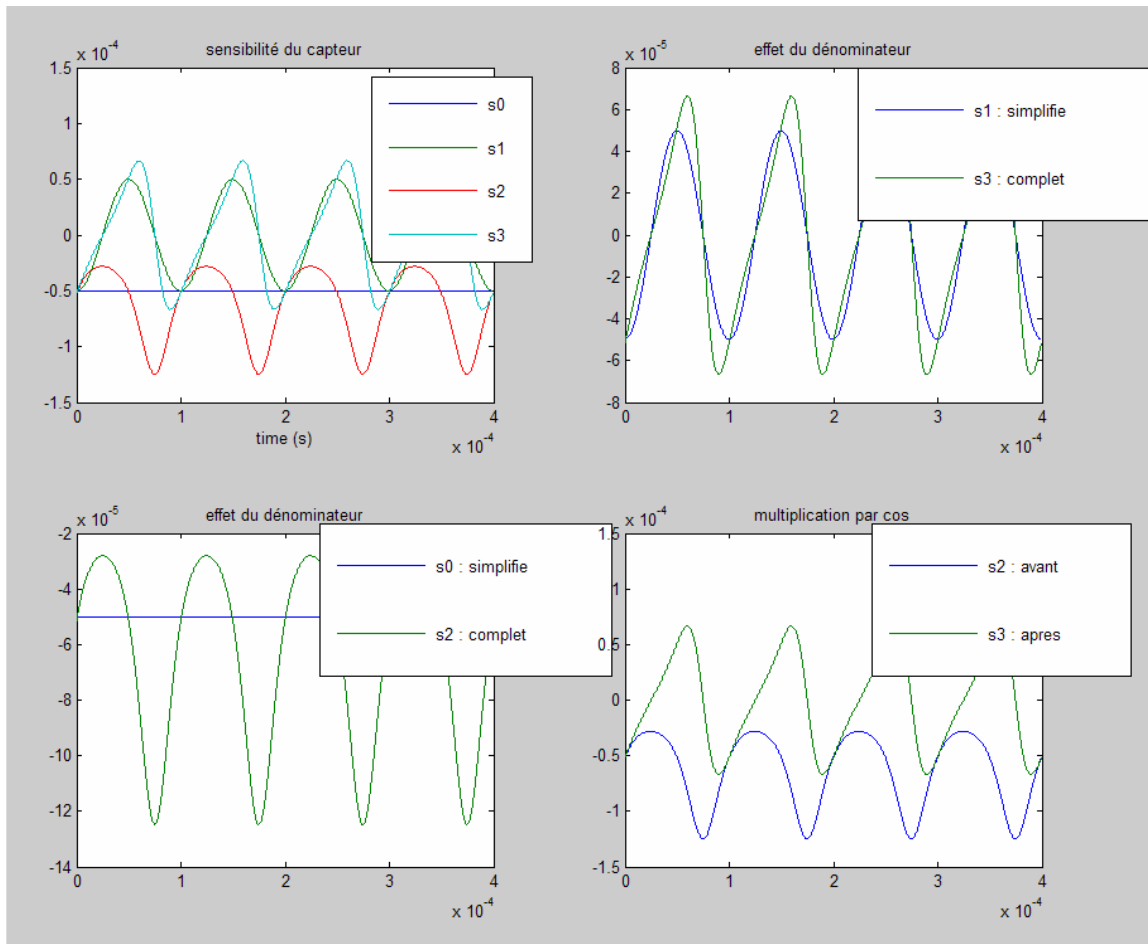


**Figure 46: Effect of the simplification of the denominator on the actual output signal**

```

% Recall:
%
% s0: sensitivity with simplified denominator  $u_0^2$ 
% s1: s0 multiplied by a cosine, "carrier" due to the oscillation of the
coil
% s2: sensitivity with complete denominator
% s3: s2 multiplied by a cosine, "carrier" due to the oscillation of the
coil. This is the ACTUAL output signal

```

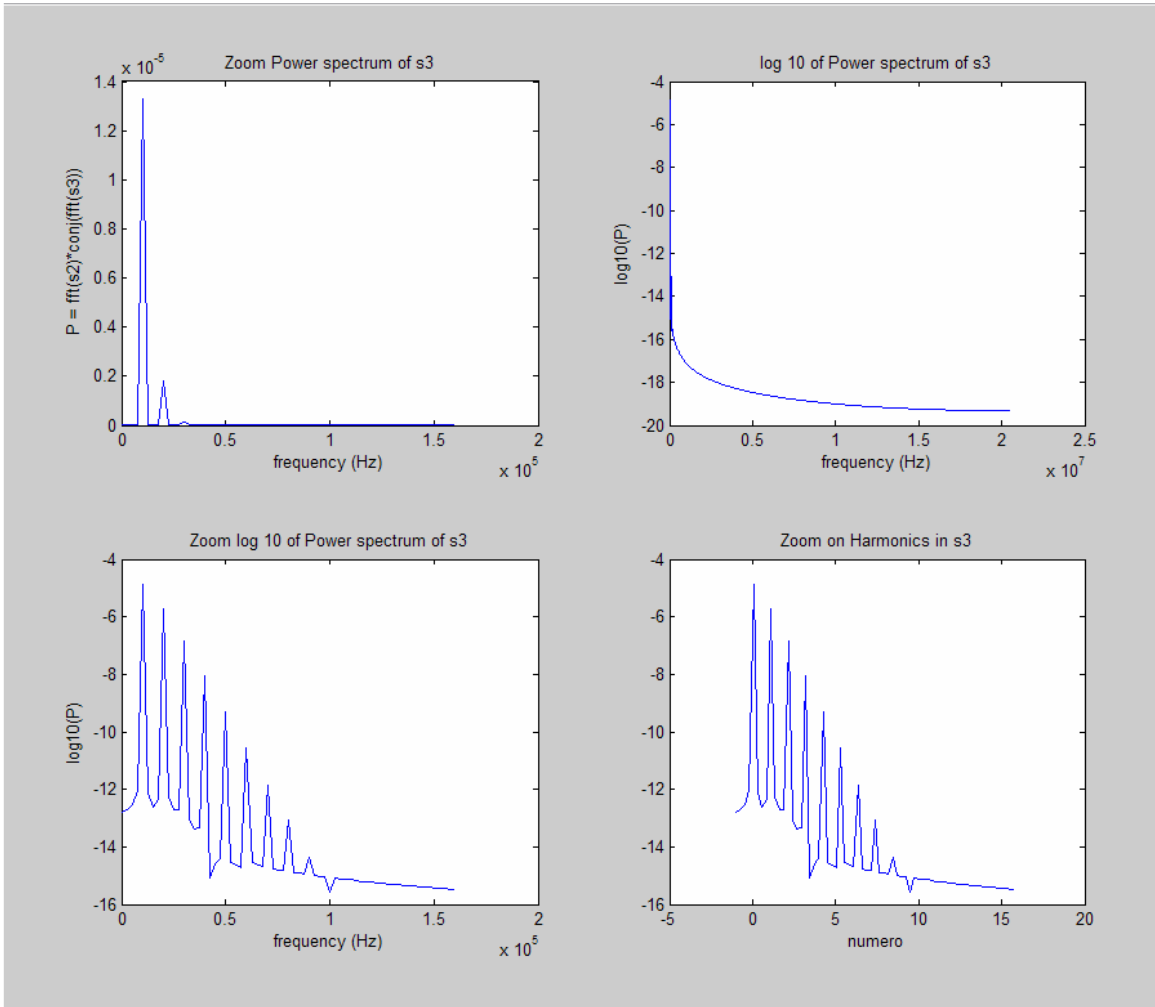


**Figure 47: Frequency content of the output signal**

## APPENDIX D

### NUMERICAL CALCULATION OF SENSITIVITY FOR OC AND LINEARISED B

```

%%%%%%%%%%%%%%%%%%%%%%%%%%%%%%%%%%%%%%%%%%%%%%%%%%%%%%%%%%%%%%%%%%%%%%%%
%%%%%%%%%%%%%%%%%%%%%%%%%%%%%%%%%%%%%%%%%%%%%%%%%%%%%%%%%%%%%%%%%%%%%%%% OC, B simulated linearised %%%%%%%%%
%%%%%%%%%%%%%%%%%%%%%%%%%%%%%%%%%%%%%%%%%%%%%%%%%%%%%%%%%%%%%%%%%%%%%%%%

close all
clear all

%
%-----
% definition of B= bo + b1 * y          % linearised magnetic flux

b1 = -1.8887e-3;
bo = 3.1280e-5;

%
%-----

w = 62900;          % natural frequency
kt = 2^10;          % number of time samples
t = linspace(0,4*pi/w,kt); % discretisation of time interval
ky = 40;            % nb samples on y
d = 517e-6;         % half thickness of beam/coil
eb = 3e-3;          % thickness of bus bar
a = 167e-6;         % vibration amplitude
uo = d+a+eb/2+100e-6; % initial distance coil/bus bar
yo = uo + a*cos(w*t); % position centre coil along time
phi = zeros(1,kt); % initialisation flux variable
l = 4*d;            % with of beam/coil
N = 100;            % number de coils

%
%-----

for i = 1:kt
    for m = 1:ky
        y(m) = yo(i) - d + m*2*d/ky;
        B(m) = bo + b1*y(m);
    end
    Q = B*(y(2)-y(1))*l*N;
    phi(i)= phi(i)+sum(Q);
end

subplot(211)
plot(t,phi)
title('phi(t)');
dphi = diff(phi)/(t(2)-t(1));
subplot(212)
plot(t(1:kt-1),dphi)
title ('d phi / d t');

```

```

%_____ Fourier transform of s3 _____

K=kt; % sampling for fft
DPHI= fft(dphi,K);
P=DPHI.*conj(DPHI)/K; % The power spectrum
f =(1./(t(2)-t(1)))*(0:K/2)/K; % Frequencies

figure
subplot(211)
plot(f(1:K/2+1),P(1:K/2+1))
title('power spectrum of the signal')
xlabel('frequency (rd/s)')
subplot(212)
plot(f(1:K/16+1),log10(P(1:K/16+1)))
title('zoom on the log10 of the power spectrum')
xlabel('frequency (rd/s)')

```

## APPENDIX E

### NUMERICAL CALCULATION OF SENSITIVITY FOR VSC AND OPTIMISATION

```

%%%%%%%%%%%%%%%%%%%%%%%%%%%%%%%%%%%%%%%%%%%%%%%%%%%%%%%%%%%%%%%%%%%%%%%%
%%%%%%%%%%%%%%%%%%%%%%%%%%%%%%%%%%%%%%%%%%%%%%%%%%%%%%%%%%%%%%%%%%%%%%%% Optimisation of the coil %%%%%%%%%
%%%%%%%%%%%%%%%%%%%%%%%%%%%%%%%%%%%%%%%%%%%%%%%%%%%%%%%%%%%%%%%%%%%%%%%%

% This program aims to optimise the flux variation in the variable
% section coil as a function of its initial configuration (angle teta).
% As a first approximation, one takes as a magnetic field B this of an
% infinite wire for the direction y, and constant for the direction x

% Here the coil is a 6 bars system. It is implicitly fastened at its
% inferior side c3, and actuated at its side summit s2 and/or s4.

% Let us recall that the hexagonal coil can be seen as the addition of a
% rectangle and two half-diamonds (one on each end). The quarters of
% diamonds are also rectangle triangles.

% The design parameters are h (side of the losange), td (deformation
% rate), and lo (the length of the superior side).

close all
clear all

%
muo = pi*4e-7; % magnetic permeability of vacuum
eb = 3e-3; % thickness of the bus bar
kt = 100; % number of time increments
ky = 20; % number of increments on y
kx = 20; % number of increments on x
kteta= 100; % number of increments on teta (initial
% angles tested)
w = 1500000; % natural frequency
t = linspace(0,4*pi/w,kt); % discretisation of the time interval
teta0= 5*pi/180; % initial angle at end of 1/4 diamond
h = 0.05e-3; % hypotenuse of 1/4 diamond
eo = h*cos(teta0); % initial length of 1/4 diamond
lo = 0.5e-3; % length of rectangle
td = 0.002; % deformation rate
b = td*(lo+2*eo); % amplitude of displacement at actuating
% point
e = zeros(1,kt); % length of 1/4 diamond
d = zeros(1,kt); % height of 1/4 diamond
phil = zeros(kteta,kt); % flux in the diamond
phir = zeros(kteta,kt); % flux in the rectangle
phi = zeros(kteta,kt); % total flux in the N coils
dmax = zeros(1,kteta); % height of 1/4 diamond in oscillation
teta = linspace (5*pi/180,pi/2,kteta);%angle at the end of 1/4 diamond
% before oscillation
N = 12; % number of coils

%

```

```

for p = 1:kteta

    eo = h * cos (teta(p));
    dmax(p) = (h^2-(eo-b)^2)^0.5;
    uo = (eb/2+dmax(p))*1.2; % initial distance between
                             % centers coil/bus bar

    if eo+b<h
        if eo-b >0

            for i=1:kt
                e(i) = eo + b*sin(w*t(i));
                d(i) = (h^2-(e(i))^2)^0.5;
                Dy = 2*d(i)./ky; % delta

            for m=1:ky
                y(m) = eb/2 + m*2*d(i)/ky;
                B(m) = muo*1./(2*pi*y(m));
                ex = e(i)./d(i).*y(m).*(y(m)<d(i))
+ 2*e(i)*(1-y(m)./d(i)).*(y(m)>d(i));
                phil(p,i) = phil(p,i) + 2.*ex.*B(m).*Dy;
            end
            phir(p,i) = lo*sum(B)*Dy;
            phi(p,i) = N * (phir(p,i)+phil(p,i));
        end

        else q = teta(p)*180/pi;
            while q > 360
                q = q - 360;
            end
            q
            break
        end
    end
end

subplot(211)
plot(t,phi(kteta/2,1:kt))
title 'phi (t) pour teta = 45°'
xlabel '* pi radians'

Dt=(t(2)-t(1));
for r = 1:p-1
    for i = 2:kt;
        dphi(r,i) = (phi(r,i) - phi(r,i-1)) /Dt;
        dphir(r,i) = (phir(r,i) - phir(r,i-1)) /Dt;
        dphil(r,i) = (phil(r,i) - phil(r,i-1)) /Dt;
    end
end
subplot(212)
plot(t,dphi(kteta/2,1:kt))
title 'd phi / d t pour teta = 45°'

figure
subplot(211)

```



```

plot(t,dphir(kteta/2,1:kt),t,dphil(kteta/2,1:kt))
title 'd phi / d t séparément dans le rectangle et dans le losange'
legend('rectangle','losange')
subplot(212)
plot(t,dphi(kteta/2,1:kt))
title 'd phi / d t dans la spire complète'

figure
M=max(transpose(dphi));
m=min(e);
%subplot(211)
plot(teta(1:p-1).*180./pi,M)
title 'max sur t de (d phi / d t), en fonction de teta'
xlabel 'teta en degrés'
% subplot(212)
% plot(teta(1:p-1).*180./pi,m)
% title 'min sur t de (e), en fonction de teta'
% xlabel 'teta en degrés'
%
```

## APPENDIX F

### NUMERICAL CALCULATION OF SENSITIVITY FOR VSC AND B LINEARISED

```

%%%%%%%%%%%%%%%%%%%%%%%%%%%%%%%%%%%%%%%%%%%%%%%%%%%%%%%%%%%%%%%%%%%%%%%%
%%%%%%%%%%%%%%%%%%%%%%%%%%%%%%%%%%%%%%%%%%%%%%%%%%%%%%%%%%%%%%%%%%%%%%%% VCS B simulated linearised %%%%%%%%%
%%%%%%%%%%%%%%%%%%%%%%%%%%%%%%%%%%%%%%%%%%%%%%%%%%%%%%%%%%%%%%%%%%%%%%%%

% Here, the coil is hexagonal. It is implicitly fastened at its superior
% side c3, and actuated at its lateral summit s2 and/or s4. For example
% it could be considered that the piezo is horizontal and joins s2 to s4

% It appears that w should not be too high, since it would generate very
% high accelerations. As much as possible, large deformations are
% preferable on the dynamics point of view.

close all
clear all

% définition of B = bo + b1 * y
b1 = -1.8887e-3;
bo = 3.1280e-5;
%
eb = 3e-3;
kt = 100;
ky = 40;
w = 10000;
t = linspace(0,4*pi/w,kt);
teta0= 45*pi/180;
h = 1e-3;
eo = h*cos(teta0);
lo = 5e-3;
td = 0.02;
b = td*(lo+2*eo);
e = zeros(1,kt);
d = zeros(1,kt);
phil = zeros(1,kt);
phi = zeros(1,kt);
phir = zeros(1,kt);
N = 140;
%
for i=1:kt
    e(i) = eo + b*sin(w*t(i));
    d(i) = (h^2-(e(i))^2)^0.5;
    Dy = 2*d(i)./ky; % delta y

    for m=1:ky
        ys(m)= m^2*d(i)/ky;
        y(m) = eb/2 +ys(m);
        B(m) = bo + b1*y(m);
        if ys(m)<d(i)
            ex = e(i)./d(i).*ys(m);
        elseif ys(m)>d(i)

```

```

        ex      = e(i)*(2-ys(m)./d(i));
    else
        ex      = e(i);
    end
    phil(i) = phil(i) + 2.*ex.*B(m).*Dy;

end
    phir(i) = lo*sum(B)*Dy;
    phi(i)  = N*(phir(i)+phil(i));
end

% _____ Plotting phi et dphi _____

subplot(211)
plot(t,phi)
title 'phi(t)'
xlabel 'temps (s)'

Dt=(t(1)-t(2));
dphi=diff(phi)/Dt;
subplot(212)
plot(t(1:kt-1),dphi(1:kt-1))
title 'd phi / d t'
xlabel 'temps (s)'

% _____ Plotting d et e _____

figure
plot(t,d,t,e)
legend ('d','e')
xlabel 'temps (s)'

% _____ Plotting velocity and max acceleration _____

vit = diff(2*d)/Dt;
acc = (diff(vit)/Dt)/9.81;

figure
subplot(211)
plot(t(1:kt-1),vit,t(1:kt-2),acc)
title 'dynamique maximum (barre supérieure)'
xlabel 'temps (s)'
legend ('vitesse (m/s)', 'accél. (Nb de g)')

tetal(1:kt)=teta0*180/pi;
subplot(212)
teta=180/pi*acos(e/h);
plot(t,teta,t,tetal)
legend('teta','teta0')
xlabel 'temps (s)'

```

## APPENDIX G

### ANALYTICAL CALCULATION OF THE SENSITIVITY OF THE RC+SC

This notice of calculation starts from **Equation 20** for the current  $i_r$ , derived in section **4.2.1**, and **Equations 21** for  $B_r$  and **22** for  $e_s$  stated in section **4.2.2**.

$$i_r = \frac{\omega \cdot B \cdot S \cdot n_r}{R_r} \sin \beta(t) \quad \text{Equation 20}$$

$$B_r = \gamma \cdot i_r \cdot n_r \quad \text{Equation 21}$$

$$e_s = -\frac{d\varphi_s}{dt} = -\frac{d}{dt} \iint_S \overset{\rho}{B}_r \bullet \overset{\rho}{dS}_s \quad \text{Equation 22}$$

Substituting **Equation 21** into **Equation 22**, the latter becomes:

$$e_s = -\frac{d}{dt} \gamma \cdot i_r \cdot n_r \cdot S \cdot \cos(\overset{\rho}{B}_r, \overset{\rho}{S}_s)(t) \quad \text{Equation 29}$$

With  $(\overset{\rho}{B}_r, \overset{\rho}{S}_s)(t) = \frac{\pi}{2} + \beta(t) = \frac{\pi}{2} + \omega \cdot t$  **Equation 30**

Then  $e_s = -\gamma \cdot n_r \cdot S \frac{d}{dt} \left( i_r \cdot \cos \left( \frac{\pi}{2} + \beta(t) \right) \right)$  **Equation 31**

The shift gives:

$$e_s = \gamma \cdot n_r \cdot S \frac{d}{dt} (i_r(t) \cdot \sin \beta(t)) \quad \text{Equation 32}$$

$$e_s = \gamma \cdot n_r \cdot S \left( \omega \cos \beta(t) \cdot i_r(t) + \sin \beta(t) \frac{d}{dt} i_r(t) \right) \quad \text{Equation 33}$$

And

$$\frac{d i_r(t)}{dt} = \frac{\omega^2 \cdot B \cdot S \cdot n_r}{R_r} \cos \beta(t) \quad \text{Equation 34}$$

From **Equation 20**. Then plugging **Equations 20** and **29** into **28**:

$$e_s = \gamma \cdot n_r \cdot S \left( \frac{\omega^2 \cdot B \cdot S \cdot n_r}{R_r} \sin \beta(t) \cos \beta(t) + \frac{\omega^2 \cdot B \cdot S \cdot n_r}{R_r} \sin \beta(t) \cos \beta(t) \right) \quad \text{Equation 35}$$

$$e_s = 2 \frac{\gamma \cdot \omega^2 \cdot B \cdot S^2 \cdot n_r^2 \cdot n_s}{R_r} \sin \beta(t) \cos \beta(t) \quad \text{Equation 36}$$

Introducing the numbers  $n_s$  of coils in the stator and using a trigonometric identity finally turns it into **Equation 23** presented in section **4.2.2**.

$$e_s = \frac{\gamma \cdot \omega^2 \cdot B \cdot S^2 \cdot n_r^2 \cdot n_s}{R_r} \sin(2\beta(t)) \quad \text{Equation 23}$$

APPENDIX H

Table 13: Data collection for the flux in the stator

$\beta$	rad	$i_r$	avg flux density	flux in stator	dFlux/dBeta	$s=e_s/l$
0,0	0,00	0,00E+00	0,00E+00	0,00E+00	0,00E+00	0,00E+00
7,5	0,13	4,24E-03	3,45E-07	6,90E-08	1,23E-06	-3,69E-06
15,0	0,26	8,41E-03	1,61E-06	3,22E-07	2,32E-06	-6,96E-06
22,5	0,39	1,24E-02	3,38E-06	6,76E-07	2,81E-06	-8,43E-06
30,0	0,52	1,63E-02	5,29E-06	1,06E-06	7,35E-06	-2,20E-05
37,5	0,65	1,98E-02	1,30E-05	2,60E-06	6,20E-06	-1,86E-05
45,0	0,79	2,30E-02	1,34E-05	2,68E-06	3,97E-06	-1,19E-05
52,5	0,92	2,58E-02	1,82E-05	3,64E-06	1,03E-05	-3,09E-05
60,0	1,05	2,81E-02	2,69E-05	5,38E-06	1,24E-05	-3,71E-05
67,5	1,18	3,00E-02	3,44E-05	6,88E-06	7,41E-06	-2,22E-05
75,0	1,31	3,14E-02	3,66E-05	7,32E-06	1,84E-05	-5,52E-05
82,5	1,44	3,22E-02	5,85E-05	1,17E-05	2,57E-05	-7,72E-05
90,0	1,57	3,25E-02	7,03E-05	1,41E-05	5,35E-07	-1,60E-06
97,5	1,70	3,22E-02	5,92E-05	1,18E-05	-2,22E-05	6,67E-05
105,0	1,83	3,14E-02	4,12E-05	8,24E-06	-1,76E-05	5,29E-05
112,5	1,96	3,00E-02	3,61E-05	7,22E-06	-1,18E-05	3,53E-05
120,0	2,09	2,81E-02	2,58E-05	5,16E-06	-1,47E-05	4,40E-05
127,5	2,23	2,58E-02	1,69E-05	3,38E-06	-9,09E-06	2,73E-05
135,0	2,36	2,30E-02	1,39E-05	2,78E-06	-4,97E-06	1,49E-05
142,5	2,49	1,98E-02	1,04E-05	2,08E-06	-6,40E-06	1,92E-05
150,0	2,62	1,63E-02	5,52E-06	1,10E-06	-4,84E-06	1,45E-05
157,5	2,75	1,24E-02	4,06E-06	8,12E-07	-3,05E-06	9,14E-06
165,0	2,88	8,41E-03	1,53E-06	3,06E-07	-2,75E-06	8,26E-06
172,5	3,01	4,24E-03	4,56E-07	9,12E-08	-1,17E-06	3,51E-06
180,0	3,14	3,98E-18	0,00E+00	0,00E+00	-7,64E-08	2,29E-07
187,5	3,27	-4,24E-03	3,56E-07	7,12E-08	2,36E-06	-7,08E-06
195,0	3,40	-8,41E-03	3,09E-06	6,18E-07	2,35E-06	-7,05E-06
202,5	3,53	-1,24E-02	3,43E-06	6,86E-07	2,38E-06	-7,15E-06
210,0	3,67	-1,63E-02	6,21E-06	1,24E-06	7,23E-06	-2,17E-05
217,5	3,80	-1,98E-02	1,29E-05	2,58E-06	5,57E-06	-1,67E-05
225,0	3,93	-2,30E-02	1,35E-05	2,70E-06	3,51E-06	-1,05E-05
232,5	4,06	-2,58E-02	1,75E-05	3,50E-06	1,01E-05	-3,03E-05

240,0	4,19	-2,81E-02	2,67E-05	5,34E-06	1,30E-05	-3,90E-05
247,5	4,32	-3,00E-02	3,45E-05	6,90E-06	6,88E-06	-2,06E-05
255,0	4,45	-3,14E-02	3,57E-05	7,14E-06	1,85E-05	-5,55E-05
262,5	4,58	-3,22E-02	5,87E-05	1,17E-05	2,64E-05	-7,93E-05
270,0	4,71	-3,25E-02	7,03E-05	1,41E-05	1,15E-06	-3,44E-06
277,5	4,84	-3,22E-02	6,02E-05	1,20E-05	-2,24E-05	6,72E-05
285,0	4,97	-3,14E-02	4,10E-05	8,20E-06	-1,85E-05	5,55E-05
292,5	5,11	-3,00E-02	3,60E-05	7,20E-06	-1,15E-05	3,46E-05
300,0	5,24	-2,81E-02	2,59E-05	5,18E-06	-1,49E-05	4,47E-05
307,5	5,37	-2,58E-02	1,65E-05	3,30E-06	-9,09E-06	2,73E-05
315,0	5,50	-2,30E-02	1,40E-05	2,80E-06	-4,66E-06	1,40E-05
322,5	5,63	-1,98E-02	1,04E-05	2,08E-06	-5,88E-06	1,76E-05
330,0	5,76	-1,63E-02	6,30E-06	1,26E-06	-5,03E-06	1,51E-05
337,5	5,89	-1,24E-02	3,82E-06	7,64E-07	-3,64E-06	1,09E-05
345,0	6,02	-8,41E-03	1,53E-06	3,06E-07	-2,57E-06	7,71E-06
352,5	6,15	-4,24E-03	4,55E-07	9,10E-08	-1,17E-06	3,51E-06
360,0	6,28	-7,96E-18	0,00E+00	0,00E+00	0,00E+00	0,00E+00

In yellow are the cells where the value was reconstructed to zero, since no simulation makes sense when the current  $i_r$  is naught. In blue is the overall sensitivity of the sensor, in V/A.

## APPENDIX I

```
%%%%%%%%%%%%%%%%%%%%%%%%%%%%%%%%%%%%%%%%%%%%%%%%%%%%%%%%%%%%%%%%%%%%%%%%
%%%%%%%%%%%%%%%%%%%%%%%%%%%%%%%%%%%%%%%%%%%%%%%%%%%%%%%%%%%%%%%%%%%%%%%% RC+SC output signal analysis %%%%%%%%%
%%%%%%%%%%%%%%%%%%%%%%%%%%%%%%%%%%%%%%%%%%%%%%%%%%%%%%%%%%%%%%%%%%%%%%%%
```

```
clear all
close all
```

```
% All calculations below are based on the simulated output of the "Rotating
% Coil + Fixed Coil" device
```

```
w=4000; % frequency of rotation (rad/s)
k=48; % length of the signal
Fs=w*k/(2*pi); % sampling frequency
t=(0:k-1)*2*pi/Fs; % time sample: 1 period
angleb=linspace(0,2*pi,k+1); % angle sample: 1 period
```

```
% _____
% _____ data acquisition: sensitivity signal _____
% _____
```

```
% the sensitivity signal is the output signal divided by the input current
```

```
s = xlsread('C:\Documents and Settings\Cyril Babinet\Mes
documents\Etudes\GIT\Thesis\Ansis\flux_vs_angle_rotor_stator', 2, 'L2:L49').';
```

```
% _____
% _____ fft of the sensitivity signal _____
% _____
```

```
K=k; % samples for fft
f = Fs/2*linspace(0,1,K/2+1); % vector of the frequencies
S = fft(s,K)/K; % Discrete Fourier Trans. of s
s1 = ifft(S,K)*K; % Inverse Fourier, for checking
P = S.*conj(S)/K; % The power spectrum
```

```
% _____
% _____ reconstruction with imaginary part _____
% _____
```

```
Ki=12; % number of peaks used (1 to 12)
```



```

s(49)=0; % final point of the signal
ri=0; % reconstructed signal

cri=-2*imag(S(2:2*Ki+1)); % coefficients of the peaks

for i=2:2:2*Ki
    y=sin(i*angleb).*cri(i);
    ri=ri+y;
end

% _____
% _____ Filtered signal with fundamental frequency only _____
% _____

s2w=sin(2*angleb).*cri(2);

% _____
% _____ Signal rectified and integrated over 4*pi _____
% _____

sri=(2*sum(abs(s))/48).*ones(1,49);

% _____
% _____ plotting _____
% _____

% Plot signal, fft/iff reconstruction, and difference
figure1= figure;
subplot(211)
plot11 = plot(t(1:k),s(1:k),'r');
xlabel('time (s)')
title('s: sensor sensitivity signal over one period')

subplot(212)
plot12 = plot(t(1:k-1),s1(1:k-1),'r',t(1:k-1),(s(1:k-1)-s1(1:k-1)), 'b');
title('signal reconstructed with inverse Fourier and error')
xlabel('time (s)')
legend1 = legend({'signal', 'error'}, 'Position', [0.150 0.1190 0.1286 0.1551]);

% -----
% Plot single-sided amplitude spectrum and angle of S
figure2 = figure;
subplot1 = subplot(2,1,1,...
    'XTickLabel', {'0','2','4','6','8','10','12','14','16','18','20','22','24',''},...
    'XTick', [0 2 4 6 8 10 12 14 16 18 20 22 24 25]);

```

```

box('on');
hold('all');

plot21 = plot(2.*pi.*f./w,2.*abs(S(1:K/2+1))); % 2(*abs): because one shows half of
the spectrum due to symmetry
title('Single-Sided Amplitude Spectrum of s');
xlabel('Frequency (factors of w)');
ylabel('|S(f)|');

%plot angle
subplot2 = subplot(2,1,2,...
'XTickLabel',{'0','2','4','6','8','10','12','14','16','18','20','22','24','"},...
'XTick',[0 2 4 6 8 10 12 14 16 18 20 22 24 25]);
box('on');
hold('all');

plot22 = plot(2.*pi.*f./w,angle(S(1:K/2+1))./pi); % no 2*...
title('angle of S in complex plane ');
xlabel('Frequency (factors of w)');
ylabel('angle (factors of pi)');

%-----
% Plot real part of fft
figure3 =figure;
subplot1 = subplot(2,1,1,...
'XTickLabel',{'0','2','4','6','8','10','12','14','16','18','20','22','24','"},...
'XTick',[0 2 4 6 8 10 12 14 16 18 20 22 24 25]);
box('on');
hold('all');
plot31 = plot(2.*pi.*f./w,2.*real(S(1:K/2+1)));

title('real y(t)');
xlabel('Frequency (factors of w)');
ylabel('real part(Y(f))');

% Plot imaginary part of fft
subplot2 = subplot(2,1,2,...
'XTickLabel',{'0','2','4','6','8','10','12','14','16','18','20','22','24','"},...
'XTick',[0 2 4 6 8 10 12 14 16 18 20 22 24 25]);
box('on');
hold('all');
plot32 = plot(2.*pi.*f./w,2.*imag(S(1:K/2+1)));

title('imag y(t)');
xlabel('Frequency (factors of w)');

```

```

ylabel('imag part(Y(f)/pi);

%-----
% Plot power spectrum of the signal
figure4 =figure;
subplot(1,1,1,...
    'XTickLabel',{'0','2','4','6','8','10','12','14','16','18','20','22','24','"},...
    'XTick',[0 2 4 6 8 10 12 14 16 18 20 22 24 25]);
box('on');
hold('all');
plot4=plot(2.*pi.*f./w,(P(1:K/2+1)));          %f(1:K+1),P(1:K+1)
title('Power spectrum of s');
xlabel('Frequency (factors of w)');
ylabel('P = fft(s)*conj(fft(s))');

%-----
% Plot reconstruction with imaginary part
figure
plot(angleb,s,'r',angleb,ri,'b',angleb,(s-ri),'g');    % ,angleb,-rif,'c+:'
title('Reconstruction using coefficients of sin(nw)')
xlabel('angle (rad)')
ylabel('amplitude (V)')
legend1 = legend({'signal: s','reconstruction','error'},'Position',[0.3661 0.745 0.1286
0.1551]); % , 'reconstr: -rif'

%-----
% Plot filtered signal with fundamental frequency only
figure
plot(angleb,s,'r',angleb,s2w,'b');
title('Filtered signal with fundamental frequency only')
xlabel('angle (rad)')
ylabel('amplitude (V)')
legend1 = legend({'signal: s','fundamental'},'Position',[0.3661 0.745 0.1286 0.1551]); % ,
'reconstr: -rif'

%-----
% Plot signal rectified and integrated over 4*pi
figure
plot(angleb,abs(s),'r',angleb,sri,'b');
title('Signal rectified and integrated over 4*pi')
xlabel('angle (rad)')
ylabel('amplitude (V)')
legend1 = legend({'rectified','integrated'},'Position',[0.3661 0.745 0.1286 0.1551]); % ,
'reconstr: -rif'

```

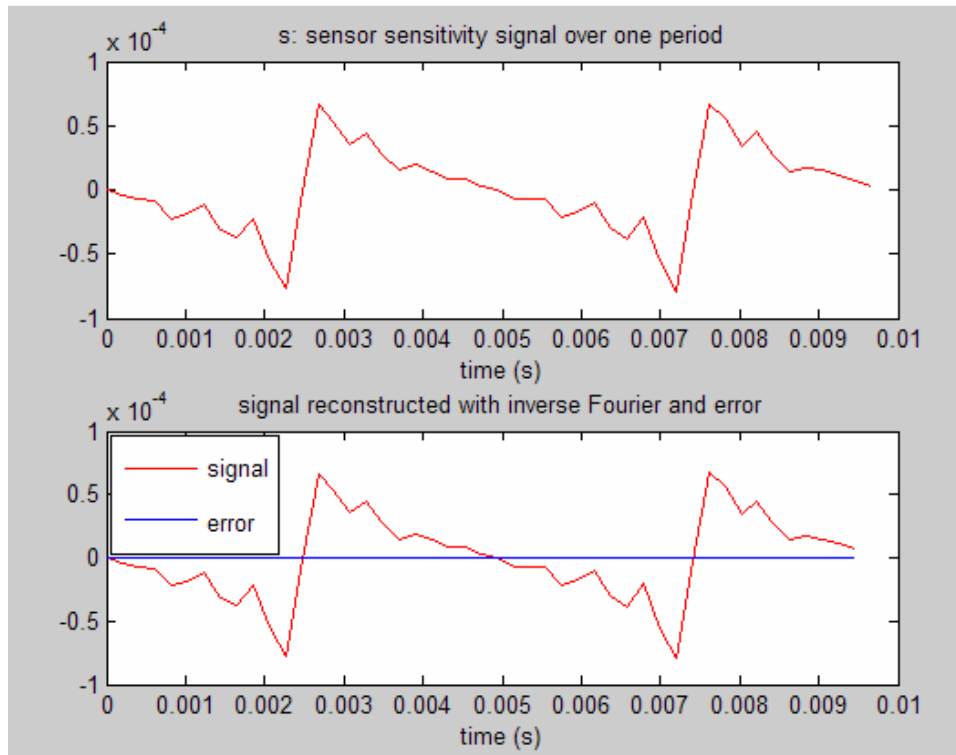


Figure 48: Signal and reconstruction trough inverse Fourier for checking, in V/A

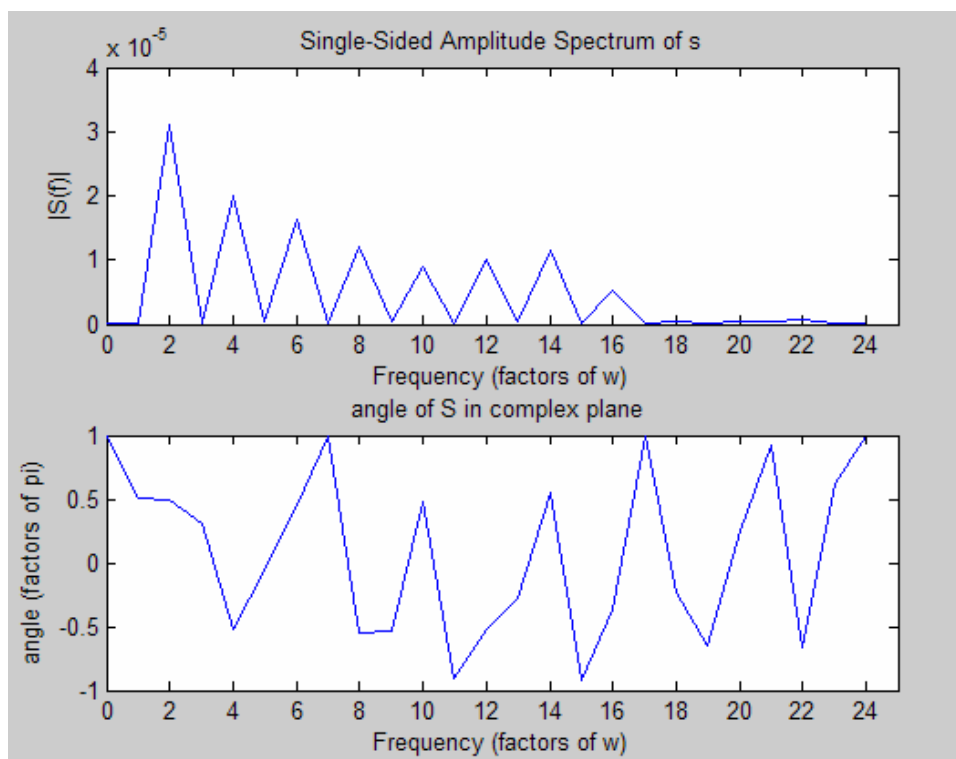
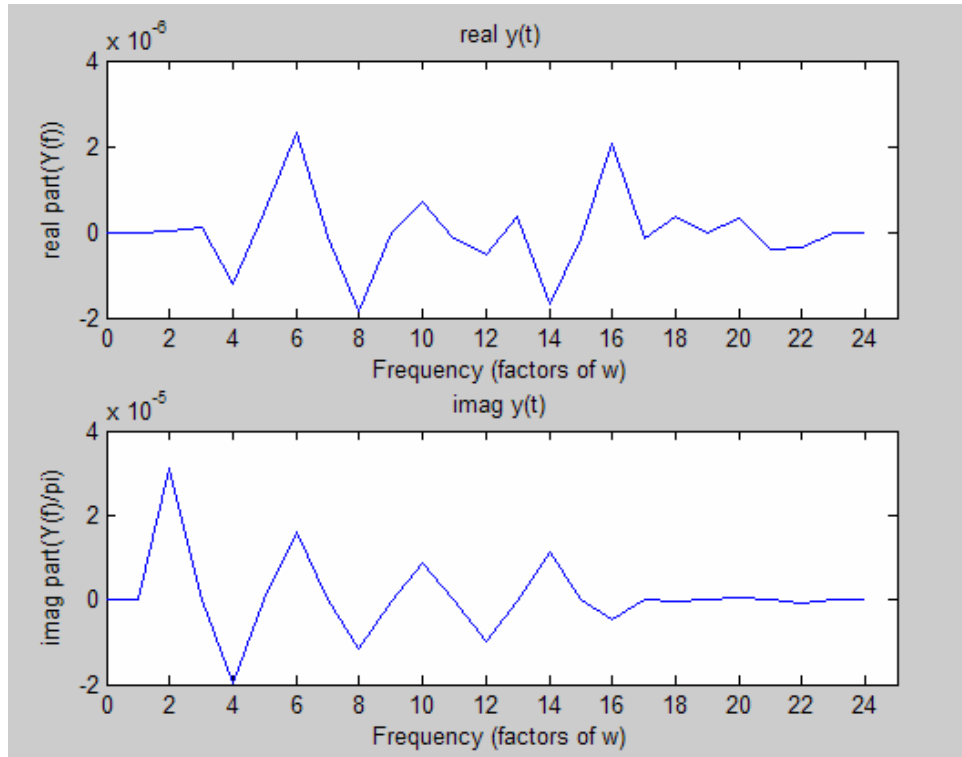
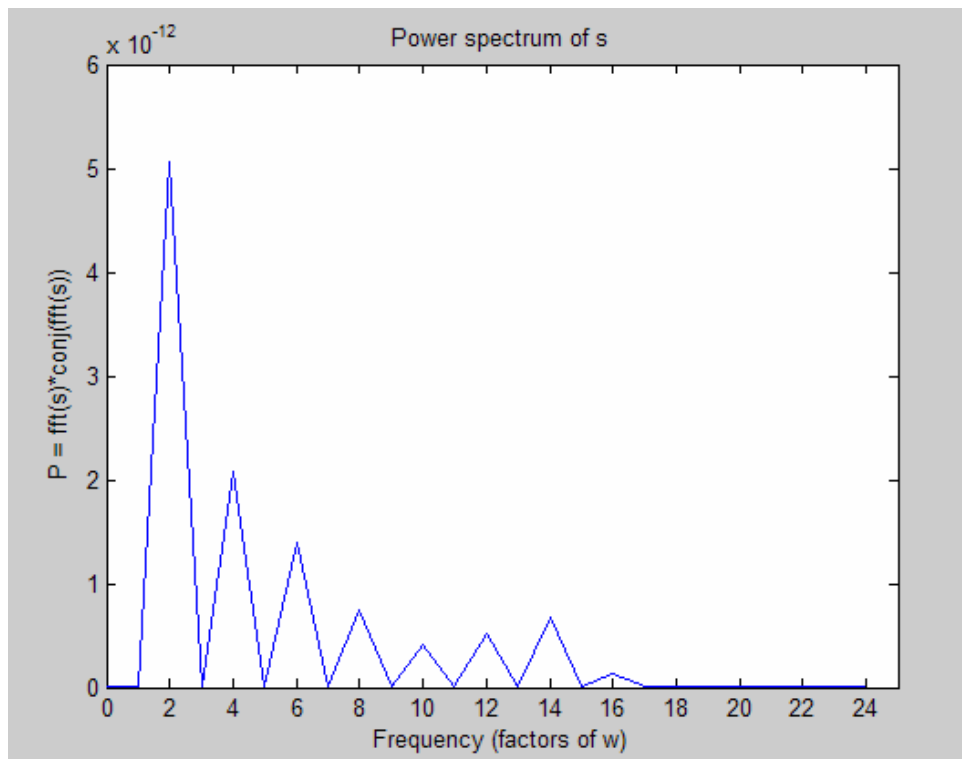


Figure 49: Amplitude in V/A and phase of the Fourier transform



**Figure 50: Real part and imaginary part of the signal in V/A. The real part (cosines) is negligible.**



**Figure 51: Power spectrum of the signal. The harmonics are not negligible**

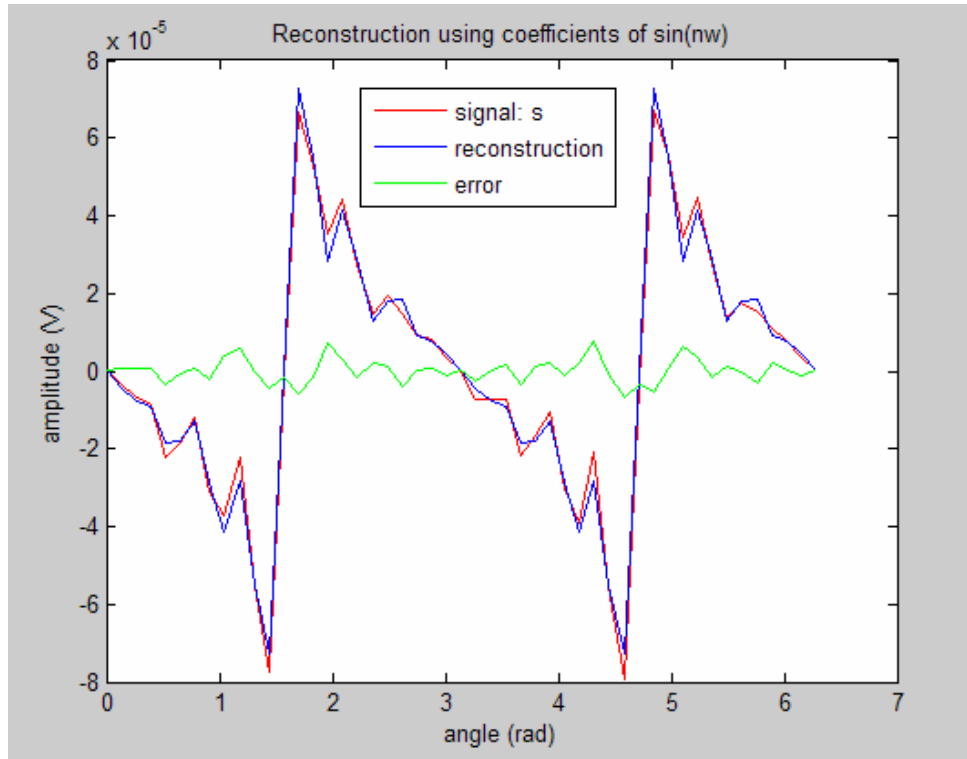


Figure 52: The reconstruction using only the imaginary part (sines) is fairly accurate

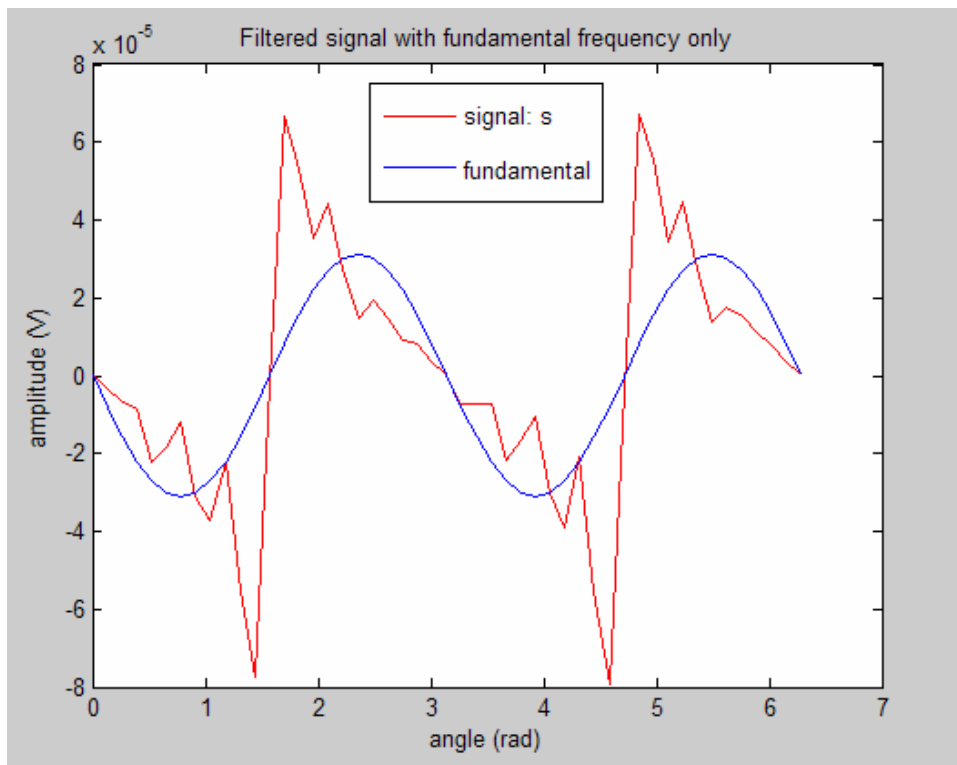
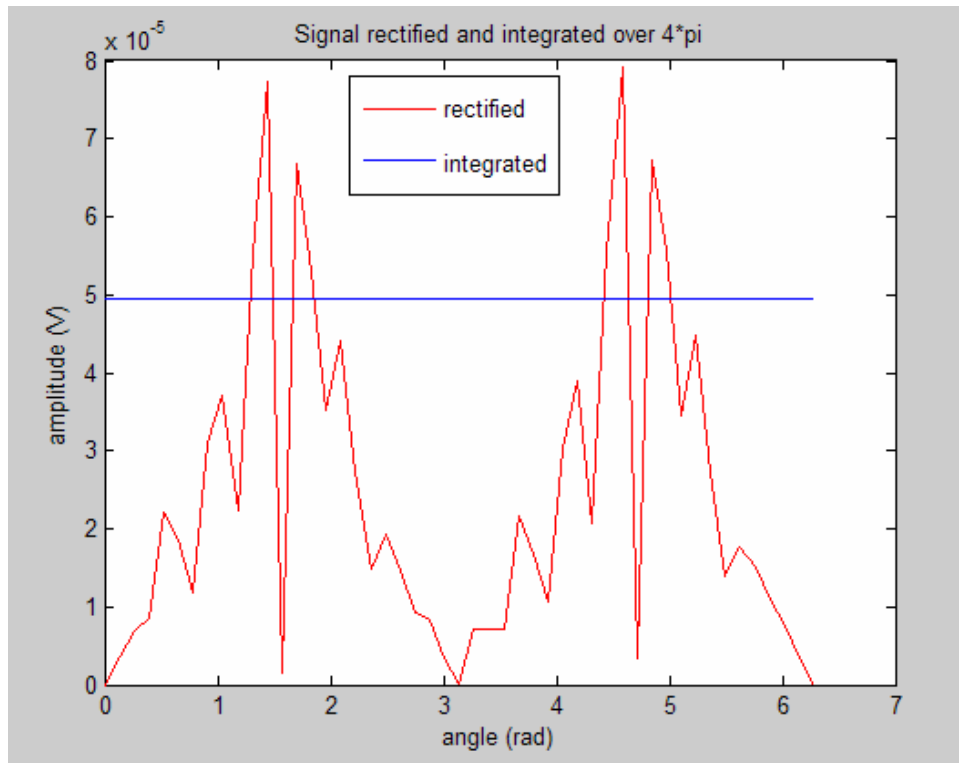


Figure 43: The reconstruction using only fundamental wastes power



**Figure 44: The signal rectified and integrated over 2 revolutions gives the desired output**

APPENDIX J

STRESS IN THE ROTOR DUE TO CENTRIPETAL ACCELERATION

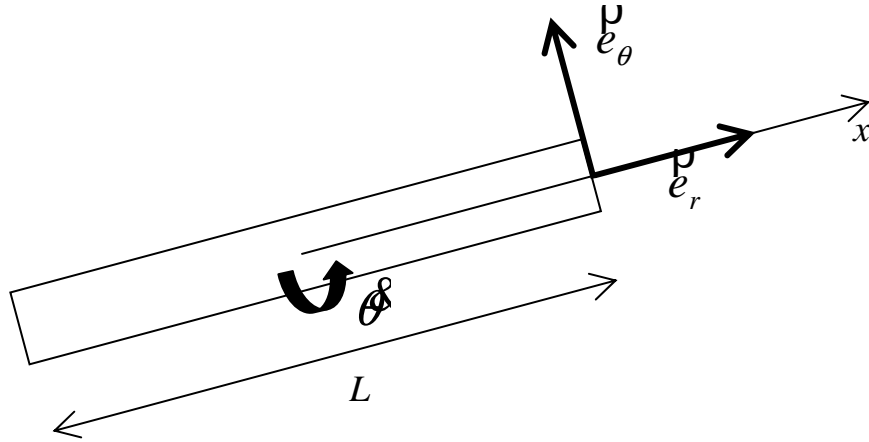


Figure 53: Top view of the rotor and polar coordinates

Calculation of the acceleration

Velocity: 
$$\mathbf{V}(r) = r \omega \mathbf{e}_\theta = r \omega \mathbf{e}_\theta^{\rho} \quad \text{Equation 37}$$

Acceleration: 
$$\mathbf{F}(r) = \frac{d\mathbf{V}(r)}{dt} = \frac{d(r\omega)}{dt} \mathbf{e}_\theta^{\rho} + r \omega \frac{d\mathbf{e}_\theta^{\rho}}{dt} \quad \text{Equation 38}$$

$$\mathbf{F}(r) = -r \omega^2 \mathbf{e}_r^{\rho} \quad \text{Equation 39}$$



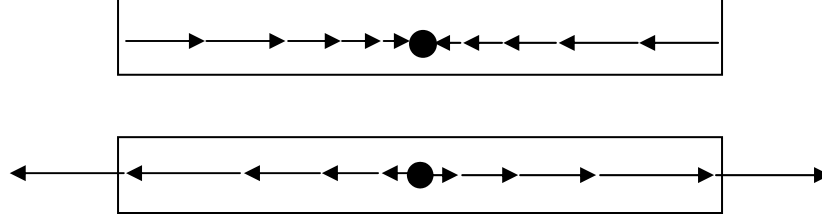


**Figure 54: Centripetal acceleration (top) and subsequent distributed force on the rotor (bottom)**

Distributed force: 
$$f_i(x) = -\rho \Gamma S_l$$
 **Equation 40**

Force: 
$$F(x) = \int_x^{L/2} f_i(x) dx = -\rho S_l \int_x^{L/2} \Gamma(x) dx = \omega^2 \rho S_l \int_x^{L/2} x dx$$
 **Equation 41**

$$F(x) = \frac{1}{2} \omega^2 \rho S_l [x^2]_x^{L/2} = \frac{1}{2} \omega^2 \rho S_l \left( \frac{L^2}{4} - x^2 \right)$$
 **Equation 42**

Stress: 
$$\sigma(x) = \frac{F(x)}{S_l} = \frac{1}{2} \omega^2 \rho \left( \frac{L^2}{4} - x^2 \right)$$
 **Equation 43**

Maximal stress: 
$$\sigma_{\max} = \sigma(x=0) = \frac{1}{8} \omega^2 \rho L^2$$
 **Equation 44**

$$\sigma_{\max} = 4.66 \times 10^5 Pa$$
 **Equation 45**

With  $S_l$  the area of the section normal to the  $x$  axis, and  $\rho = 2.33 \times 10^3 \text{ Kg.m}^{-3}$  the density of the rotor (silicon), and parameters  $\omega = 4 \times 10^3 \text{ rad.s}^{-1}$  and  $L = 10^{-2} \text{ m}$  from **Table 10**.

## APPENDIX K

### OPTIMISATION OF THE NUMBER OF COILS ON THE ROTOR

$R_r$  needs to be estimated. If it is necessary to increase the resistance of the winding of the rotor, adding resistors would concentrate heat dissipation, whereas acting on  $A_r$ , the area of the section of the conductor, would distribute it. Then there will be no resistors and the resistance will only be due to the resistivity  $\rho$  of the coils. If  $l_r$  is the length of the winding of the rotor and  $l_{r1}$  is the length of one coil, then

$$R_r = \frac{\rho \cdot l_r}{A_r} \approx \frac{\rho \cdot n_r \cdot l_{r1}}{A_r} \quad \text{Equation 46}$$

Then

$$e_s = \frac{\omega^2 \cdot B \cdot n_r^2 \cdot n_s \cdot S^2 \cdot \gamma}{R_r} \cdot \sin(2\beta(t)) \quad \text{Equation 23}$$

Becomes:

$$e_s \approx \frac{\omega^2 \cdot B \cdot n_r \cdot n_s \cdot S^2 \cdot \gamma \cdot A_r}{\rho \cdot l_{r1}} \cdot \sin(2\beta(t)) \quad \text{Equation 47}$$

$$e_s \propto n_r \cdot A_r \quad \text{Equation 48}$$

Now

$$n_r = \frac{h}{2d_r} = \frac{h}{4\sqrt{A_r/\pi}} \propto A_r^{-1/2} \quad \text{Equation 49}$$

With  $h$  the height of the set of coil (see **Figure 55**), limited to half of the height of the rotor if the set of coil covers the entire surface of the rotor. And  $d_r$  is the diameter of the conductor constituting the coil. **Equation 49** also implies that the distance between two coils is taken as equal to one diameter of conductor. Eventually, one gets:

$$e_s \propto A_r^{1/2}$$

**Equation 50**

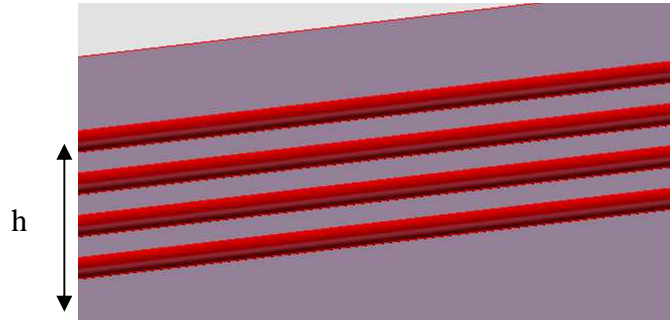


**Figure 55: Zoom on the set of coils of the rotor near the upper edge**

## REFERENCES

- 1- **SWAFFORD D.**, *New Generation of Current Sensor, Feasibility Study*, LI-E internal document.
- 2- **ZHOU H., HENSON B.**, *Analysis of a diamond-shaped mechanical amplifier for a piezo actuator*, in *International Journal of Advanced Manufacturing Technology*, (2007) 32: 1–7, DOI 10.1007/s00170-005-0303-7
- 3- **SARRAUTE E., VASIC D., COSTA F.**, *Transformateurs statiques piézoélectriques*, in *Techniques de l'Ingénieur*, D 3 015
- 4- **COSTA F., POULICHET P.**, *Sondes pour la mesure de courant en électronique de puissance*, in *Techniques de l'Ingénieur*, D 3 085
- 5- **PRIETO J.L., AROCA C., LOPEZ E., SANCHEZ M.C., SANCHEZ P.**, *Magnetostrictive-Piezoelectric Magnetic Sensor With Current Excitation*, in *Journal of Magnetism and Magnetic Materials* 215-216 (2000) 756-758